The bacterial flagellum: Modeling the dynamics of the elastic filament and its transition between polymorphic helical forms

vorgelegt von
Diplom-Physiker

Reinhard Vogel

geboren in Suhl

Von der Fakultät II - Mathematik und Naturwissenschaften
der Technischen Universität Berlin
zur Erlangung des akademischen Grades
Doktor der Naturwissenschaften (Dr. rer. nat.)

genemigte
Dissertation

Promotionsausschuss:	
Vorsitzender:	Prof. Dr. Martin Schoen
Erster Gutachter:	Prof. Dr. Holger Stark
Zweiter Gutachter:	Prof. Dr. Roland Netz

Tag der wissenschaftlichen Aussprache: 29.05.2012

Berlin 2012

D83

Inhaltsverzeichnis

1 Introduction **1**
- 1.1 Bacteria and their flagella . . . 1
- 1.2 Modeling the motor-driven flagellum and its polymorphism . . . 2

2 The bacterial flagellum – Biology and theoretical description **7**
- 2.1 The structure of the bacterial flagellum . . . 7
  - 2.1.1 The filament . . . 7
  - 2.1.2 The hook . . . 9
  - 2.1.3 The motor . . . 10
- 2.2 Swimming on the micron scale . . . 12
  - 2.2.1 The Stokes equation . . . 12
  - 2.2.2 Resistive force theory . . . 14
  - 2.2.3 Rotation of a rigid helix . . . 19
  - 2.2.4 Thermal fluctuations . . . 20
- 2.3 Elasticity theory of filaments . . . 22
  - 2.3.1 Differential geometry of space curves . . . 22
  - 2.3.2 Kirchhoff's rod theory . . . 25
  - 2.3.3 A brief introduction into the theory of buckling . . . 29
- 2.4 The numerical scheme . . . 32
  - 2.4.1 The discretized filament . . . 32
  - 2.4.2 Elastic forces and torques . . . 35
  - 2.4.3 Equations of motion and boundary conditions . . . 36
- 2.5 Theory of helical springs . . . 38
  - 2.5.1 The helical geometry . . . 38
  - 2.5.2 Effective compressional and torsional rigidity of a helix . . . 39
  - 2.5.3 Effective bending rigidity of a helix . . . 42
  - 2.5.4 Propagation of a disturbance . . . 43

3 Motor-driven bacterial flagella and buckling instabilities **45**
- 3.1 Introduction . . . 45
- 3.2 The motor-driven helical filament . . . 46
  - 3.2.1 Force-torque relation and buckling . . . 46
  - 3.2.2 Buckling instability during locomotion . . . 52
  - 3.2.3 Twist dependent friction . . . 53

3.3 Buckling theory for a helical rod . . . 55
3.3.1 Model equations . . . 55
3.3.2 Discussion . . . 59
3.4 Summary and conclusions . . . 62

4 Stretching induced polymorphic transformations 65
4.1 Introduction . . . 65
4.2 Continuum model for the bacterial flagellum . . . 67
4.2.1 Principles for extending Kirchhoff's rod theory . . . 67
4.2.2 The double-well potential does not reproduce the experiments . . . 68
4.2.3 Extended Kirchhoff rod theory . . . 69
4.2.4 Relation to the free energy of Wada and Netz . . . 71
4.3 Force-extension curves . . . 73
4.3.1 Pulling on and compressing the helical filament . . . 73
4.3.2 Ground-state energy difference of the coiled and normal state . . . 75
4.3.3 Twist-to-bend ratio . . . 76
4.3.4 Extensional rate . . . 79
4.4 Clamped filament . . . 81
4.5 Summary and conclusions . . . 85

5 Rotation-induced polymorphic transformations 87
5.1 Introduction . . . 87
5.2 Swimming of *Rhodobacter sphaeroides* . . . 89
5.2.1 Biology of *Rhodobacter sphaeroides* . . . 89
5.2.2 Modeling the polymorphic states and swimming of *Rhodobacter sphaeroides* . . . 90
5.2.3 Dynamics of the coiled-to-normal and normal-to-coiled transition 92
5.2.4 Changing the swimming direction with the run-and-stop strategy 96
5.2.5 Summary and conclusion . . . 100
5.3 Rotation-induced polymorphic transformations in *Escherichia coli* . . . 101

6 Conclusions 105

Kapitel 1

Introduction

1.1 Bacteria and their flagella

Bacteria are widespread all over the world with a total biomass, which is larger than the one of plants and animals [70, 130]. They have been found in parts of the earth which at first glance seemed to be devoid of life like hot springs or salt lakes [70]. Many of them use large organisms as their habitat. For example, in a human body there are around ten times more bacterial cells than human ones, many of them living in the gut. There they supply the digestion and prevent the outbreaking of diseases, which are caused by other bacteria [106].

One example of a bacterium, that lives in the intestine, is the *Escherichia coli*. Together with the closely related bacterium *Salmonella typhimurium* it is one of the bacteria, which has been studied in most detail. Therefore it acts as a standard model in bacteriology [78].

Many bacteria move actively, e. g. to increase the efficiency of nutrient acquisition, to avoid toxic substances, to translocate to new hosts, to access optimal colonization sites, or to disperse in the environment. When their motion is guided by a chemical gradient, this process is called chemotaxis [11]. Generally bacteria with a typical cell size of a few microns are too small to sense a gradient along their bodies. Therefore they sample their environment with time by performing a random walk. Then chemotaxis is used to bias the overall swimming direction of bacteria toward, or away from a particular stimuli [13, 14]. Different strategies to perform such a random walk are known [5, 13, 85, 104, 133].

Peritrichous bacteria such as *Escherichia coli* and *Salmonella typhimurium* swim by rotating a bundle of elastic filaments with helical shape, which are called flagella [13, 86]. The flagellum is a complex apparatus consisting of three parts: the rotary motor, a short and very flexible proximal hook, that couples the motor to the third part, which is the long helical filament [81, 87]. The filament of *E.coli* bacteria is up to 15 µm long and is about 0.015 µm in diameter [1]. It is relatively stiff but can switch between distinct polymorphic forms. In peritrichous bacteria the motors are embedded at different locations of the cell wall so that the flagella have to bend around the cell body to form a bundle. We note that eukaryotic cells like *Chlamydomonas reinhardtii* or spermatozoa also use an organelle called flagellum to swim [61, 95]. Nevertheless, the structure and

functionality of their flagellum differ completely from the bacterial flagellum.

During locomotion the bundle of flagella rotates counterclockwise as seen from behind and therefore generates a thrust force, which pushes the cell body forward. After a swimming period of about 1s the sense of rotation of one motor reverses and the attached flagellum leaves the bundle. Rotating now clockwise it undergoes a sequence of different helical configurations characterized by their pitch, radius and helicity. During this tumbling event the bacterium changes its swimming direction randomly. After around 0.1s the motor reverses its rotational direction again and the flagellum switches to its original normal helical form and returns into the bundle. This so called run-and-tumble strategy leads to a random walk. Whenever, for example, the bacterium senses a positive nutrient gradient, it prolongs the swimming phase and hence it drifts towards the source [13].

The polymorphism of the flagellum is a fascinating and intensively studied subject. Similar to the torque driven transformation during the tumbling of *E.coli* in experiments one induces transformations between different polymorphic forms by applying external forces or torques to the filament [28, 30, 54]. Furthermore the filament takes over these forms in response to different solvent conditions such as a change in pH value, salinity, or temperature of the surrounding solvent [48, 57, 58], and an addition of alcohol [53], or sugar [107]. This kind of polymorphic transition is observed for flagella of bacteria, which do not show a polymorphic transformation during swimming [104], too. A first theoretical explanation of the flagellar polymorphism has been given by Asakura [8] and Calladine [19] based on the microscopic structure of the flagellar filament.

The hydrodynamics of swimming bacteria with a helical filament has been studied in detail in the 1970s by Lighthill [79,80] and Purcell [97]. Later also the elastic filament has been investigated [66,124–126], which is important for the synchronization and bundling of two or more flagella due to hydrodynamic interactions [55, 64–66, 99, 101].

Bacteria and their flagella have already inspired researchers in nanotechnology and microfluidics. So bacteria are used to transport colloids [9] and pump fluids [29, 67]. The thin filament assists to create tubes for nanofluidics for medical applications [50, 51]. New liquid-crystalline phases of screw like objects were studied using the different polymorphic helical forms. Also artificial bacterial flagella have been fabricated [138].

An understanding of the bacterial tumbling motion and the applications of bacterial flagella in nanotechnology and microfluidics requires a sufficiently simple elastic model that includes the flagellar polymorphism. This work aims to provide such a model.

1.2 Modeling the motor-driven flagellum and its polymorphism

We start with the study of the dynamics of the normal form of a single bacterial flagellum. The model is based on a discretization of Kirchhoff's elastic-rod theory. The friction with the viscous environment is characterized by resistive force theory. We de-

velop a new coarse-grained approach for driving the helical filament by a motor torque. Therefore we formulate a boundary condition for the tip of the filament, which is attached to the motor, that reflects the property of the hook as universal joint. We perform our simulations with realistic parameter values and compare our results to experiments. A rotating helical flagellum produces a thrust force that adds up along the filament and then pushes the cell body forward. We fix the rotating flagellum at its tip, where the motor torque is applied, and show that it buckles under the thrust force at a critical torque, which is in the biologically relevant regime. Buckling becomes visible as a supercritical Hopf bifurcation in the thrust force. A second bifurcation occurs at an even higher motor torque. Then we attach the flagellum to a spherical load particle to mimic the influence of the cell body and we also observe the first buckling instability during locomotion. A variation of the necessary thrust force is provided by changing the size of the sphere. The analysis shows a characteristic relation between the critical thrust force and motor torque. Real values for motor torque, cell body size, and the geometry of the helical filament suggest that buckling should occur in a single bacterial flagella. In addition, we find that the orientation of a flagellum, which pushes along the driving torque, is stable whereas pulling flagellum is unstable. We comment on the biological relevance for single flagellated bacteria, i. e. for chemotaxis of marine bacteria.

The observed buckling transition is comparable to a vertical column that buckles under its own weight. A theoretical description of the bending column is given by the buckling theory of rods, which goes back to Euler [34] and is one of the first examples for a theoretical description of a bifurcation. In this work we treat buckling instabilities for the biologically relevant helical filament, where the force comes in due to the characteristic rotation-translation coupling. Based on the ideas of the buckling theory of rods we develop an analytical model for the buckling instability of the helical filament which quantitatively reproduces the critical force-torque relation from our simulations.

Then we extend Kirchhoff's rod theory to describe the transition between two polymorphic forms of the bacterial flagellum. The theoretical treatment is motivated by experiments done by Darnton and Berg [28]. They used an optical tweezer set-up to pull the two ends of the flagellar filament apart with a constant velocity which induced a transition between two polymorphic configurations. Then they compressed the flagellum to return to the initial configuration. Darnton and Berg recorded the force as a function of the extension of the filament mainly for the transformation between the coiled to the normal configuration. The transformation starts locally at one end of the flagellum and then proceeds in discrete steps along the flagellum, which was clearly visible in the force-extension curves.

Our modeling follows the spirit of previous work, where the authors introduced a double-well potential for the twist to describe the transition between two helical states [27, 40]. However, we show that a conventional double-well potential cannot reproduce the experimentally observed force extension curves. Therefore we develop an alternative model, where we assume the validity of Kirchhoff's elastic energy for both polymorphic states. Then the particular helical form, which has the lowest elastic energy, is observed.

In the limit, which is relevant for biology, we show the equivalence of our ansatz to the elastic model of Wada and Netz [126], who used Kirchhoff's model with attached spin variables along the filament to distinguish locally between the two helical states.

We present Brownian-dynamics simulations of the force-extension curves which reproduce the experimental results of the stretching-induced polymorphic transformations. Furthermore we focus on several aspects of the force-extension curves, namely, how they depend on the ratio of torsional and bending rigidities and on the extensional rate used to pull the flagellum apart. The mean extension, at which a coiled-to-normal transition first occurs locally, is a function of the extension rate. We demonstrate how this extension can be inferred from equilibrium properties of a clamped helical filament.

In the end, we study polymorphic transitions of a motor-driven flagellum which are induced by changing the applied motor torque. Therefore we apply our model of the polymorphism to the single-flagellated bacterium *Rhodobacter sphaeroides* to investigate the rotation-induced transition between the coiled and normal form of its flagellum. The bacterium uses a run-and-stop strategy for chemotaxis. During the run phase its flagellum is in the normal form, which is optimized to push the bacterium forward. When the motion stops, the flagellum relaxes into a lasso-like coiled state. After a while the flagellum starts to rotate again, which induces a polymorphic transition back into the normal state, and the bacterium swims into a new random direction. Our model of the bacterium reproduces this swimming behavior. We discuss the two observed transitions in detail and we show how the reorientation of the swimming direction of the cell is driven by the coiled-to-normal transition. Finally we demonstrate that our concept is applicable to describe transitions between several polymorphic forms with different helicity as observed during the tumbling of *E.coli*.

This work is organized as follows: In chapter 2 we give an overview of the methods used. First we shortly explain the biological background of the bacterial flagellum and we deduce our coarse-grained approach for driving the helical filament by a motor torque. Then we introduce the basic theory of swimming motion on the micron scale, which is important for bacteria. We explain the resistive force theory, which we use to describe the dynamics of the flagellar filament. Thereafter we summarize the classical elastic theory of rods, which goes back to Kirchhoff, and we show how to discretize the model, which we use in our simulations. Finally, we derive effective elastic constants, i. e. the torsional and bending rigidity and the spring constant of a helical filament. In chapter 3 we present and discuss our numerical results for the buckling instabilities of the rotating normal form of a single bacterial flagellum. After that we formulate a buckling theory for a helical rod and we show that it quantitatively reproduces the critical force-torque relation in the biologically relevant regime. Our extension of Kirchhoff's rod theory to include the polymorphism of the bacterial flagellum is presented in chapter 4. The results of the simulated force-extension curves are discussed. In the next step we use our model of the bacterial flagellum to simulate the swimming of *Rhodobacter sphaeroides* in chapter 5.

Thereafter we present simulations of the transitions, which are relevant for the tumbling of *E.coli*. Finally we close with a summary and conclusions in chapter 6.

Kapitel 2

The bacterial flagellum – Biology and theoretical description

2.1 The structure of the bacterial flagellum

Bacteria such as *Escherichia coli* and *Salmonella typhimurium* swim through a fluid by rotating a bundle of several flagella, which act as a kind of a propeller. The bacterial flagellum consists of three parts. The major component is the long extracellular helical filament, a biopolymer constructed from a single protein called flagellin. It is driven by a rotary motor. The connection between the motor and the filament is called hook. It is an extremely flexible but very short filament and acts as a constant velocity joint.

In this section we shortly introduce the biological and physical key features of the three components of the flagellum.

2.1.1 The filament

In principle one distinguishes two forms of the flagellar filament: the plain form and a complex form. Complex flagella are brittle and form left-handed helices with little or no structural polymorphism [104]. Also their molecular structure is more complex than from plain filaments [118]. In this work we deal only with the plain filament and its polymorphism which is found e. g. in *E. coli*, *Salmonella*, and *Rhodobacter* .

The filament is about 0.015µm in diameter and up to 15µm in length [1]. It is relatively stiff but can switch between distinct polymorphic forms. The filament assumes these forms in response to external perturbations such as changes in pH value, salinity, and temperature of the surrounding fluid [48, 57, 58, 104, 108], the addition of alcohols [53] or sugars [107], and by applying external forces or torques to the filament [28, 30, 54, 86].

The different forms have been explained by Calladine [19, 20] based on the work of Asakura [8], who has used the microscopic structure of the flagellar filament. We sketch the basic ideas of the theory in figure 2.1.

The helical filament is a cylinder formed by eleven protofilaments. Each filament consists of a stack of protein monomers called flagellin. These monomers assume two conformations, which are called L and R-state, respectively, and differ in length by 0.8Å [59,

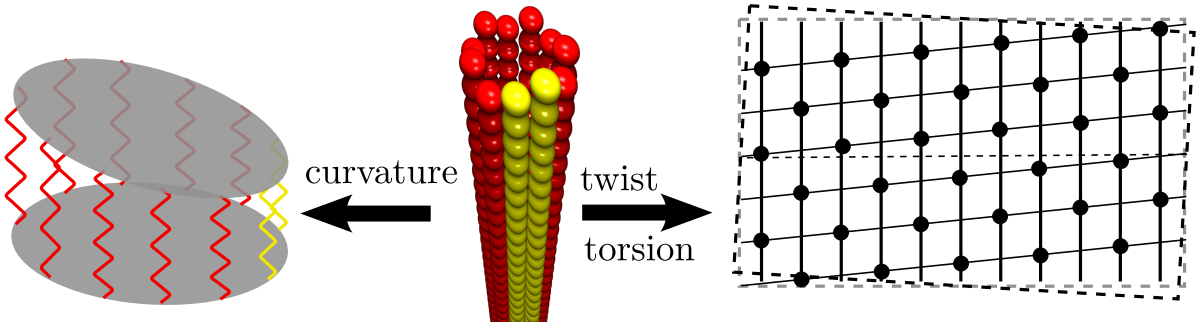

Abbildung 2.1: The flagellar filament is a polymer of a protein called flagellin, which has two states of different length. The proteins are ordered in eleven protofilaments, which form the filament **(center)**. In each protofilament only one state appears: the short or the long form of flagellin. Due to the coupling of different lengths of the protofilaments, the whole filament is bent **(left)**. The proteins have a fixed bond length with in a protofilament and to the neighboring protofilaments. To match this with the circumference of the filament the protofilaments are slightly twisted **(right)**. Together with the bending this leads to the helical structure of the filament.

102]. Each protofilament only contains one type of monomer, which is referred to as Calladine's rule [37]. Therefore the protofilaments have different lengths . The principle structure is sketched in the center of figure 2.1. To reduce the elastic strain within the filament the protofilaments form two clusters with the short and the long form, respectively. To equilibrate the two different lengths within the flagellar filament it starts to bend as shown left in figure 2.1.

The flagellin molecules of two neighboring protofilaments displaced axially relative to each other, which also depends on their state. To form a chemical bond between these proteins on the surface of the cylinder, the protofilaments are slightly tilted against the centerline of the flagellar filament as shown on the right hand side of figure 2.1. This introduces a twist of the filament and leads, together with the bending, to the helical shape of the flagellar filament.

Hence we obtain two straight forms with left- and, respectively, right-handed intrinsic twist, when all protofilaments are either in the R or in the L state. In addition we have ten helical polymorphic states for a filament containing R and L state protofilaments. All forms are presented in figure 2.2. The corresponding curvature and torsion was derived by Calladine [19, 20] as

$$\kappa_{n_R} = \kappa_{\mathtt{max}} \sin(\pi n_R/11), \qquad \tau_{n_R} = \tau_L + (\tau_R - \tau_L) n_R/11, \tag{2.1}$$

where n_R is the number of protofilaments in the R state. The quantities $\kappa_{\mathtt{max}} \approx 2.4/\mu\mathrm{m}$, $\tau_L \approx -5.2/\mu\mathrm{m}$, and $\tau_R \approx 11.8/\mu\mathrm{m}$ are fit parameters taken from [28]. Most of the polymorphic forms have been observed experimentally [49,134]. The molecular structure

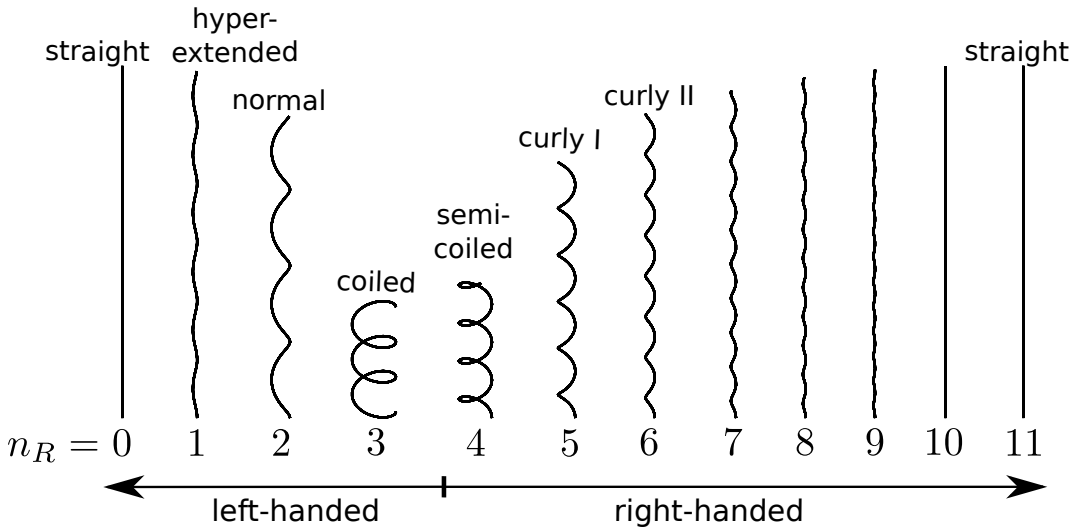

Abbildung 2.2: Twelve polymorphic states of the bacterial flagellum with length $L = 10\mu m$ and curvature and torsion given by Eq. (2.1).

for the flagellar filament has been confirmed recently [134, 137] and several extensions of Calladine's model exist [37, 49, 112–114].

It is interesting to note, that there exist three distinguishable families of bacterial flagella with significantly different fit parameters. These families belong to peritrichous bacteria like *E.coli* and *Salmonella*, monotrichous polar bacteria like *Pseudomonas* or bacteria with lateral flagella. But other forms has also been found [38].

In this work we use preferentially Eq. (2.1) and the given parameters to determine the intrinsic curvature and torsion for the polymorphic forms used in the simulations. But in chapter 5 we use different polymorphic forms of the flagellar filament of *Rhodobacter sphaeroides*.

2.1.2 The hook

The motor torque is transmitted to the helical filament by a short flexible coupling. Because of its shape it is called hook. With a well regulated length of $0.05\mu m$ for *E.coli* or *S.typhimurium* and up to $0.1\mu m$ for *R. sphaeroides* it is much shorter than the helical filament [56, 71, 103, 109]. It is also shorter than the typical discretization length of $h = 0.2\mu m$ which we can employ in our simulations. Therefore, we do not model the hook in full detail. Instead we neglect the extension of the hook and take it into account as a boundary condition for the end of the filament which is attached to the motor as discussed below.

Molecular dynamics simulations showed that the hook bends and twists easily. This is possible since conformational changes of molecular bonds require only a small amount

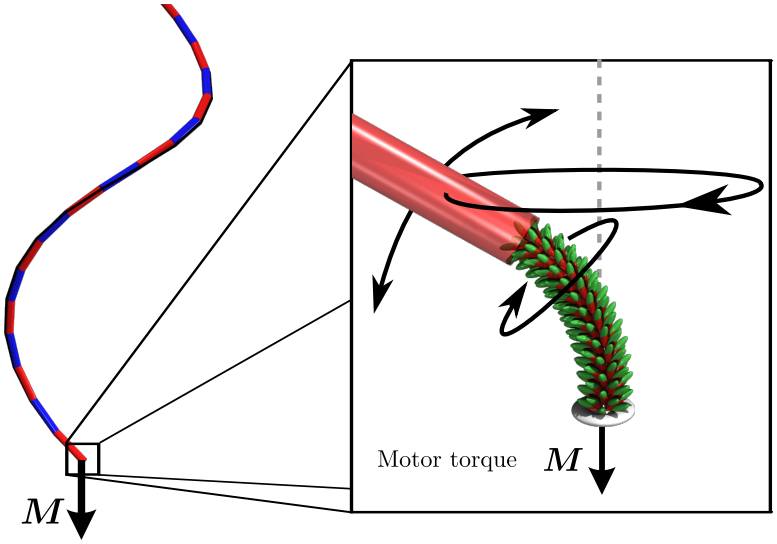

Abbildung 2.3: The hook acts as a universal joint between the motor embedded into the cell wall and the long helical filament, which retains its full rotational degrees of freedom. Because of its short length we do not model the hook explicitly but let the motor torque act directly on the tip of the filament, which can adopt any orientation in space.

of energy [39]. So the hook itself allows the filament to assume almost any orientation. Hence, it is comparable to a constant-velocity joint. The blow-up in figure 2.3 illustrates how motor and hook act together to drive the filament. The picture also shows the rotational degrees of freedom of the filament at the attachment point to the hook. The filament can rotate about its local axis, about the axis parallel to the motor torque, and towards or away from this axis.

Consequently, in this study we guarantee the rotational degrees of freedom of the filament. Therefore we balance the motor torque with the elastic and the frictional torque, acting on the tip of the filament attached to the motor. We note that our approach to drive the flagellum is different from other studies, where the helix direction is kept constant [101] or an artificial long hook was used [55, 129].

2.1.3 The motor

The rotation of the flagellar filament is induced by a rotary motor. It consists of a protein complex called the rotor, and a number of stator proteins that are fixed in the inner membrane. So it has a similar structure like a typical electric motor [12].

In bacteria like *E.coli* or *Salmonella*) it rotates with a constant torque but switches the sense of rotation between clockwise and counterclockwise which leads to the tumb-

ling [13]. For other bacteria like *Rhizobium lupini* [104] or *Rhodobacter sphaeroides* [3] it is reported that they change directly the rotational velocity instead of the more common change in rotational direction. The motor generates a torque of 1pNμm up to 4.6pNμm for *E.coli* [13, 110].

In contrast to other biological molecular motors like kinesin or myosine, the rotary motor of the bacterial flagellum does not use directly ATP as a source of energy [92]. Instead, it uses protons moving down an electro chemical gradient across the cell membrane [76, 90]. Also other ions can be used [13]. Several theoretical models exist to describe the typical behavior of this motor [77, 122].

The most important fact for us is, the motor runs at a constant torque over a broad range of angular velocities [12]. Hence,in our model we do not have to take into account a special torque-speed dependence and simply model the motor by employing a constant torque at the filament.

2.2 Swimming on the micron scale

2.2.1 The Stokes equation

In this work we analyze the physics of swimming bacteria in a fluid. When we speak about swimming we think of a motion through water or any other liquid without external forces. In this section the principles of the dynamics of fluids are shortly collected.

The incompressibility condition

The first principle is the conservation of mass. This means that in a small given volume the density ρ of the fluid changes if there is a mass flux $\rho\boldsymbol{u}$ in or out the volume for a local fluid velocity $\boldsymbol{u}$. This leads to the continuity equation [45, 75]

$$0 = \frac{\partial \rho}{\partial t} + \nabla \cdot (\rho \boldsymbol{u}). \tag{2.2}$$

For our purpose we consider the fluid as incompressible. So the density ρ is constant and equation (2.2) reduces to the incompressibility condition

$$0 = \nabla \cdot \boldsymbol{u}. \tag{2.3}$$

The Navier-Stokes equation

The second principle is given by Newton's laws of motion applied to a small fluid element [24, 45]

$$\rho \frac{\mathrm{d}\boldsymbol{u}}{\mathrm{d}t} = \boldsymbol{f}_{\text{fluid}} + \boldsymbol{f}_{\text{ext}}. \tag{2.4}$$

Hence the change of the momentum $\rho\boldsymbol{u}$ of a moving fluid element is given by forces acting on it. These forces are divided into external ones $\boldsymbol{f}_{\text{ext}}$ and forces through the interaction between neighboring fluid elements $\boldsymbol{f}_{\text{fluid}}$. The second one is given locally by the stress or pressure tensor $\boldsymbol{\Pi}$ projected on the surface $\mathrm{d}\boldsymbol{S}$ between the fluid elements $\mathrm{d}\boldsymbol{f}_{\text{fluid}} = \mathrm{d}\boldsymbol{S} \cdot \boldsymbol{\Pi}$. The stress tensor consists of the hydrostatic pressure p, which acts in any direction. In addition we have the shear stresses, which are proportional to the velocity difference between two neighboring fluid elements for a Newtonian fluid. The rate of deformation is given by the symmetrized velocity gradient $(\nabla \otimes \boldsymbol{u}) + (\nabla \otimes \boldsymbol{u})^{\mathrm{T}}$. Other terms proportional to the divergence of the velocity vanish due to the incompressibility. Hence the stress tensor is given by

$$\boldsymbol{\Pi} = -p\mathbf{1} + \eta\big((\nabla \otimes \boldsymbol{u}) + (\nabla \otimes \boldsymbol{u})^{\mathrm{T}}\big), \tag{2.5}$$

where we use the shear viscosity η. Finally the Navier-Stokes equation is established by [45]

$$\rho \frac{\mathrm{d}\boldsymbol{u}}{\mathrm{d}t} = \rho \left(\frac{\partial \boldsymbol{u}}{\partial t} + \boldsymbol{u} \cdot \nabla \boldsymbol{u} \right) = -\nabla p + \eta \nabla^2 \boldsymbol{u} + \boldsymbol{f}_{\text{ext}}. \tag{2.6}$$

Reynolds number

If one rescales the Navier-Stokes equation with the typical length a and velocity u of the investigated system only one dimensionless parameter remains. It is called *Reynolds number*

$$\mathtt{Re} = \frac{\rho u a}{\eta}. \tag{2.7}$$

An important consequence is that the solution of the Navier-Stokes equation of two systems that differ only in their size are equivalent if their Reynolds numbers are equal [75]. This fact is used to study simplified models of the complex flow of large technical objects like planes and ships or the consequences of natural disasters like tsunamis in water channels or wind tunnels (see e. g. [119, 136]). Furthermore large scale models are used to investigate the hydrodynamics on the micron scale [64, 72].

The Reynolds number can be interpreted as the ratio of the inertial force $F_{\mathtt{inert}} \sim \rho a^2 u^2$ and the dissipative force $F_{\mathtt{dis}} \sim \eta a u$. So for small numbers $\mathtt{Re} < 1$ the friction terms on the right hand side of the Navier-Stokes equations are important, whereas for $\mathtt{Re} \gg 1$ the change of momentum on the left hand side of the equation dominates which causes turbulence. For bacteria moving with full speed the Reynolds number is of the order $\mathtt{Re} \sim 10^{-5} \ldots 10^{-6}$ and so practically zero [13]. Hence inertia plays no role at all whereas friction dominates. As a consequence they only move as long as a thrust force pushes them forward. This means the physics for them is rather the Aristotelian dynamics than the one of Newton.

Alternatively we can explain the Reynolds number as the ratio of the hydrodynamic relaxation time $\tau_{\mathtt{relax}} \sim a^2\rho/\eta$ and the time $\tau_{\mathtt{transl}} = a/u$ required to travel the distance a. The hydrodynamic relaxation time describes how long a disturbed fluid element needs to be in mechanical equilibrium with its surrounding. Especially for a swimmer this is the characteristic time it needs to slow down after it stopped his swimming motions. For bacteria this time is in the order of $\tau_{\mathtt{relax}} \sim 1\mu\mathrm{s}$.

It is interesting to note that the translational time is more or less constant for swimmers of different size. In contrast, the body lengths varies over seven orders of magnitude from $\sim 10^{-6}$m for bacteria to ~ 10m for whales. The time needed to swim their body length is for all swimmers of the order of $0.1 \ldots 1$s. Some examples are given in table 2.1. To understand that this time is more or less independent from the body size, we compare the force F_{org} generated by the organism to swim and the counter acting friction force F_{fric}. The first one is proportional to the surface of the organism that acts on the fluid $F_{\mathrm{org}} \sim a^2$. The second one is given by $F_{\mathrm{fric}} \sim \eta v a$ if the dissipation is important or by $F_{\mathrm{fric}} \sim v^2 a^2$ if inertia dominates. Hence we find for small organisms a swimming time that is independent from the body size: $\tau_{\mathtt{transl}} \sim 1$ and for large ones a time that grows slowly: $\tau_{\mathtt{transl}} \sim \sqrt{a}$. So we can estimate the Reynolds number of swimming organisms only by their size. For small animals it scales like $a^2\rho/\eta$ and for large ones like $a^{\frac{3}{2}}\rho/\eta$. This is consistent with the scaling law: $\mathtt{Re} \sim a^{1.86}$ found empirically [94].

organism	length a/[m]	swimming velocity u/[m/s]	source
E.coli	$2 \cdot 10^{-6}$	$20 \cdot 10^{-6}$	[13]
Chlamydomonas	$2 \cdot 10^{-5}$	$11 \cdot 10^{-5}$	[95]
Paramecium	$2.5 \cdot 10^{-4}$	$1 \cdot 10^{-4}$	[44]
Euchaeta rimana (zooplankton)	$3 \cdot 10^{-3}$	$7 \cdot 10^{-3}$	[135]
Metridia pacifica	$4 \cdot 10^{-3}$	$4 \cdot 10^{-3}$	[135]
human	2	1	[94]
cetaceans	2	8	[79]

Tabelle 2.1: Comparison of the body size and swimming velocity of some swimmers. The time they need to travel their body length is more or less constant.

The Stokes equation

We have seen that for a swimming bacterium the Reynolds number is practically zero. This coincides with negligible inertial forces and relaxation times. As a consequence we can neglect the time derivative on the left hand side of the Navier-Stokes equation (2.6). Therefore it simplifies to the creeping-flow or *Stokes equations* [45]

$$0 = -\nabla p + \eta \nabla^2 \boldsymbol{u} + \boldsymbol{f}_{\text{ext}}. \tag{2.8}$$

These are three linear partial differential equations for the fluid velocity $\boldsymbol{u}$ and the pressure p with the viscosity η. In addition the incompressibility condition (2.3) has to be fulfilled to close the set of equations.

2.2.2 Resistive force theory

In a moving helical filament different parts of the filament interact via hydrodynamic interactions. A common way to study the interaction of the helix with its flow field is the slender body theory [65, 66, 79] that uses a Green's function approach for the solution of the Stokes equation. The disadvantage of this method is its computational expense.

This is the reason why we use in this work the so called resistive force theory which is also a common technique to study the dynamics of elastic filaments in a viscous fluid (see e. g. [24, 27, 66, 131, 132]). In this theory one introduces local friction coefficients per unit length parallel $\gamma_{\parallel}$ and perpendicular $\gamma_{\perp}$ to the tangent vector of the filament. Long ranged hydrodynamic interactions are neglected.

We start with the general equations of motion of an arbitrary rigid particle. Based on this we introduce resistive force theory and its application to the helix. After that we summarize some aspects of the hydrodynamics of a helical filament.

The motion of a rigid particle of arbitrary shape

To calculate the flow field induced by a particle at position $\boldsymbol{r}$ moving with velocity $\boldsymbol{v}$ and rotating with angular velocity $\boldsymbol{\omega}$ in the fluid, one has to solve a boundary value problem. For the velocity on the particle surface one usually assumes the so called no-slip boundary conditions. This means that the fluid velocity at a point $\boldsymbol{r}_0$ of the surface S_p is equal to the surface velocity $\boldsymbol{u}(\boldsymbol{r}_0) = \boldsymbol{v} + \boldsymbol{\omega} \times (\boldsymbol{r} - \boldsymbol{r}_0)$.

By solving the Stokes equation we obtain the stress tensor $\boldsymbol{\Pi}(\boldsymbol{v}, \boldsymbol{\omega})$ (see Eq. (2.5)) as a function of the particle velocity and the angular velocity. Then we can calculate the local forces acting on the particle by projecting it on the local surface element $\mathrm{d}\boldsymbol{S}$. The total force $\boldsymbol{F}$ and torque $\boldsymbol{M}$ are obtained from the integration over the entire surface S_p

$$\boldsymbol{F}(\boldsymbol{v}, \boldsymbol{\omega}) = \int_{S_p} \boldsymbol{\Pi} \cdot \mathrm{d}\boldsymbol{S}, \qquad \boldsymbol{M}(\boldsymbol{v}, \boldsymbol{\omega}) = \int_{S_p} \boldsymbol{r}_0 \times (\boldsymbol{\Pi} \cdot \mathrm{d}\boldsymbol{S}). \tag{2.9}$$

It follows from the linearity of the Stokes equations, that the functional relation between the force and the torque on the one hand side and the velocity and angular velocity on the other is linear. One can show that this linear relation has to be symmetric [45, 98]. Consequently we write down a matrix equation and obtain the *equations of motion of a particle of arbitrary shape* [45]

$$\begin{pmatrix} \boldsymbol{F} \\ \boldsymbol{M} \end{pmatrix} = \begin{pmatrix} \mathsf{A} & \mathsf{C}^{\mathrm{T}} \\ \mathsf{C} & \mathsf{B} \end{pmatrix} \cdot \begin{pmatrix} \boldsymbol{v} \\ \boldsymbol{\omega} \end{pmatrix}. \tag{2.10}$$

The block matrix is called *resistance* and it contains the following second rank tensors

- the symmetric *translational tensor* A,
- the symmetric *rotation tensor* B,
- and the *coupling tensor* C, that represents a coupling of the translational and rotational motion.

The resistance tensor contains all information about the interaction of the particle with the fluid. Hence, if we know the resistance we do not need to calculate the flow field at all. For a rigid particle in an unbounded fluid it is proportional to the viscosity η and depends otherwise only on the geometry of the particle. Its entries scale with the characteristic particle size a as $\mathsf{A} \sim a$, $\mathsf{B} \sim a^3$, and $\mathsf{C} \sim a^2$.

In general it is difficult to calculate the resistance matrix. Instead, by using informations about the symmetry of an object one can determine some general properties. For example the tensors A and B are invariant under a reflectional transformation, whereas the sign of C changes. Consequently for a particle with reflectional symmetry the coupling tensor vanishes.

For example we can determine the resistance of a sphere. It has to be invariant under any rotation. The only second rank tensors with this property are proportional to the identity $\mathbf{1}$. The proportionality constants can be derived [45] and are given by

$$\mathbf{A}_{\mathtt{sphere}} = 6\pi\eta a\mathbf{1}, \qquad \mathbf{B}_{\mathtt{sphere}} = 8\pi\eta a^3\mathbf{1} \tag{2.11}$$

with the radius a of the sphere.

As second example we consider a thin rod with length L, diameter d, and with the unit vector $\boldsymbol{t}$ parallel to its axis. It remains invariant under any rotation around its axis. So we can split up the tensor in parts that act parallel and perpendicular to the rod axis where the latter is isotropic

$$\mathbf{A}_{\mathtt{rod}} = A_{\parallel}(\boldsymbol{t}\otimes\boldsymbol{t}) + A_{\perp}(\mathbf{1} - \boldsymbol{t}\otimes\boldsymbol{t}) \tag{2.12}$$

$$\mathbf{B}_{\mathtt{rod}} = B_{\parallel}(\boldsymbol{t}\otimes\boldsymbol{t}) + B_{\perp}(\mathbf{1} - \boldsymbol{t}\otimes\boldsymbol{t}). \tag{2.13}$$

The friction coefficients can be derived as [31]

$$A_{\parallel} = \frac{2\pi\eta L}{\ln(L/d)}, \qquad A_{\perp} = \frac{4\pi\eta L}{\ln(L/d)}, \tag{2.14}$$

$$B_{\parallel} = \pi\eta L d^2, \qquad B_{\perp} = \frac{\pi\eta L^3}{3\ln(L/d)}. \tag{2.15}$$

For an object consisting of several particles that are located far enough away from each other, such that their velocity fields do not interact, their resistance tensors just add up. This is the basic idea of the resistive force theory of a long thin filament. The basic assumption is that the filament can be described locally by a rod with appropriately chosen friction coefficients parallel $\gamma_{\parallel}$ and perpendicular $\gamma_{\perp}$ to the tangent vector of the filament. Then the total resistance is determined by the sum or integral of all rods forming the filament.

Resistive force theory and its application to a helix

We assume a rigid filament $\boldsymbol{r}(s)$ parametrized by its arc length s with translational velocity $\boldsymbol{v}$ and angular frequency $\boldsymbol{\omega}$. Each segment moves with a velocity $\boldsymbol{v} + \boldsymbol{\omega}\times\boldsymbol{r}$. Using local friction coefficients per unit length parallel $\gamma_{\parallel}$ and perpendicular $\gamma_{\perp}$ to the tangent vector $\boldsymbol{t} = \boldsymbol{r}'(s)$ of the filament we derive the force and torque densities that initiate such a motion by

$$\boldsymbol{f} = \left(\gamma_{\parallel}\boldsymbol{t}\otimes\boldsymbol{t} + \gamma_{\perp}\left(\mathbf{1} - \boldsymbol{t}\otimes\boldsymbol{t}\right)\right)\cdot(\boldsymbol{v} + \boldsymbol{\omega}\times\boldsymbol{r}), \tag{2.16}$$

$$\boldsymbol{m} = \boldsymbol{r}\times\boldsymbol{f}. \tag{2.17}$$

We note that the rotational friction coefficients are neglected because for small rods they are much smaller than the translational ones. Integrating the force and torque densities

along the filament gives the linear relation between force, torque, velocity, and angular velocity (2.10).

Now we use a helical filament with helical radius R and pitch angle α. The position vector along the arc length s is given by

$$\boldsymbol{r}(s) = \left(R\cos\left(\frac{\cos\alpha}{R}s\right), R\sin\left(\frac{\cos\alpha}{R}s\right), \sin\alpha s\right)^{\mathrm{T}}. \tag{2.18}$$

Now we can derive the full resistance of the helix by integrating Eq. 2.17 along the curve 2.18. Here we give the relevant coefficients for a helix with a full turn $L = 2\pi R/\cos\alpha$

$$A_\perp = L\gamma_\perp\left(1 - \frac{\delta}{2}\cos^2\alpha\right), \tag{2.19a}$$

$$A_\parallel = L\gamma_\perp\left(1 - \delta\sin^2\alpha\right), \tag{2.19b}$$

$$B_\parallel = L\gamma_\perp R^2\left(1 - \delta\cos^2\alpha\right), \tag{2.19c}$$

$$C_\parallel = -L\gamma_\perp R\delta\sin\alpha\cos\alpha, \tag{2.19d}$$

where we use $\delta = \frac{\gamma_\perp - \gamma_\parallel}{\gamma_\perp}$ to characterize the anisotropy in the local friction coefficients. The coefficients $A_\parallel$, $B_\parallel$, and $C_\parallel$ describe the translational friction, the rotational friction and the coupling parallel to the helical axis, whereas $A_\perp$ describes the friction of the helix perpendicular to its axis. Note that $A_\parallel$ also holds for arbitrary filament lengths, if L is not an integer of a full helical turn. For all other coefficients one obtains corrections of the form $\sin\left(\frac{\cos\alpha}{R}L\right)$ which are negligible in the limit $L \to \infty$.

For a simple theory for the propulsion of a helical flagellum we restrict equation (2.10) to the direction parallel to the helical axis. Using the parallel coefficients above, we obtain

$$\begin{pmatrix} F \\ M \end{pmatrix} = \begin{pmatrix} A_\parallel & C_\parallel \\ C_\parallel & B_\parallel \end{pmatrix} \cdot \begin{pmatrix} v \\ \omega \end{pmatrix} \tag{2.20}$$

Here M denotes the motor torque used by the bacterium to rotate the flagellum with the angular velocity ω. So the thrust force F is created to push the bacterium with a velocity v forward. The actual velocity is determined by the friction force $A_{\mathtt{cell}}v$ of the cell body, that has to balance the thrust force. We note that the cell body also rotates in the opposite direction of the flagellum with an angular velocity $\omega_{\mathtt{cell}}$ to balance the motor torque. As a consequence the motor has to spin with frequency $\omega_{\mathtt{motor}} = \omega - \omega_{\mathtt{cell}}$. By comparing the least power required to move the cell and which is given by $vF = A_{\mathtt{cell}}v^2$, with the power output of the motor $M\omega_{\mathtt{motor}}$, Purcell [97,98] derived the maximal propulsive efficiency $\varepsilon_{\mathtt{max}}$ of a helical flagellum as

$$\varepsilon_{\mathtt{max}} = \frac{1}{4}\frac{C_\parallel^2}{A_\parallel B_\parallel} \lessapprox 2\%. \tag{2.21}$$

This is consistent with experimental measurements [23] and calculations using slender body theory [111].

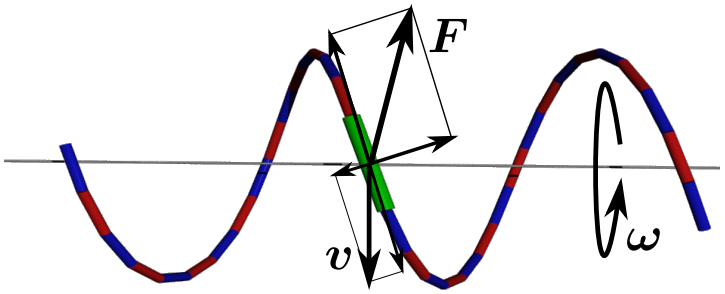

Abbildung 2.4: Each segment of a rotating helical flagellum experiences a frictional force $\boldsymbol{F}$ that is not anti-parallel to the local velocity $\boldsymbol{v}$ due to the anisotropic friction of a rod. Whereas the force component perpendicular to the helix axis averages to zero over one helical turn, the parallel component adds up to the thrust force.

A simple argument for the rotational induced thrust force of the helix is shown in figure 2.4. We only regard a rotation about the helical axis. The local velocity is perpendicular to this axis. But due to the anisotropic friction of a rod the opposing friction force is not anti-parallel to the velocity. Whereas the force component perpendicular to the helix axis averages to zero over one helical turn, the parallel component adds up to the thrust force pushing the bacterium forward. It is notable that this argument goes back to Buder in 1915 [13, 18] .

To adjust the local friction coefficients $\gamma_\parallel$ and $\gamma_\perp$ for the helical filament, Lighthill [79] used slender-body theory. He obtained

$$\gamma_\parallel = \frac{2\pi\eta}{\ln(2q/r)} \qquad \text{and} \qquad \gamma_\perp = \frac{4\pi\eta}{\ln(2q/r) + 1/2}. \tag{2.22}$$

Here $r = 0.01\mu\text{m}$ is the cross-sectional radius of the bacterial flagellum and q a characteristic length which has been derived by Lighthill as $q = 0.09\Lambda$, where $\Lambda = 2\pi R/\cos\alpha$ is the filament length of one helical turn.

For the bacterial flagella this leads to $\gamma_\parallel \approx 1.54\eta$, $\gamma_\perp \approx 2.74\eta$ for the normal state and $\gamma_\parallel \approx 1.64\eta$, $\gamma_\perp \approx 2.91\eta$ for the coiled state. Since the coefficients are similar in both states, we use the intermediate values $\gamma_\parallel \approx 1.6\eta$ and $\gamma_\perp \approx 2.8\eta$ for our simulations.

Kim and Powers compared [66] the local thrust forces of a helix calculated with resistive force theory and slender body theory. For the case of a helix with large pitch and small radius like the normal form of bacterial flagella, they obtained good agreements between both theories apart from boundary effects. Only for close-coiled helices with small pitch and large radius they observed deviations in the computed forces up to a factor four. Here each coil obstructs the flow to the next one. Since slender body theory accounts for these long ranged interactions, the components of the force along the flow direction is much smaller in slender body theory than in resistive force theory.

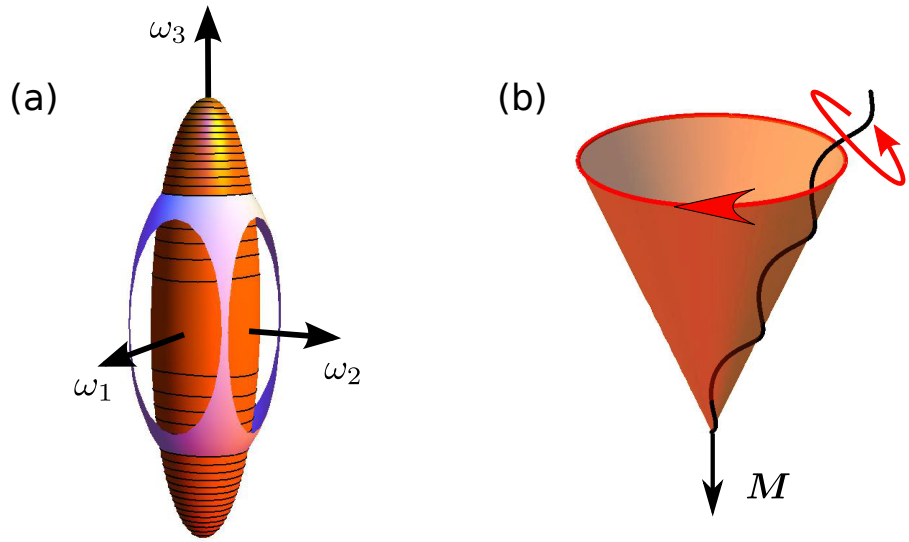

Abbildung 2.5: **(a)** The constant applied torque and the dissipated energy define two ellipsoids (red and blue) in the body fixed frame of a rigid helix. The intersection gives the path of the angular velocity $\boldsymbol{\omega}$. For a long slender helix two directions are degenerate and the trajectories are circles. **(b)** In the lab frame the helix rotates about its axis which precesses about the applied torque $\boldsymbol{M}$.

Chattopadhyay and Wu measured [23] the velocity and the generated torque for different bacteria. The results were compared with theoretical predictions of slender body theory and resistive force theory with the coefficients of Lighthill and of Gray and Hancock. For the estimated torque they observed good agreement between experiment, slender body theory, and the Lighthill's resistive force theory. For a large cell body resistive force theory overestimates the velocity up to a factor of two. The error of slender body theory has been derived in the order of 15%. We conclude that resistive force theory will catch the basic physics but we also expect quantitative deviations in the filament dynamics compared to the experiment.

2.2.3 Rotation of a rigid helix

Now we investigate the behavior of a rigid helix fixed at one point under a constant torque. The theory is not restricted to a helix, rather it is the theory of a top at low Reynolds number.

Starting from Eq. (2.10) we set $\boldsymbol{v} = 0$ and concentrate on the rotational motion due

to a constant external torque $\boldsymbol{M}$ with the relevant equation

$$\boldsymbol{M} = \mathbf{B} \cdot \boldsymbol{\omega}. \tag{2.23}$$

The rotational friction tensor $\mathbf{B}$ is symmetric. In the following we use its frame of eigenvectors $\{\boldsymbol{e}_1, \boldsymbol{e}_2, \boldsymbol{e}_3\}$ and the eigenvalues B_1, B_2, and B_3. We differentiate Eq. (2.23) with respect to time t, use $\partial_t \boldsymbol{e}_i = \omega \times \boldsymbol{e}_i$ and obtain

$$B_1 \partial_t \omega_1 = (B_2 - B_3)\omega_2 \omega_3, \tag{2.24}$$
$$B_2 \partial_t \omega_2 = (B_3 - B_1)\omega_1 \omega_3, \tag{2.25}$$
$$B_3 \partial_t \omega_3 = (B_1 - B_2)\omega_1 \omega_2. \tag{2.26}$$

These equations are equivalent to the Euler equations for a rigid body with an inertia tensor $\mathbf{B}$ and without friction. The external torque is zero hence the angular momentum is conserved. Following this analogy and according to Eq. (2.23) the constant external torque in our case corresponds to the angular momentum of the rigid body and the dissipated energy $P = \boldsymbol{M} \cdot \boldsymbol{\omega}$ to the rotational kinetic energy. Furthermore, up to the square of the applied torque $M^2 = (\mathbf{B} \cdot \boldsymbol{\omega})^2$ also the dissipated energy $P = \boldsymbol{\omega} \cdot \boldsymbol{M} = \boldsymbol{\omega} \cdot (\mathbf{B} \cdot \boldsymbol{\omega})$ is a conserved quantity too and the trajectory of $\boldsymbol{\omega}$ follows from the intersection of two ellipsoids as illustrated in figure (2.5)(a). In particular, if two of the friction coefficients B_i are equal, the angular velocity $\boldsymbol{\omega}$ precesses in real space on a cone about the direction of the torque [7, 73].

We already calculated one component of the rotational friction tensor $\mathbf{B}$ of a helix with filament length L in the previous section. In general for a long slender helix, like the normal form of the bacterial flagellum, two eigenvalues B_1 and B_2 of $\mathbf{B}$ are equal to a good approximation. Due to the scaling with the flagellum length, $B_1 \approx B_2 \propto L^3$, they are large compared to the third one, $B_3 \propto L$. This third friction coefficient belongs to the principal axis, which is parallel to the helical axis, again to a good approximation. Hence a rigid helical filament precesses about the applied torque as shown in figure (2.5)(b).

2.2.4 Thermal fluctuations

Until now we described the dynamics of a rigid particle with continuum fluid mechanics. Now we focus on the interaction of our micron sized object with the solvent molecules. Although the size and the dynamics of the fluid molecules are on a much smaller scale than we are interested in, they have some influence on the dynamics of the filament, e. g. for the transitions between the polymorphic states in bacterial flagella.

On the one hand the particle transfers its momentum to the fluid, which we described before with the resistance equation (2.10). On the other hand the particle experiences random kicks from the solvent molecules leading to a random locomotion. This is called Brownian motion named after Robert Brown [17] who has observed it in 1827. An explanation has been given around 80 years later by Einstein [33] using the molecular nature of the fluid.

We model Brownian motion with over-damped Langevin equations [6,69] that balances a stochastic thermal force $F_{\mathtt{th}}$ by viscous drag (2.10) and reads in one dimension as

$$\gamma \frac{\mathrm{d}x}{\mathrm{d}t} = F_{\mathtt{th}}, \tag{2.27a}$$

$$\langle F_{\mathtt{th}} \rangle = 0, \qquad \langle F_{\mathtt{th}}(0) F_{\mathtt{th}}(t) \rangle = 2\gamma K_B T \delta(t). \tag{2.27b}$$

Because the thermal force is not directed its mean value $\langle F_{\mathtt{th}} \rangle$ has to be zero. Furthermore we assume a delta correlated stochastic process, which is also called white noise. The reason is the large difference between the molecular time scale at which it is generated and the time scale which we are studying. The statistical properties of the particle in the fluid fulfills thermal equilibrium properties described by statistical physics. Therefore the second moment is proportional to the thermal energy $k_B T$. It is related to the diffusion constant D of the particle, which is derived by the following short calculation

$$\begin{aligned} \left\langle x^2(t) \right\rangle =& \left\langle \frac{1}{\gamma} \int_0^t F_{\mathtt{th}}(t_1) \mathrm{d}t_1 \frac{1}{\gamma} \int_0^t F_{\mathtt{th}}(t_2) \mathrm{d}t_2 \right\rangle \\ =& \frac{1}{\gamma^2} \int_0^t \int_0^t \langle F_{\mathtt{th}}(t_1) F_{\mathtt{th}}(t_2) \rangle \, \mathrm{d}t_1 \mathrm{d}t_2 \\ =& 2\gamma^{-1} k_B T t \ := \ 2Dt. \end{aligned} \tag{2.28}$$

Hence, we regard the Stokes-Einstein relation

$$D = \gamma^{-1} k_b T, \tag{2.29}$$

between the temperature of the solvent T, the diffusion constant D and the friction γ of the particle, which was deduced by Einstein [33] in 1905. It is a simple version of the more general fluctuation-dissipation theorem [31]. In general the diffusion constant D and the friction coefficient γ are second rank tensors. In the case of a helix this leads to an coupling of the translational and rotational diffusion [52].

We note, in the numerical solution of a Langevin equation with discrete time steps Δt one has to ensure the correct linear behavior of the mean square displacement. Therefore the discrete stochastic force scales with the time step $F_{\mathtt{th}} \propto (\Delta t)^{-1/2}$. For further reading we refer to [69, 105].

In this work the thermal forces are only small perturbations. This indicates that the diffusion of the helix is small compared to its translational and rotational motion due to the applied forces and torques. Also the deformation driven by thermal fluctuations become only important for filament length in the order of millimeters. Indeed this is much larger than the actual length of ten to twenty microns. Nevertheless these small fluctuations are important for the polymorphic transitions, which we will study in chapter 4. They enable the filament to cross the energy barrier between two polymorphic states.

2.3 Elasticity theory of filaments

The elasticity theory of long thin rods is based on linear elasticity. It is assumed that Hook's law is valid such that a small displacement Δx is proportional to the applied force F

$$\Delta x \sim F. \tag{2.30}$$

Nevertheless, in a long rod even a small local deformation leads to large displacements of the ends of the rod. Furthermore there are two length scales: the radius of the cross section and the length of the rod. Therefore it is difficult to apply the full three dimensional elasticity theory. To avoid the complexity the theory is rewritten in local kinematic variables that affect the center line of the rod.

To understand these local variables we first recall some basics about differential geometry of space curves. The key feature of differential geometry is to use the differential calculus to obtain geometrical invariants. Especially for space curves we want to know when two curves are equally apart from rotations or translations and what is the best local approximation of a curve.

We start in section 2.3.1 with a short summary of the Frenet theory, which is the standard theory of space curves (see for example [116]). We will explain the curvature and the torsion of a curve and show that these two geometrical invariants determine a space curve.

The class of curves where Frenet theory can be applied is very restrictive. Hence we will generalize the formalism. This leads us directly to the kinematic variables of Kirchhoff's rod theory.

2.3.1 Differential geometry of space curves

The Frenet-Serret equations

We consider a differentiable space curve $\boldsymbol{r}(s)$ parametrized by the arc length s. This ensures that the tangent vector $\boldsymbol{t} = \boldsymbol{r}'(s)$ is always normalized and the length of an arbitrary segment is given by

$$L = \int_{s_1}^{s_2} |\boldsymbol{r}'| \mathrm{d}s = s_2 - s_1. \tag{2.31}$$

It is well known that the curve $\boldsymbol{r}(s)$ can be locally approximated in first order by a straight line parallel to the tangent vector $\boldsymbol{t} = \boldsymbol{r}'$. A better approximation includes the change of the tangent $\boldsymbol{t}'$. Its absolute value is the *curvature* $\kappa = |\boldsymbol{t}'|$ and describes how much $\boldsymbol{r}$ locally deviates from a straight line. The unit vector $\boldsymbol{n} = \boldsymbol{t}'/\kappa$ is also called the normal vector. Since the tangent is a unit vector its derivative and hence the normal vector is perpendicular to it. Note that $\boldsymbol{n}$ is only well defined if the curvature is non vanishing $\kappa > 0$.

The tangent and the normal vector define the osculating plane or equally called the plane of bending. The best local second order approximation of the curve $\boldsymbol{r}(s)$ is a circle in this plane of radius κ^{-1}. If the osculating planes are equal for the whole curve $\boldsymbol{r}(s)$, it is called a planar curve. But in general for a space curve the plane of bending is different for two neighboring points. To measure the difference we introduce the binormal vector $\boldsymbol{b} = \boldsymbol{t} \times \boldsymbol{n}$. Together with the tangent and the normal vector this vector form a local right-handed orthonormal basis called Frenet frame. The vector $\boldsymbol{b}$ is also the normal vector of the osculating plane. So its derivative is a measure for the deviation of $\boldsymbol{r}$ from a planar curve. Because of the definition of the binormal its derivative $\boldsymbol{b}'$ has to be parallel or anti-parallel to the normal vector. So we define the *torsion* as $\tau = -\boldsymbol{b}' \cdot \boldsymbol{n}$, which is positive if $\boldsymbol{r}$ winds out of the osculating plane in the direction of $\boldsymbol{b}$ like a right-handed helix.

We note, the definition of the curvature κ and the torsion τ are uniquely defined for a space curve $\boldsymbol{r}$ by $\boldsymbol{t}' = \kappa\,\boldsymbol{n}$ and $\boldsymbol{b}' = -\tau\,\boldsymbol{n}$. Using the definitions one shows easily that $\boldsymbol{n}' \cdot \boldsymbol{t} = -\kappa$ and $\boldsymbol{n}' \cdot \boldsymbol{b} = \tau$. So we obtain the following set of ordinary differential equations for the Frenet frame

$$\begin{array}{rcrcl} \boldsymbol{t}' & = & & \kappa\,\boldsymbol{n}, & \\ \boldsymbol{n}' & = & -\kappa\,\boldsymbol{t} & + & \tau\,\boldsymbol{b}, \\ \boldsymbol{b}' & = & & -\tau\,\boldsymbol{n}. & \end{array} \tag{2.32}$$

For given $\kappa(s) > 0$ and $\tau(s)$ this equation has a solution $\{\boldsymbol{t}, \boldsymbol{n}, \boldsymbol{b}\}$, which is unique up to an initial rotation. By integrating the tangent we obtain the space curve $\boldsymbol{r}(s)$, which is unique except of its initial value $r(0)$. We conclude that there is a one to one relation between curvature and torsion on the one hand, and the space curve $\boldsymbol{r}$ on the other, except for a translation or rotation.

The equations (2.32) can be rewritten in a more compact form by using the notation $\{\boldsymbol{e}_1, \boldsymbol{e}_2, \boldsymbol{e}_3\} = \{\boldsymbol{n}, \boldsymbol{b}, \boldsymbol{t}\}$ and the Darboux vector $\boldsymbol{\Omega} = \tau\,\boldsymbol{t} + \kappa\,\boldsymbol{b}$ as

$$\boldsymbol{e}_i' = \boldsymbol{\Omega} \times \boldsymbol{e}_i. \tag{2.33}$$

The Darboux vector describes an infinitesimal rotation and can be interpreted as the angular velocity of the Frenet frame along the curve. In this form we easily deduce the preceding interpretation of κ and τ. The curvature describes the rotation of the tangent vector in the osculating plane around the binormal vector. This vector rotates around the tangent as a consequence of the torsion.

Another way to frame a curve

In the last section 2.3.1 we recovered that a space curve is characterized by two invariants called curvature and torsion. Nevertheless the Frenet formalism is not well defined if the curvature vanishes. In 1975 Bishop [16] presented an approach to frame a curve, which avoids these problems. In this section we summarize his arguments.

In the Frenet formalism we defined a local basis by the direction of the bending. Now we choose an arbitrary vector $\boldsymbol{e}_1$, which is perpendicular to the tangent $\boldsymbol{t} = \boldsymbol{r}'$. We claim that this vector turns along $\boldsymbol{r}(s)$ only a certain amount, which is necessary for it to remain normal. This means its derivative is always parallel to the tangent $\boldsymbol{e}_1' = -k_1\boldsymbol{t}$ with some function $k_1(s)$. Hence the vector field $\boldsymbol{e}_1(s)$ is as close to being parallel as possible without losing its normality to the space curve. We call this kind of vector field *relatively parallel*.

Now we determine k_1 by a short calculation. We start from the definition, that $\boldsymbol{e}_1$ is perpendicular to the tangent in any point, and expand it for a small perturbation $\mathrm{d}s$

$$\begin{aligned} 0 &\stackrel{!}{=} \boldsymbol{e}_1(s+\mathrm{d}s)\cdot\boldsymbol{t}(s+\mathrm{d}s), && \text{(2.34a)}\\ &= (\boldsymbol{e}_1(s)+\boldsymbol{e}_1'(s)\mathrm{d}s)\cdot(\boldsymbol{t}(s)+\boldsymbol{t}'(s)\mathrm{d}s)+O(\mathrm{d}s^2), && \text{(2.34b)}\\ &= \big(\boldsymbol{e}_1'(s)\cdot\boldsymbol{t}(s)+\boldsymbol{e}_1(s)\cdot\boldsymbol{t}'(s)\big)\mathrm{d}s. && \text{(2.34c)} \end{aligned}$$

If there is no curvature the derivative of the tangent and consequently k_1 is equal to zero. Otherwise we find $k_1 = \kappa\cos\phi$ with the curvature κ and the actual angle ϕ between $\boldsymbol{e}_1$ and the normal vector $\boldsymbol{n}$. Hence the relative parallel vector field $\boldsymbol{e}_1(s)$ and its derivative $k_1(s)$ are uniquely defined by choosing a vector $\boldsymbol{e}_1$ perpendicular to the tangent at point $\boldsymbol{r}(0)$.

Now we construct a local orthonormal basis $\{\boldsymbol{e}_1, \boldsymbol{e}_2, \boldsymbol{e}_3\}$ with $\boldsymbol{e}_3 = \boldsymbol{t}$ and $\boldsymbol{e}_2 = \boldsymbol{t}\times\boldsymbol{e}_1$. One easily shows that $\boldsymbol{e}_2$ is also relatively parallel and its derivative is given by

$$\begin{aligned} \boldsymbol{e}_2' &= \underbrace{\boldsymbol{t}'\times\boldsymbol{e}_1}+\underbrace{\boldsymbol{t}\times\boldsymbol{e}_1'}_{=0} && \text{(2.35)}\\ &= -k_2\boldsymbol{t} \qquad \text{with} \quad k_2 = \kappa\sin\phi. && \text{(2.36)} \end{aligned}$$

It directly follows that the curvature and the normal vector are given by

$$\kappa = \sqrt{k_1^2+k_2^2} \tag{2.37}$$

$$\boldsymbol{n} = \cos\phi\,\boldsymbol{e}_1 + \sin\phi\,\boldsymbol{e}_2 = \frac{k_1}{\kappa}\boldsymbol{e}_1 + \frac{k_2}{\kappa}\boldsymbol{e}_2. \tag{2.38}$$

Similarly to the Frenet formalism we obtain differential equations for the basis. Again we rewrite it by using the Darboux vector

$$\boldsymbol{e}_i' = \boldsymbol{\Omega}\times\boldsymbol{e}_i \qquad \text{with} \quad \boldsymbol{\Omega} = -k_2\boldsymbol{e}_1 + k_1\boldsymbol{e}_2. \tag{2.39}$$

Hence k_1 and k_2 describe the rotation or bending in one relatively fixed direction. The space curve $\boldsymbol{r}$ is determined uniquely by two functions up to an euclidean transformation. Contrary to the Frenet formalism in this case the functions $k_1 = \kappa\cos\phi$ and $k_2 = \kappa\sin\phi$ are only determined up to a phase shift $\phi \to \phi + \Delta\phi$. By differentiating the binormal vector $\boldsymbol{e}_3\times\boldsymbol{n}$ we obtain the relation to the torsion as $\tau = \phi'$. Thus κ and $\int\tau\mathrm{d}s$ behave like polar coordinates for the curve (k_1, k_2).

To summarize a space curve is always described by two functions (k_1, k_2) or (κ, τ) that implement the infinitesimal rotation of a local frame along the arc length. Both sets of functions behave like a special choice of a coordinate system by defining a proper local frame.

In the theory of rods we will use a material frame $\{\boldsymbol{e}_1, \boldsymbol{e}_2, \boldsymbol{e}_3\}$ with $\boldsymbol{e}_3 = \boldsymbol{r}'$. In general it will neither correspond to the Frenet nor to a relatively parallel frame. As a consequence the Darboux vector will have three non-zero components $\boldsymbol{\Omega} = (\Omega_1, \Omega_2, \Omega_3)$.

Now we analyze the relation of this general representation to the Frenet frame. Therefore we calculate the normal vector

$$\kappa \boldsymbol{n} = \boldsymbol{t}' = \boldsymbol{\Omega} \times \boldsymbol{e}_3 = -\Omega_1 \boldsymbol{e}_2 + \Omega_2 \boldsymbol{e}_1. \tag{2.40}$$

The terms Ω_1 and Ω_2 describe the bending in two directions and the total or geometric curvature is given by $\kappa = \sqrt{\Omega_1^2 + \Omega_2^2}$. In this sense Ω_3 describes the deviation of $\boldsymbol{e}_1$ and $\boldsymbol{e}_2$ from a relatively parallel frame. In the next step we compute the torsion. First we introduce the angle ϕ between $\boldsymbol{e}_1$ and the normal in equation (2.38) with

$$\sin\phi = -\Omega_1/\kappa, \qquad \cos\phi = \Omega_2/\kappa. \tag{2.41a}$$

By differentiating the binormal we obtain the torsion

$$\tau = \phi' + \Omega_3. \tag{2.41b}$$

Consequently Ω_3 is a torsion iff the ratio $\Omega_1/\Omega_2 = -\tan\phi$ is a constant.

2.3.2 Kirchhoff's rod theory

A rod or filament is a three dimensional body, where the cross sectional radius is much smaller than its arc length. The fundamental idea of Kirchhoff's rod theory is to represent the physically relevant stresses from linear elasticity theory of three dimensional bodies as cross sectional averages at each point along the axis of the filament. The theory has been published first in 1859 by Kirchhoff [68] and later extended by others [84]. A comprehensive introduction into the theory and its applications has been given by Love [84]. A short but more modern overview can be found in [32].

We describe the rod by its center line $\boldsymbol{r}_0(s)$ with the arc length s and choose for every cross section s two orthonormal vectors $\boldsymbol{e}_1$ and $\boldsymbol{e}_2$ perpendicular to the tangent $\boldsymbol{e}_3 = \boldsymbol{r}_0'(s)$, which typically corresponds to the principal axes of the cross sectional inertia tensor. In principle we can describe every point of the rod by the arc length and two coordinates for the position in the cross section. The advantage of this description with a local coordinate system compared to the usual global one is the following. A bending of one part of the rod leads to a large global displacement of e. g. the end of the filament, whereas in the local coordinate system there are still only small displacements. These small displacements can be handled by the linear elasticity theory. From this one can

derive the deformation of the material frame which is given by an vector $\boldsymbol{\Omega}$ as we learned from the previous section

$$\boldsymbol{e}_i' = \boldsymbol{\Omega} \times \boldsymbol{e}_i. \tag{2.42}$$

Because this vector contains the information about the deformation of the rod and it describes the rotation of the material frame, we call it the *rotational strain vector* $\boldsymbol{\Omega}$. The condition of small displacements is fulfilled if the cross sectional radius is large compared to e. g. the bending radius $r \gg 1/\Omega_i$. For bacterial flagella with a diameter of 0.02µm the curvature and torsion has to be small compared to 100/µm which is true also for large deformations.

We have seen that a space curve is described by only two geometrical invariants. So there always exists a frame (the Frenet frame or the relatively parallel frame) such that one component of $\boldsymbol{\Omega}$ vanishes. Nevertheless, for a physical rod all components are important. To capture the main idea we start with a straight rod which can bend in both directions $\boldsymbol{e}_1$ and $\boldsymbol{e}_2$. In addition we can twist it around its axis, which does not lead to a visible deformation but to an internal strain. For an arbitrary formed rod this kind of deformation is described by a rotation around $\boldsymbol{e}_3$ by the twist angle ϕ as given in Eq. (2.41) and shown in figure 2.6. We note, that the accurate description of the twist is the main difference between Kirchhoff's theory and other elastic models which are used to model bacterial flagella [101, 129].

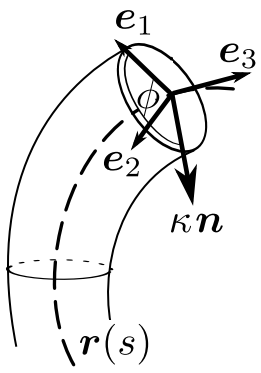

Abbildung 2.6: The conformation of a slender elastic rod

The interaction of the rotational strain vector and the actually acting forces can be described in two different ways [120]. The classical method uses force and torque balance equations, which describe how the stress is equilibrated in the rod. Additionally one needs a constitutive relation that describes how the geometry couples to the forces. The second and more modern method is based on the elastic energy as a functional of the rotational strain vector. The elastic forces are obtained by the functional derivative with respect to $\boldsymbol{r}$. In this work we use both methods. For the simulation we use the elastic energy and calculate the variational derivative numerically. The advantage of this method is that the energy can be extended to include the polymorphic forms of the bacterial flagellum. Nevertheless for our analytical investigations, i. e. the buckling theory, we use the classical method since it is easier to handle.

The classical theory

To obtain the force and torque balance equations we consider a small segment of the rod between the points $\boldsymbol{r}(s)$ and $\boldsymbol{r}(s+\mathrm{d}s)$. [1] There are internal elastic forces and torques at the ends of a segment due to the interaction with other parts of the rod. At $\boldsymbol{r}(s)$ the force is given by $\boldsymbol{F}$ and, respectively, the torque by $\boldsymbol{M}$. At the end $\boldsymbol{r}(s+\mathrm{d}s)$ we write the force as $-\boldsymbol{F}+\mathrm{d}\boldsymbol{F}$ and, respectively, the torque as $-\boldsymbol{M}+\mathrm{d}\boldsymbol{M}$. In addition there might act external forces $\boldsymbol{f}\mathrm{d}s$ and torques $\boldsymbol{m}\mathrm{d}s$ on the segment. From Newton's laws we know that in mechanical equilibrium the sum of all forces and the sum of all torques are equal to zero. This implies the force and torque balance equations

$$\boldsymbol{F}' + \boldsymbol{f} = 0, \tag{2.43a}$$

$$\boldsymbol{M}' + \boldsymbol{t} \times \boldsymbol{F} + \boldsymbol{m} = 0, \tag{2.43b}$$

where we used the tangent of the rod $\boldsymbol{t} = \boldsymbol{e}_3 = \boldsymbol{r}'$. In our case the local forces $\boldsymbol{f}$ and torques $\boldsymbol{m}$ are given by the friction.

Moreover these equations are coupled to a constitutive relation. Kirchhoff has shown that the torque in a point $\boldsymbol{r}(s)$ depends linearly on the rotational strain

$$\boldsymbol{M} = A_1(\Omega_1^0 - \Omega_1)\boldsymbol{e}_1 + A_2(\Omega_2^0 - \Omega_2)\boldsymbol{e}_2 + C(\Omega_3^0 - \Omega_3)\boldsymbol{e}_3. \tag{2.44}$$

Here we denote the spontaneous curvatures by Ω_1^0 and Ω_2^0, the spontaneous torsion by Ω_3^0, the *bending rigidities* by A_1 and A_2, and the *torsional rigidity* by C.

The bending rigidities $A_{1/2} = EI_{1/2}$ are given by the tensile modulus E and the cross sectional inertia moment $I_{1/2} = \int x_{2/1}^2 \mathrm{d}A$. In this work only circular cross sections are regarded. In this situation both bending rigidities are equal to a constant $A = A_1 = A_2$. The cross sectional inertia moment is given by $I = \pi r^4/4$ with filament radius r [74]. The torsional rigidity for a circular cross section is given by $C = G2I = G\pi r^4/2$ with the shear modulus G [74].

The bending rigidity A together with an appropriate length scale introduce characteristic values for force and elastic energy. In this work we do not use these characteristic values to rescale our physical quantities to dimensionless numbers. For an easy comparability with experiments we use for our simulations a fixed value of $A = 3.5\mathrm{pN}\mu\mathrm{m}^2$, which has been given in Ref. [28] as a typical value for bacterial flagella. To investigate the influence of the torsional rigidity C we introduce the dimensionless *twist-bend ratio* $\Gamma = C/A$. In chapter 4 we will analyze the influence of Γ on the transition between two polymorphic forms of the bacterial flagellum and we will find that $\Gamma \lessapprox 1$ is a appropriate value.

[1] The balance equations can also be derived by integrating the equations for the stress tensor of the three dimensional linear elasticity theory over the cross section of the rod (see e. g. [32, 84]).

The elastic energy and the equations of motion

Kirchhoff's rod theory leads to an elastic free energy of the form

$$\mathcal{F}\big[\boldsymbol{\Omega}(s)\big] = \int_0^L \mathfrak{f}_{\mathtt{cl}}(\boldsymbol{\Omega}, \boldsymbol{\Omega}_0)\,\mathrm{d}s, \tag{2.45}$$

$$\mathfrak{f}_{\mathtt{cl}}(\boldsymbol{\Omega}, \boldsymbol{\Omega}_0) = \frac{A}{2}\left((\Omega_1 - \Omega_1^0)^2 + (\Omega_2 - \Omega_2^0)^2 + \Gamma(\Omega_3 - \Omega_3^0)\right). \tag{2.46}$$

The constants are the same as described in the previous paragraph. It can be interpreted as a second order expansion in the angular strain $\boldsymbol{\Omega}$. Since the bacterial flagellum has a circular cross section, we are free to choose for the material frame the undeformed ground state the Frenet frame. The spontaneous rotational strain vector is given by

$$\boldsymbol{\Omega}_0 = \begin{pmatrix} 0 \\ \kappa_0 \\ \tau_0 \end{pmatrix} \tag{2.47}$$

with a spontaneous curvature κ_0, torsion τ_0, and a vanishing twist angle $\phi = 0$.

Since $\boldsymbol{\Omega}$ directly depends on the centerline $\boldsymbol{r}(s)$ and the twist angle $\phi(s)$, the total free energy is a functional $\mathcal{F}[\boldsymbol{r}(s), \phi(s)]$ in $\boldsymbol{r}(s)$ and $\phi(s)$. Hence we can write the elastic forces $\boldsymbol{f}_{\mathtt{el}}$ and the torque $m_{\mathtt{el}}\boldsymbol{e}_3$ around the filament axis as functional derivatives with respect to $\boldsymbol{r}$, and ϕ, respectively,

$$\boldsymbol{f}_{\mathtt{el}} = -\frac{\delta\mathcal{F}}{\delta\boldsymbol{r}}, \qquad\qquad m_{\mathtt{el}} = -\frac{\delta\mathcal{F}}{\delta\phi}. \tag{2.48}$$

At low Reynolds number the sum of elastic and thermal forces is balanced by a viscous drag. The same applies to the elastic and thermal torques. Using resistive force theory with local friction coefficients $\gamma_\parallel, \gamma_\perp$, and γ_R, as described in section 2.2.2, we formulate the Langevin equations

$$\left[\gamma_\parallel \boldsymbol{t}\otimes\boldsymbol{t} + \gamma_\perp(\mathbf{1} - \boldsymbol{t}\otimes\boldsymbol{t})\right]\cdot\boldsymbol{v} = \boldsymbol{f}_{\mathtt{el}} + \boldsymbol{f}_{\mathtt{th}} \tag{2.49a}$$

$$\gamma_R\omega = m_{\mathtt{el}} + m_{\mathtt{th}}. \tag{2.49b}$$

Finally the thermal force $\boldsymbol{f}_{\mathtt{th}}$ and torque $m_{\mathtt{th}}$ are Gaussian stochastic variables with zero mean: $\langle\boldsymbol{f}_{\mathtt{th}}\rangle = \mathbf{0}$ and $\langle m_{\mathtt{th}}\rangle = 0$. Their variances obey the fluctuation-dissipation theorem and therefore read

$$\langle\boldsymbol{f}_{\mathtt{th}}(t,s)\otimes\boldsymbol{f}_{\mathtt{th}}(0,0)\rangle = 2k_BT\,\delta(t)\,\delta(s)\left[\gamma_\parallel\boldsymbol{t}\otimes\boldsymbol{t} + \gamma_\perp(\mathbf{1} - \boldsymbol{t}\otimes\boldsymbol{t})\right], \tag{2.50a}$$

$$\langle m_{\mathtt{th}}(t,s)m_{\mathtt{th}}(0,0)\rangle = 2k_BT\,\delta(t)\,\delta(s)\,\gamma_R, \tag{2.50b}$$

$$\langle m_{\mathtt{th}}(t,s)\boldsymbol{f}_{\mathtt{th}}(0,0)\rangle = \mathbf{0}. \tag{2.50c}$$

We note, the analytical derivation of the functional derivatives is rather complicated due to the constraint of a constant arc length (see e. g. [115,117,120,139,140]). Therefore we will introduce in section 2.4 a numerical variation scheme where we implement the in-extensibility condition with a stretching potential.

2.3.3 A brief introduction into the theory of buckling

In chapter 3 we will investigate a motor driven flagellum and show that it buckles under its thrust force, which is induced by the rotation, at a critical motor torque. We will present a sophisticated analytical model for the buckling transition based on a helical rod, which quantitatively reproduces the critical force-torque relation obtained in simulations. Therefore we present an introduction to the basic ideas of the classical buckling theory that goes back to Euler [34].

Stability of rod subjected to twisting couple and thrust on its ends

We first investigate the case of a rod subjected to torques and forces only on the ends. The interested reader is referred to the books of Love [84] and Landau & Lifshitz [74] for more details about elasticity.

We assume a straight rod with length L_0 aligned to the z axis such that $\boldsymbol{r} = s\boldsymbol{e}_3 = (0, 0, z)^t$. Then we apply a constant force $\boldsymbol{F} = F\boldsymbol{e}_3$ and a torque $\boldsymbol{M} = M_t\boldsymbol{e}_3$ at the ends of the rod parallel to the rod axis. Then the straight rod with a twist $\Omega_3 = M_t/C$ is a trivial solution of force and torque balance equations (2.43) (without force and torque densities $\boldsymbol{f} = \boldsymbol{m} = 0$) and the constitutive equation (2.44).

Now we study a small disturbance $X(z)$ and $Y(z)$ in the x and y direction, respectively. Then we expand all equations up to first order in these coordinates and its derivatives. As long as X and Y are small compared to the rod length L_0 we identify the arc length s with z. Our aim is to derive linear differential equations for $X(z)$ and $Y(z)$ as a function of z from the general equations (2.43) and (2.44). In general these linear equations only have one trivial solution, but at the bifurcation point there are also non trivial ones. We will deduce this in the following paragraphs.

The position vector and its derivatives with respect to z now read as

$$\boldsymbol{r} = \begin{pmatrix} X(z) \\ Y(z) \\ z \end{pmatrix}, \qquad \boldsymbol{r}' = \begin{pmatrix} X'(z) \\ Y'(z) \\ 1 \end{pmatrix}, \qquad \boldsymbol{r}'' = \begin{pmatrix} X''(z) \\ Y''(z) \\ 0 \end{pmatrix}. \tag{2.51}$$

Note that the absolute value of $\boldsymbol{r}'$ is equal to one up to second order in x and y. Hence it is equal to the tangent vector $\boldsymbol{e}_3$. This justifies our assumption $s \approx z$.

The curvature is given by the rotation of the tangent with respect to the rotational strain vector $\boldsymbol{e}_3' = \boldsymbol{\Omega} \times \boldsymbol{e}_3$. This equation determines the first two components of $\boldsymbol{\Omega}$. We obtain

$$\Omega_1 = -Y'', \qquad \Omega_2 = X''. \tag{2.52}$$

Using this in the constitutive equation (2.44) the total moment $\boldsymbol{M}$ is given by

$$\boldsymbol{M} = A \begin{pmatrix} -Y''(z) \\ X''(z) \\ 0 \end{pmatrix} + M_t\boldsymbol{e}_3. \tag{2.53}$$

Here we assumed that the twist $\Omega_3 = M_t/C$ remains constant under a small perturbation.

Now we rescale our quantities as

$$\frac{z}{L_0} \to \tilde{z}, \qquad \frac{ML_0}{A} \to \tilde{M}, \qquad \frac{FL_0^2}{A} \to \tilde{F}. \tag{2.54}$$

We find that the force $\tilde{F}$ is constant along the filament due to the force balance equation (2.43a) without an additional force density. We use the torque (2.53) together with the torque balance equation (2.43b) and obtain the following coupled linear differential equations for $X(\tilde{z})$ and $Y(\tilde{z})$

$$-Y''' + \tilde{M}_t X'' - Y'\tilde{F} = 0 \tag{2.55a}$$

$$X''' + \tilde{M}_t Y'' + X'\tilde{F} = 0. \tag{2.55b}$$

Additionally one has to fulfill certain boundary conditions depending on physical conditions. If these equations have more than the trivial solution $X = Y = 0$ the solution of the full equations (2.43) branches out such that there is a bifurcation point.

Note that for a zero torque $\tilde{M}_t = 0$ the equations decouple. These cases could be easily solved using an harmonic ansatz. For more details consider [74, 84].

Example: rod with hinged ends We speak of hinged ends if the endpoints of the rod are fixed ($X(0) = Y(0) = X(1) = Y(1) = 0$) but the tangents are free to move. It follows that at the ends the torque (2.53) acts only in the z direction whereas the x and y components cancel each other

$$X''(0) + \tilde{M}_t Y'(0) = 0 \qquad Y''(0) - \tilde{M}_t X'(0) = 0 \tag{2.56}$$

$$X''(1) + \tilde{M}_t Y'(1) = 0 \qquad Y''(1) - \tilde{M}_t X'(1) = 0. \tag{2.57}$$

We solve equations (2.55) with the ansatz

$$X = a\sin(q_1\tilde{z} + \alpha_1) + b\sin(q_2\tilde{z} + \alpha_2) \tag{2.58a}$$

$$Y = a\cos(q_1\tilde{z} + \alpha_1) + b\cos(q_2\tilde{z} + \alpha_2). \tag{2.58b}$$

It follows that $q_{1,2}$ are solutions of the quadratic equation $q^2 + \tilde{M}_t q - \tilde{F} = 0$. Using the boundary conditions we obtain the bifurcation criteria

$$\pi^2 = \tilde{M}_t^2/4 + \tilde{F} \tag{2.59}$$

$$= F_c\frac{L_0^2}{A} + \frac{1}{4}M_c^2\left(\frac{L_0}{A}\right)^2. \tag{2.60}$$

The critical force F_c and the critical torque M_c separate two regions, where the rod remains straight or buckles under the applied forces and torques, as we show in figure 2.7.

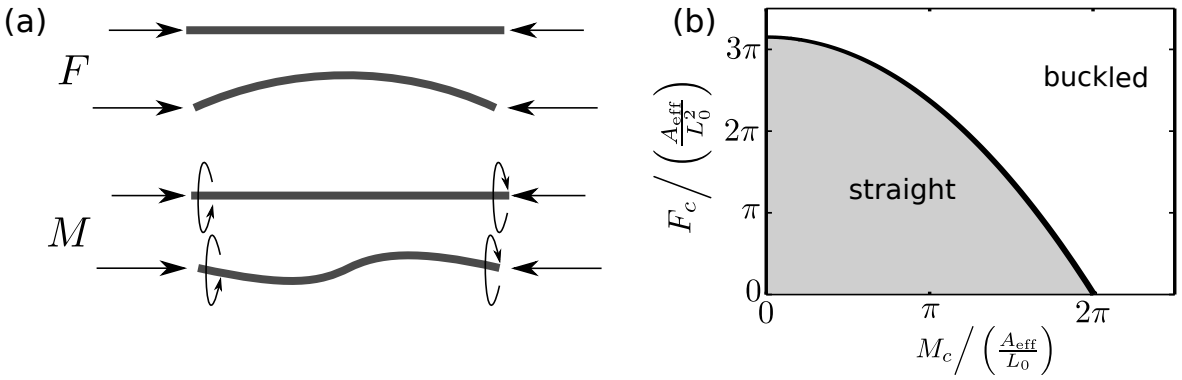

Abbildung 2.7: **(a)** An elastic rod buckles under the influence of a compressional force F and an external torque M. **(b)** The critical values F_c and M_c where buckling occurs obey a characteristic relation. The graph depicts relation (2.60) valid for a rod with hinged ends.

The quadratic dependency of the critical force on the critical torque reflects that the buckling instability should not depend on the direction of the applied torque. In contrast the direction of the force is important. If the force is positive the rod is compressed, which leads to a buckling, but if the force is negative sufficient tension stabilizes the rod against a torque.

Stability of a rod rotating at low Reynolds number

In the last decade elastic instabilities were reported in the dynamics of rods at low Reynolds number. Here typically a torque is applied at one end of the filament. The rod rotates and the applied torque is balanced by frictional forces and torques continuously distributed along the filament. Wolgemuth *et al.* [132] have investigated a rod with one clamped and one free end rotating around its axis. They have observed two regimes separated by a supercritical (*i. e.* continues) Hopf bifurcation. When the rotational frequency exceeds a critical value, the straight filament starts to bend and performs a whirling motion. In Brownian dynamics simulations Wada and Netz [123] have observed for the same conditions a subcritical (*i. e.* discontinuous) Hopf bifurcation, where the strongly bent filament nearly folds back on itself.

A rod tilted with respect to the rotational axis bends slightly due to friction at low rotational velocity. At a critical value a discontinuous transition to a helical rod shape occurs [88, 89].

In chapter 3 we consider buckling instabilities for the biologically relevant helical filament. The problem is more complex due to the characteristic rotation-translation coupling and the fact that we do not fix the orientation of the helical filament.

2.4 The numerical scheme

Our aim is to construct a numerical scheme, that calculates the local forces acting on a discretized filament by variation of an elastic free energy

$$\mathcal{F} = \int_0^L \mathfrak{f}_{\mathtt{rot}}(\boldsymbol{\Omega}) + \mathfrak{f}_{\mathtt{str}} \, \mathrm{d}s \tag{2.61}$$

that is given by the integral over the arc length of an elastic energy density $\mathfrak{f}_{\mathtt{rot}}(\boldsymbol{\Omega})$ due to the rotational strain $\boldsymbol{\Omega}$. To avoid a constraint for the in-extensibility of the filament we add a free energy for the stretching of the filament $\mathfrak{f}_{\mathtt{str}}$ such that the changes in the filament length are negligible. Discretizing the filament enables us to write the integral of the energy densities as a sum. Then the forces acting on the filament are given by the gradient of the energy with respect to the discrete points. Our approach to derive the variational derivatives of the elastic energy numerically enables us in chapter 4 to test different extensions of the Kirchhoff elastic energy needed to describe the polymorphic transformations of bacterial flagella.

We develop a technique, which is based on the work of Reichert [100] and which is similar to the one of Chirico and Langowski [25] and Wada and Netz [123–128] who studied simulations of helical nano springs etc.

2.4.1 The discretized filament

We start by discretizing the centerline of the filament $\boldsymbol{r}(s)$ of the form

$$\boldsymbol{r}^{(n)} = \boldsymbol{r}(hn) \qquad \text{with } n = 0, \ldots, N. \tag{2.62}$$

The total length $L = Nh$ of the filament is given by the discretization length h and the number of segments N. At every point $\boldsymbol{r}^{(n)}$ we attach a tripod $\{\boldsymbol{e}_1^{(n)}, \boldsymbol{e}_2^{(n)}, \boldsymbol{e}_3^{(n)}\}$ and approximate the tangent vector by

$$\boldsymbol{e}_3^{(n)} = \frac{\boldsymbol{r}^{(n)} - \boldsymbol{r}^{(n-1)}}{|\boldsymbol{r}^{(n)} - \boldsymbol{r}^{(n-1)}|} \qquad \text{for } n > 0. \tag{2.63}$$

For $n = 0$ we choose the vector $\boldsymbol{e}_3^{(0)}$ to fulfill the boundary conditions for the starting point $s = 0$ of the filament. The transformation of two neighboring tripods into one another is a rotation[2] $\mathbf{R}(h|\boldsymbol{\Omega}|, \boldsymbol{\Omega}^{(n)})$ around a vector $\boldsymbol{\Omega}^{(n)}$ by an angle $h|\boldsymbol{\Omega}^{(n)}|$. The difference between these two tripods is then given by

$$\boldsymbol{e}_i^{(n+1)} - \boldsymbol{e}_i^{(n)} = (\mathbf{R}(h|\boldsymbol{\Omega}|, \boldsymbol{\Omega}^{(n)}) - \mathbf{1}) \cdot \boldsymbol{e}_i^{(n)}. \tag{2.64}$$

[2] The rotation $\mathbf{R}(\alpha, a\boldsymbol{n})$ of a vector $\boldsymbol{v}$ around an axis defined by the unit vector $\boldsymbol{n}$ by an angle α is given by

$$\mathbf{R}(\alpha, a\boldsymbol{n}) \cdot \boldsymbol{v} = (\boldsymbol{n} \otimes \boldsymbol{n}) \cdot \boldsymbol{v} + \cos\alpha \, (\mathbf{1} - \boldsymbol{n} \otimes \boldsymbol{n}) \cdot \boldsymbol{v} + \sin\alpha \, (\boldsymbol{n} \times \boldsymbol{v}).$$

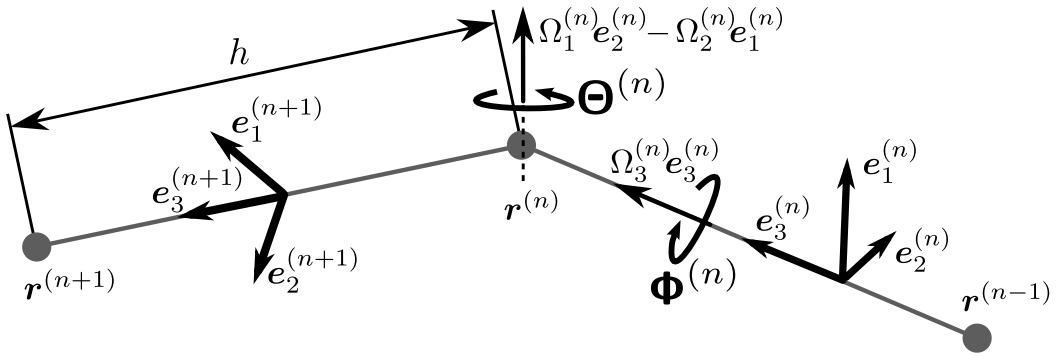

Abbildung 2.8: The discretization scheme.

We divide this equation by the discretization length and take the limit $h \to 0$. Hence we obtain on the left hand side of Eq. (2.64) the first derivative of $\boldsymbol{e}_i(hn)$. On the right hand side we gain a skew symmetric matrix describing an infinitesimal rotation of $\boldsymbol{e}_i^{(n)}$ that can be written in the form $\boldsymbol{\Omega}^{(n)} \times \boldsymbol{e}_i^{(n)}$. Consequently the vector $\boldsymbol{\Omega}^{(n)}$ is the rotational strain vector of the filament.

The strain vector describes two physical rotations: the twist about the tangent $\boldsymbol{e}_3$ and the bending, i. e. the rotation of the tangent itself. Hence it is useful to split the rotation around $\boldsymbol{\Omega}^{(n)}$ into two independent rotations reflecting the physical behavior. First we rotate around the tangent representing the twist and after that around the binormal to bend the filament

$$\mathbf{R}(h|\boldsymbol{\Omega}|, \boldsymbol{\Omega}^{(n)}) = \boldsymbol{\Theta}^{(n)} \cdot \boldsymbol{\Phi}^{(n)} + O(h^2) \tag{2.65a}$$

with

$$\boldsymbol{\Phi}^{(n)} = \mathbf{R}(h\Omega_3^{(n)}, \boldsymbol{e}_3^{(n)}). \tag{2.65b}$$

$$\boldsymbol{\Theta}^{(n)} = \mathbf{R}(h\kappa^{(n)}, \Omega_1^{(n)}\boldsymbol{e}_2^{(n)} - \Omega_2^{(n)}\boldsymbol{e}_1^{(n)}), \quad \text{and } \kappa = \sqrt{\Omega_1^2 + \Omega_2^2}. \tag{2.65c}$$

In general the sequential order of the performed rotations is important. Since the discretization is only accurate up to first order in h, we do not make an additional error. The used sequence of rotation is adopted from [100]. We sketch the discretized model in figure 2.8.

To determine the components of the strain vector we apply the rotation to the basis vectors. We start with the tangent $\boldsymbol{e}_3^{(n)}$ to derive the components of the normal vector. The rotation $\boldsymbol{\Phi}^{(n)}$ does not affect the tangent whereas the rotation around the binormal leads to

$$\boldsymbol{e}_3^{(n+1)} = \cos(h\kappa^{(n)})\boldsymbol{e}_3^{(n)} + \frac{\sin(h\kappa^{(n)})}{\kappa}\left(\Omega_1^{(n)}\boldsymbol{e}_1^{(n)} + \Omega_2^{(n)}\boldsymbol{e}_2^{(n)}\right), \tag{2.66}$$

so we obtain

$$\Omega_1^{(n)} = \frac{\kappa^{(n)}}{\sin(h\kappa^{(n)})} \boldsymbol{e}_1^{(n)} \cdot \boldsymbol{e}_3^{(n+1)} \tag{2.67a}$$

$$\approx \frac{\boldsymbol{e}_1^{(n)} \cdot \boldsymbol{e}_3^{(n+1)}}{h} \left(1 + \frac{(h\kappa^{(n)})^2}{6}\right), \tag{2.67b}$$

$$\Omega_2^{(n)} = \frac{\kappa^{(n)}}{\sin(h\kappa^{(n)})} \boldsymbol{e}_2^{(n)} \cdot \boldsymbol{e}_3^{(n+1)} \tag{2.67c}$$

$$\approx \frac{\boldsymbol{e}_2^{(n)} \cdot \boldsymbol{e}_3^{(n+1)}}{h} \left(1 + \frac{(h\kappa^{(n)})^2}{6}\right). \tag{2.67d}$$

The actual rotation angle $h\kappa^{(n)}$ is determined by the scalar product $\boldsymbol{e}_3^{(n)} \cdot \boldsymbol{e}_3^{(n+1)}$ of the two tangents or by the scalar product of the cross product $\boldsymbol{e}_3^{(n)} \times \boldsymbol{e}_3^{(n+1)}$ of the two tangents and the binormal vector $\frac{\Omega_1^{(n)}}{\kappa^{(n)}} \boldsymbol{e}_2^{(n)} - \frac{\Omega_2^{(n)}}{\kappa^{(n)}} \boldsymbol{e}_1^{(n)}$:

$$\boldsymbol{e}_3^{(n)} \cdot \boldsymbol{e}_3^{(n+1)} = \cos(h\kappa^{(n)}) \approx 1 - \frac{(h\kappa^{(n)})^2}{2}, \tag{2.68a}$$

$$\boldsymbol{e}_3^{(n)} \times \boldsymbol{e}_3^{(n+1)} = \sin((h\kappa^{(n)})) \left(\frac{\Omega_1^{(n)}}{\kappa^{(n)}} \boldsymbol{e}_2^{(n)} - \frac{\Omega_2^{(n)}}{\kappa^{(n)}} \boldsymbol{e}_1^{(n)}\right). \tag{2.68b}$$

To receive the component $\Omega_3^{(n)}$ we analyze the rotation of the vector $\boldsymbol{e}_1^{(n)}$ into $\boldsymbol{e}_1^{(n+1)}$. Instead of calculating the full rotation we rotate $\boldsymbol{e}_1^{(n)}$ with $\boldsymbol{\Phi}^{(n)}$ and $\boldsymbol{e}_1^{(n+1)}$ with the inverse of $\boldsymbol{\Theta}^{(n)}$

$$\boldsymbol{\Phi}^{(n)} \cdot \boldsymbol{e}_1^{(n)} = (\boldsymbol{\Theta}^{(n)})^{-1} \cdot \boldsymbol{e}_1^{(n+1)} \tag{2.69}$$

and take the scalar product with $\boldsymbol{e}_2^{(n)}$. The left-hand side simplifies to $\sin(h\Omega_3^{(n)})$. To evaluate the right hand side we use the identities (2.67a), (2.67c) and (2.68). So we compute

$$\begin{aligned}\sin(h\Omega_3^{(n)}) = {} & (\boldsymbol{e}_3^{(n)} \cdot \boldsymbol{e}_3^{(n+1)})(\boldsymbol{e}_2^{(n)} \cdot \boldsymbol{e}_1^{(n+1)}) - (\boldsymbol{e}_2^{(n)} \cdot \boldsymbol{e}_3^{(n+1)})(\boldsymbol{e}_3^{(n)} \cdot \boldsymbol{e}_1^{(n+1)}) \\ & + \frac{(\boldsymbol{e}_1^{(n)} \cdot \boldsymbol{e}_3^{(n+1)})(\boldsymbol{e}_3^{(n)} \cdot \boldsymbol{e}_2^{(n+1)})}{1 + (\boldsymbol{e}_3^{(n)} \cdot \boldsymbol{e}_3^{(n+1)})}.\end{aligned} \tag{2.70}$$

Now we know the dependency of $\boldsymbol{\Omega}^{(n+1)}$ on the surrounding tripods. In the next step we will determine the variations of the tripod through a variation of the position vectors of the discretized filament and the local twist to calculate the forces and twisting moments.

2.4.2 Elastic forces and torques

We discretized the space curve $\boldsymbol{r}(s)$ into $N+1$ points or N segments where every point has a local frame. The rotation of these tripods is related to N vectors $\boldsymbol{\Omega}^{(n)}$ that are identified with the rotational strain. Now we discretize the elastic energy (2.61) of the filament by approximating the integral by a sum. The part that ensures the in-extensibility reads as

$$\mathcal{F}_{\mathtt{str}} = \sum_{i=0}^{N-1} \frac{K}{2}(|\boldsymbol{r}^{(i+1)} - \boldsymbol{r}^{(i)}| - h)^2 \tag{2.71}$$

with the spring constant K. It is straight forward to calculate the force analytically and hence we obtain

$$\boldsymbol{F}^{(n)}_{\mathtt{str}} = K\Big[(|\boldsymbol{r}^{(n+1)} - \boldsymbol{r}^{(n)}| - h)\boldsymbol{e}_3^{(n+1)} - (|\boldsymbol{r}^{(n)} - \boldsymbol{r}^{(n-1)}| - h)\boldsymbol{e}_3^{(n)}\Big]. \tag{2.72}$$

The discretized energy due to the rotational strain vector is given by

$$\mathcal{F}_{\mathtt{rot}}(\{\boldsymbol{\Omega}^{(n)}\}) = \sum_{i=0}^{N-1} h\, \mathfrak{f}(\boldsymbol{\Omega}^{(i)}) + O(h^2). \tag{2.73}$$

From the energy we obtain the torque around the local axis due to the twist ϕ. We derive the torque numerically by replacing the derivative with respect to the twist by a difference quotient [96]

$$\boldsymbol{M}^{(n)}_{\mathtt{el}} = -\boldsymbol{e}_3^{(n)} \frac{\partial \mathcal{F}_{\mathtt{rot}}\big(\{\boldsymbol{\Omega}^{(k)}(\{\phi^{(l)}\})\}\big)}{\partial \phi^{(n)}} \tag{2.74a}$$

$$\approx \boldsymbol{e}_3^{(n)} \frac{\mathcal{F}_{\mathtt{rot}}\big(\{\boldsymbol{\Omega}^{(k)}(\{..., \phi^{(n)} - \delta\phi, ...\})\}\big) - \mathcal{F}_{\mathtt{rot}}\big(\{\boldsymbol{\Omega}^{(k)}(\{..., \phi^{(n)} + \delta\phi, ...\})\}\big)}{2\delta\phi} \tag{2.74b}$$

We do not have to calculate the actual twist angle $\phi^{(n)}$. The twist variation $\delta\phi$ leads to a small rotational variation of the vectors $\boldsymbol{e}_1^{(n)}$ and $\boldsymbol{e}_2^{(n)}$ of the form

$$\delta\boldsymbol{e}_1^{(n)} = \cos(\delta\phi)\boldsymbol{e}_1^{(n)} + \sin(\delta\phi)\boldsymbol{e}_2^{(n)} \approx \delta\phi\, \boldsymbol{e}_2^{(n)}, \tag{2.75a}$$

$$\delta\boldsymbol{e}_2^{(n)} = \cos(\delta\phi)\boldsymbol{e}_2^{(n)} - \sin(\delta\phi)\boldsymbol{e}_1^{(n)} \approx -\delta\phi\boldsymbol{e}_1^{(n)}, \tag{2.75b}$$

which are used together with Eqs. (2.67a), (2.67c) and (2.70) to determine the change of the rotational strain.

We derive the forces numerically by small displacements in the position vectors of the discretization points $\boldsymbol{r}^{(n)} + \delta\boldsymbol{r}^{(n)}$

$$\boldsymbol{F}^{(n)}_{\mathtt{rot}} = -\nabla_{\boldsymbol{r}^{(n)}} \mathcal{F}_{\mathtt{rot}}\big(\{\boldsymbol{\Omega}^{(k)}(\{\boldsymbol{r}^{(l)}\})\}\big) \tag{2.76a}$$

$$\approx \frac{\mathcal{F}_{\mathtt{rot}}\big(\{\boldsymbol{\Omega}^{(k)}(\{..., \boldsymbol{r}^{(n)} - \delta\boldsymbol{r}, ...\})\}\big) - \mathcal{F}_{\mathtt{rot}}\big(\{\boldsymbol{\Omega}^{(k)}(\{..., \boldsymbol{r}^{(n)} + \delta\boldsymbol{r}, ...\})\}\big)}{2\delta\boldsymbol{r}} \tag{2.76b}$$

Hence for each component of $\boldsymbol{F}^{(n)}_{\mathtt{rot}}$ we calculate the differential quotient with respect to δx, δy, and, respectively, δz.

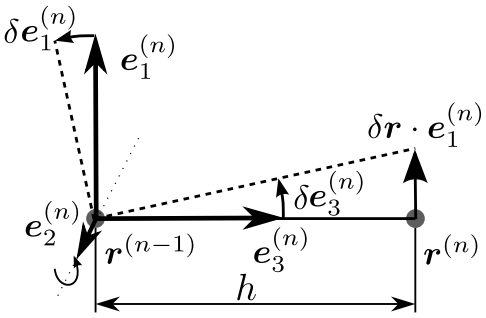

Abbildung 2.9: Rotation of the frame n due to a displacement $\delta \boldsymbol{r}$ of $\boldsymbol{r}^{(n)}$.

Now we determine how the variation $\delta \boldsymbol{r}$ affects $\boldsymbol{\Omega}^{(n)}$. A displacement of $\boldsymbol{r}^{(n)}$ parallel to the tangents $\boldsymbol{e}_3^{(n)}$ or $\boldsymbol{e}_3^{(n+1)}$ generates the restoring force (2.72). A perpendicular displacement leads to a small rotation of the local frames. Since the displacements are small we split up the rotation: one around $\boldsymbol{e}_1^{(n)}$ and another one around $\boldsymbol{e}_2^{(n)}$. The angle of the rotation around $\boldsymbol{e}_2^{(n)}$ is determined by the projection of the displacement into the $\boldsymbol{e}_1^{(n)}$ direction divided by the segment length. This can be seen in figure 2.9. The same argument holds for a rotation around $\boldsymbol{e}_1^{(n)}$. So we obtain the variations of the frame n due to the variation of $\boldsymbol{r}^{(n)}$

$$\delta \boldsymbol{e}_{1/2}^{(n)} = -(\boldsymbol{e}_3 \otimes \boldsymbol{e}_{1/2})^{(n)} \cdot \frac{\delta \boldsymbol{r}^{(n)}}{h}, \tag{2.77a}$$

$$\delta \boldsymbol{e}_3^{(n)} = \left((\boldsymbol{e}_1 \otimes \boldsymbol{e}_1)^{(n)} + (\boldsymbol{e}_2 \otimes \boldsymbol{e}_2)^{(n)}\right) \cdot \frac{\delta \boldsymbol{r}^{(n)}}{h}. \tag{2.77b}$$

The tripod $n+1$ is also rotated by the variation of $\boldsymbol{r}^{(n)}$ but in the opposite direction

$$\delta \boldsymbol{e}_{1/2}^{(n+1)} = (\boldsymbol{e}_3 \otimes \boldsymbol{e}_{1/2})^{(n+1)} \cdot \frac{\delta \boldsymbol{r}^{(n)}}{h}, \tag{2.77c}$$

$$\delta \boldsymbol{e}_3^{(n+1)} = -\left((\boldsymbol{e}_1 \otimes \boldsymbol{e}_1)^{(n+1)} + (\boldsymbol{e}_2 \otimes \boldsymbol{e}_2)^{(n+1)}\right) \cdot \frac{\delta \boldsymbol{r}^{(n)}}{h}. \tag{2.77d}$$

Together with Eqs. (2.67a), (2.67c) and (2.70) we derive the change of the rotational strain.

2.4.3 Equations of motion and boundary conditions

The equations of motion (2.49) are given in the discretized version by

$$\left[h\gamma_{\parallel}(\boldsymbol{t} \otimes \boldsymbol{t})^{(n)} + h\gamma_{\perp}(\mathbf{1} - (\boldsymbol{t} \otimes \boldsymbol{t})^{(n)})\right] \frac{\partial \boldsymbol{r}^{(n)}}{\partial t} = \boldsymbol{F}_{\mathtt{rot}}^{(n)} + \boldsymbol{F}_{\mathtt{str}}^{(n)} + \boldsymbol{F}_{\mathtt{th}}^{(n)}, \tag{2.78a}$$

$$h\gamma_R \boldsymbol{e}_3^{(n)} \omega^{(n)} = \boldsymbol{M}_{\mathtt{rot}}^{(n)} + \boldsymbol{M}_{\mathtt{th}}^{(n)}, \tag{2.78b}$$

$$\text{with } \boldsymbol{t}^{(n)} = \frac{\boldsymbol{e}_3^{(n)} + \boldsymbol{e}_3^{(n+1)}}{2}. \tag{2.78c}$$

We solve these equations with and without thermal noise. Without thermal noise the force $\boldsymbol{F}_{\mathtt{th}}^{(n)}$ and torque $\boldsymbol{M}_{\mathtt{th}}^{(n)}$ are constantly zero. In this case we solve the equations using an embedded Runge-Kutta method with adaptive step size control using the Cash-Karp parameters [96].

For the simulations with thermal noise we use the simple Euler method [69]. As time step Δt we use the same as for the Runge-Kutta method but reduced by a factor of ten. The random numbers are generated with the Mersenne Twister mt19937. According to the documentation of the GNU Scientific Library it is one of the fastest algorithm appropriate for scientific simulations [105]. To obey the fluctuation-dissipation theorem for the random forces and torques we use Gaussian distributed random numbers in every time step, centered around zero with second moments of $\left\langle F_{\parallel/\perp}^2 \right\rangle = 2k_BT\gamma_{\parallel/\perp}/\Delta t$ for the parallel and perpendicular components of the force, respectively, and $\langle M_{\mathtt{th}} \rangle = 2k_BT\gamma_R/\Delta t$ for the twist around the tangent.

We apply specific boundary conditions on both ends of the filament. Furthermore external forces may be added to the equations of motion. At the end $s = L$ we regard only torque free conditions which are automatically fulfilled. At the top $s = 0$ of the filament we attached the tripod $\{\boldsymbol{e}_1^{(0)}, \boldsymbol{e}_2^{(0)}, \boldsymbol{e}_3^{(0)}\}$ that determines the orientation of the filament. If we keep it fixed in time during the simulations we obtain a clamped filament. Otherwise we need an additional equation of motion that describes the rotation $\boldsymbol{\omega}$ of the material frame. This is achieved by balancing all the torques acting on it

$$\begin{aligned}\left[\gamma_R h(\boldsymbol{e}_3 \otimes \boldsymbol{e}_3)^{(0)} + \frac{1}{2}\gamma_\perp h^3(\mathbf{1} - (\boldsymbol{e}_3 \otimes \boldsymbol{e}_3)^{(0)})\right] \cdot \boldsymbol{\omega} \\ = \boldsymbol{M}_{\mathtt{ext}} - A[\Omega_1 \boldsymbol{e}_1^{(0)} + (\Omega_2 - \kappa_0)\boldsymbol{e}_2^{(0)}] - C(\Omega_3 - \tau_0)\boldsymbol{e}_3^{(0)}.\end{aligned} \tag{2.79}$$

It gives rise to a frictional torque decomposed into a component along the tangent vector $\boldsymbol{e}_3^{(0)}$ and one perpendicular to it. The frictional torque is balanced by the elastic torque $-\delta\mathcal{F}/\delta\boldsymbol{\Omega}$ and an external torque $\boldsymbol{M}_{\mathtt{ext}}$, e. g. the motor torque.

Limits of the model

In the discrete model for the coupling of the rotational strain to the filament we assumed small angles given by the discretization length times the curvature or twist. In the simulations we use a discretization length corresponding to $h = 0.2\mu\text{m}$, which is the upper limit to describe bending and twist up to $3/\mu\text{m}$. In this work we are mainly interested in the normal and coiled forms of bacterial flagella where the last assumption is fulfilled.

For the derivation of the bending force we assumed that the discretization length h remains constant. Regarding its change would lead to higher order corrections that we neglected before. Therefore we ensure that the restoring force due to the stretching potential (2.72) is large enough to keep the distance between two knots approximately constant. The typical forces on the filament are below 5pN. To keep the variation of the discretization length $|1 - |\boldsymbol{r}^{(n)} - \boldsymbol{r}^{n-1)}|/h|$ below 1% we need a spring constant of $K = 1000\text{pN}/\mu\text{m}$. We will only use large forces in chapter 4 where we will observe a relative stretching in the order of 1.5%.

2.5 Theory of helical springs

2.5.1 The helical geometry

A helix or circular helix is a straight curve on the surface of a cylinder of radius R. This can be easily seen if we cut the cylinder parallel to its axis and wind it up to a plane as sketched in figure 2.10. Using cylindrical coordinates we find a simple parameterization by the azimuthal angle

$$\boldsymbol{r}(\varphi) = \begin{pmatrix} R\cos\varphi \\ R\sin\varphi \\ P\varphi/2\pi \end{pmatrix}. \tag{2.80}$$

The height, which the helix gains with one turn, is called the pitch P.

For the calculations we need a parameterization by the arc length s. Therefore we introduce the pitch angle α between a cross section of the cylinder and the space curve. It corresponds to the slope of the line on the surface. Furthermore we need the increase k of the angle $\varphi = ks$ per length. Note that the length of one coil is given by $L_{\texttt{coil}} = 2\pi/k$. So we obtain the parameterization

$$\boldsymbol{r}(s) = \begin{pmatrix} R\cos ks \\ R\sin ks \\ \sin\alpha s \end{pmatrix}. \tag{2.81}$$

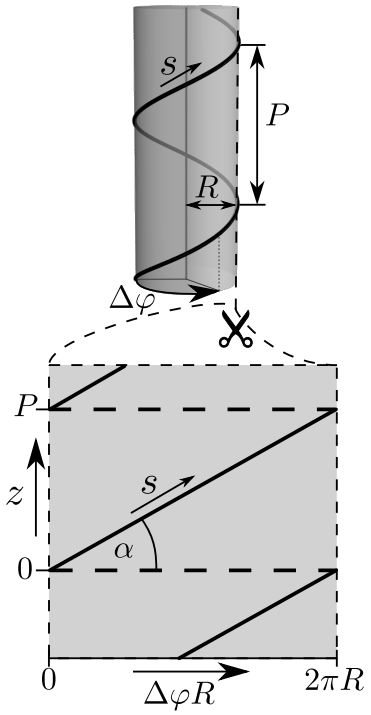

Abbildung 2.10: A helix is a straight line on the surface of a cylinder.

If the length of the derivative $\boldsymbol{r}'$ of $\boldsymbol{r}$ with respect to s is equal to one then s is the arc length resulting in the condition for the radius $R = \cos\alpha/k$. Now we derive the Frenet frame of the helix as described in section 2.3.1 and find

$$\boldsymbol{t} = \begin{pmatrix} -\cos\alpha\sin(ks) \\ \cos\alpha\cos(ks) \\ \sin\alpha \end{pmatrix}, \quad \boldsymbol{n} = -\begin{pmatrix} \cos(ks) \\ \sin(ks) \\ 0 \end{pmatrix}, \quad \boldsymbol{b} = \begin{pmatrix} \sin\alpha\sin(ks) \\ -\sin\alpha\cos(ks) \\ \cos\alpha \end{pmatrix}. \tag{2.82}$$

Using this frame we calculate the curvature κ and torsion τ

$$\kappa = k\cos\alpha, \qquad \tau = k\sin\alpha. \tag{2.83}$$

Note that the curvature and the torsion of a helix are constant along the whole filament. Hence they are the simplest form of a three dimensional space curve and every other curve can be approximated locally by them. This is the reason why helices and their variations are often be found in technique and nature (see i. e. [15,19,26,91,116,117,127])

We summarize the different parameterizations of the helix and how they are related to each other in table 2.2.

$(x,y,z)^{\mathrm{T}}$	R,P,φ	α,k,s	κ,τ,s
R,P,φ	$\boldsymbol{r}(\varphi)=\begin{pmatrix}R\cos\varphi\\R\sin\varphi\\P\varphi/2\pi\end{pmatrix}$	$R=\cos\alpha/k$ $P=2\pi\sin\alpha/k$	$R=\dfrac{\kappa}{\kappa^2+\tau^2}$ $P=2\pi\dfrac{\tau}{\kappa^2+\tau^2}$
α,k,s	$\tan\alpha=\dfrac{P}{2\pi R}$ $k=\dfrac{2\pi}{\sqrt{P^2+(2\pi R)^2}}$	$\boldsymbol{r}(s)=\begin{pmatrix}\frac{1}{k}\cos\alpha\cos(ks)\\\frac{1}{k}\cos\alpha\sin(ks)\\\sin(\alpha)s\end{pmatrix}$	$\tan\alpha=\tau/\kappa$ $k=\sqrt{\kappa^2+\tau^2}$
κ,τ,s	$\kappa=\dfrac{R}{R^2+(P/2\pi)^2}$ $\tau=\dfrac{P/2\pi}{R^2+(P/2\pi)^2}$	$\kappa=k\cos\alpha$ $\tau=k\sin\alpha$	$\boldsymbol{r}(s)=\begin{pmatrix}\frac{\kappa}{\kappa^2+\tau^2}\cos\left(\sqrt{\kappa^2+\tau^2}s\right)\\\frac{\kappa}{\kappa^2+\tau^2}\sin\left(\sqrt{\kappa^2+\tau^2}s\right)\\\frac{\tau}{\sqrt{\kappa^2+\tau^2}}s\end{pmatrix}$

Tabelle 2.2: Different parameterizations of a helix.

2.5.2 Effective compressional and torsional rigidity of a helix

Combined force and torque

We investigate the uniform deformation of a helical filament of length L under external forces and torques parallel to the helical axis. Hence the geometric curvature κ and torsion τ are constant along the filament. We use the Frenet frame as the material frame of the undeformed helix. Neglecting internal twists we use the strain vector $\boldsymbol{\Omega}=(0,\kappa,\tau)$ for the deformed state and write the free energy density

$$\mathfrak{f}=\frac{A}{2}\left[(\kappa-\kappa_0)^2+\Gamma(\tau-\tau_0)^2\right]. \tag{2.84}$$

We choose the orientation of the helical axis along the z axis of a cylindrical coordinate system (ρ,φ,z). The geometry and free energy of the uniformly deformed helix are completely described by its height $z=L\sin\alpha=L\frac{\tau}{\sqrt{\kappa^2+\tau^2}}$ and the difference in azimuthal angles of both ends of the filament. Note that $\varphi=\varphi(s=L)=Lk=L\sqrt{\kappa^2+\tau^2}$ holds, where we set $\varphi(s=0)=0$. Consequently we obtain the energy

$$\frac{\mathcal{F}(\varphi,z)}{AL}=\frac{1}{2}\left[\left(\frac{\varphi}{L}\sqrt{1-\left(\frac{z}{L}\right)^2}-\kappa_0\right)^2+\Gamma\left(\frac{\varphi}{L}\frac{z}{L}-\tau_0\right)^2\right]. \tag{2.85}$$

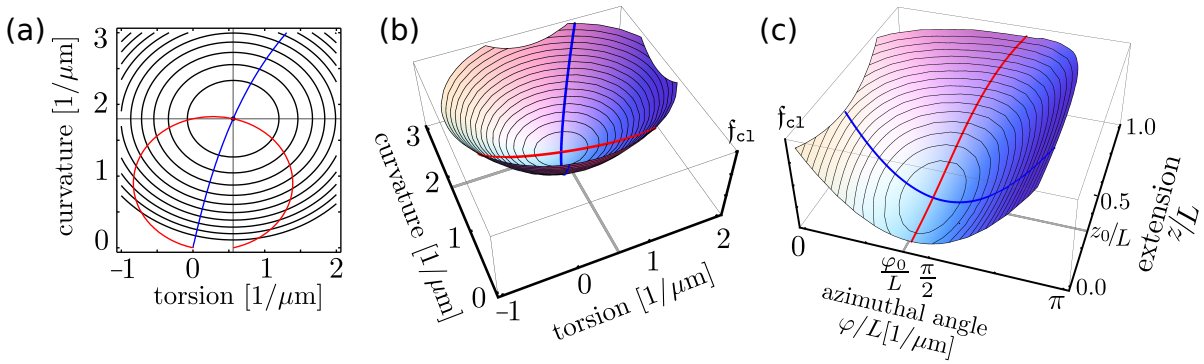

Abbildung 2.11: **(a)** and **(b)** The elastic energy for a uniform deformed helix as a function of curvature and torsion. Figure **(b)** shows the three dimensional energy surface, whereas **(a)** shows only the equipotential lines. Figure **(c)** explains the energy surface as function of the extension and the azimuthal angle. In all figures the **red** curve indicates the deformation of a pure force and the **blue** one the deformation of a pure torque.

For the calculation it is useful to replace the extension z/L by the pitch angle α using the identities $z/L = \sin\alpha$ and $\sqrt{1-(z/L)^2} = \cos\alpha$.

The force F and torque M acting on a uniformly stretched helix follow from the derivative of the elastic energy with respect to z and, respectively, φ. Therefore we use the chain rule $\partial_z \mathcal{F} = (\partial_\alpha \mathcal{F})/(L\cos\alpha)$ and conclude

$$\frac{F}{A} = -\frac{\kappa_0 - \frac{\varphi}{L}\cos\alpha}{\cos\alpha}\frac{\varphi}{L}\sin\alpha + \Gamma\left(\tau_0 - \frac{\varphi}{L}\sin\alpha\right)\frac{\varphi}{L}, \tag{2.86a}$$

$$\frac{M}{A} = \left(\kappa_0 - \frac{\varphi}{L}\cos\alpha\right)\cos\alpha + \Gamma\left(\tau_0 - \frac{\varphi}{L}\sin\alpha\right)\sin\alpha. \tag{2.86b}$$

Note that for an extension $z \to L$ ($\alpha \to \pi/2$) the force diverges which is due to the assumed incompressibility of the filament. In general there is always a small coupling of the extension and the twist. Only for the special case of $\Gamma = 1$ the equations (2.86a) and (2.86b) are uncoupled. In figure 2.11 we show the elastic energy $\mathfrak{f} = \mathcal{F}/L$ of the coiled form of a bacterial flagellum as a function of the curvature and torsion, and as function of the extension z/L and the azimuthal angle φ/L. The deformation due to a pure force is shown in red and due to a pure torque in blue. These deformations are often good approximations for the deformation of the helical filament in the simulations, also for non-uniformly deformed filaments. But we also have to note that the uniform deformation is not always a stable configuration, e. g. if the helix is compressed it starts to buckle [15, 21, 41–43, 46, 47].

Often we are only interested in small deviations from the relaxed configuration (z_0, φ_0).

So we linearize the equations (2.86) and obtain

$$\frac{F}{A} = -\left(1 + \frac{\tau_0^2}{\kappa_0^2}\right)(\Gamma\kappa_0^2 + \tau_0^2)\frac{z - z_0}{L} + (1-\Gamma)\tau_0\frac{\varphi - \varphi_0}{L}, \tag{2.87a}$$

$$\frac{M}{A} = (1-\Gamma)\tau_0\frac{z - z_0}{L} - \frac{\kappa_0^2 + \Gamma\tau_0^2}{\kappa_0^2 + \tau_0^2}\frac{\varphi - \varphi_0}{L}. \tag{2.87b}$$

These linear relations are the same as the ones, which are described by Love [84]. He derived them from the force and torque balance equations (2.43) without local forces $\boldsymbol{f} = 0$ and torques $\boldsymbol{m} = 0$.

Next we derive the stretch modulus and the effective torsional rigidity of a helix for a pure applied force F, or respectively, a torque M

$$F = -k\frac{z - z_0}{L} \qquad \text{for } M = 0 \tag{2.88a}$$

$$\text{with} \qquad k = \frac{A\Gamma(\kappa_0^2 + \tau_0^2)^3}{\kappa_0^2(\kappa_0^2 + \Gamma\tau_0^2)} = \frac{A}{R_0^2}\frac{\Gamma}{\cos^2\alpha_0 + \Gamma\sin^2\alpha_0}, \tag{2.88b}$$

$$M = -c\frac{\varphi - \varphi_0}{L} \qquad \text{for } F = 0 \tag{2.88c}$$

$$\text{with} \qquad c = \frac{A\Gamma(\kappa_0^2 + \tau_0^2)}{\Gamma\kappa_0^2 + \tau_0^2} = \frac{A\Gamma}{\sin^2\alpha_0 + \Gamma\cos^2\alpha_0}. \tag{2.88d}$$

Note that the spring constant $K_{\texttt{helix}}$ of the helical spring is given by the stretch modulus divided by the arc length $K_{\texttt{helix}} = k/L$. For the effective torsional rigidity we relate the change of the angle φ to the height of the helix $L_0 = \sin\alpha_0 L$ instead of the arc length L. Hence it is given by $C_{\texttt{eff}} = \sin\alpha_0 c$.

For a twist-bend ratio $\Gamma = 1$ there is no dependence of the constants k or c on the pitch of the helices. In the technical important case of a helical spring with a small pitch compared to the radius we find for the pitch angle $\sin^2\alpha_0 \approx 0$. In this case the spring constant is determined by the torsional rigidity C of the filament, whereas the torsional rigidity of the spring c is determined by the filament bending rigidity A.

Finally we make a short remark on the necessary conditions for the validity of the uniform deformation. As mentioned above one can also derive the relations for the force and the torque starting from the force and torque balance equations (2.43). There the assumption of a vanishing twist angle ϕ is equivalent to the condition that there is no torque in the normal direction $\boldsymbol{e}_1$. To receive a uniform helix at its ends one has to apply an additional torque $\boldsymbol{M} = \boldsymbol{e}_\varphi(C(\tau_0 - \tau)\kappa - A(\kappa_0 - \kappa)\tau)/\sqrt{\kappa^2 + \tau^2}$. Without this torque inhomogeneities at both ends occur, which lead to small deviations from the derived formulas.

Force extension curve of a helical filament

Now we investigate the case where the ends of the filament can rotate freely during stretching, i. e. the ends are torque free. This case is important in chapter 4.

We use the zero torque condition in equation (2.86b) to determine the relation between the twist and the extension

$$\frac{\varphi}{L} = \frac{\kappa_0 \cos\alpha + \Gamma\tau_0 \sin\alpha}{(\cos^2\alpha + \Gamma \sin^2\alpha)}. \tag{2.89}$$

Here we use again the pitch angle α as a short form for the extension $z/L = \sin\alpha$. Then, we derive the classical force-extension relation (see e. g. [125])

$$F(z) = \frac{A\Gamma(\kappa_0 \cos\alpha + \Gamma\tau_0 \sin\alpha)(\tau_0 \cos\alpha - \kappa_0 \sin\alpha)}{\cos\alpha(\cos^2\alpha + \Gamma \sin^2\alpha)^2}. \tag{2.90}$$

When we linearize this equation for a small relative extension $(z - z_0)/L$ we obtain the spring constant (2.88b) again.

Interestingly we find that the curvature $\kappa(z/L) = \sqrt{1-(z/L)^2}\frac{\varphi}{L}$ and the torsion $\tau(z/L) = \frac{z}{L}\frac{\varphi}{L}$ of a helix with extension z/L lie on the ellipse

$$[\kappa(z/L) - \kappa_0/2]^2 + \Gamma[\tau(z/L) - \tau_0/2]^2 = (\kappa_0/2)^2 + \Gamma(\tau_0/2)^2, \tag{2.91}$$

where the center is at $(\kappa_0/2, \tau_0/2)$. In deriving Eq. (2.91) we used expression (2.89) for φ/L. For a symmetric elastic energy with twist-to-bend ratio $\Gamma = 1$ the ellipse becomes a circle.

Bacterial flagella only have a length of a few pitches. So finite size effects from both ends lead to a noticeable dependence of curvature and torsion on arc length s. Nevertheless we find that Eq. (2.90) is a good approximation for the force-extension curve. This is even valid in the presence of thermal fluctuations, if the persistence length A/k_BT is not too small [125].

2.5.3 Effective bending rigidity of a helix

In the previous section we derived the stretch modulus and the torsional rigidity of a helical spring. Now we study the third typical elastic constant: an effective bending rigidity $A_{\mathtt{eff}}$. We will use it to analyze the buckling of a rotating flagellum in chapter 3. We note, in engineering science the understanding of buckling of helical springs is a well known problem. If the height of the spring is larger than its radius, one approximates the spring by a soft rod with effective bending, shear, and compressional rigidity [15, 46, 47]. In our case, contrary to classical helical spring theory, the pitch of the helix is much larger than its radius. We therefore have to generalize the theory of helical springs in Ref. [15] to derive an effective bending rigidity for the helical filament.

Our strategy is to apply a small constant torque perpendicular to the helical axis, rewrite the total elastic energy as a function of the torque and compare this result with the case of a simple rod to obtain $A_{\mathtt{eff}}$. To bend a simple rod with a constant

curvature Ω one needs the bending energy $\mathcal{F} = \frac{1}{2} A_{\mathtt{eff}} \Omega^2 L_0$. Using the torque $M = A_{\mathtt{eff}} \Omega$ (see Eq. (2.44)), we obtain

$$\mathcal{F} = \frac{1}{2} \frac{M^2}{A_{\mathtt{eff}}} L_0. \tag{2.92}$$

Now we calculate the corresponding elastic energy for the helical filament. We apply a constant torque $\boldsymbol{M} = M \boldsymbol{e}_x$ perpendicular to the helical axis $\boldsymbol{e}_z$ and replace the components of the angular strain vector $\boldsymbol{\Omega}$ in Kirchhoff's energy density (2.46) by the components of the torque $\boldsymbol{M} = A\Omega_1 \boldsymbol{e}_1 + A(\Omega_2 - \kappa)\boldsymbol{e}_2 + C(\Omega_3 - \tau)\boldsymbol{e}_3$ and we derive

$$\mathfrak{f}_{\mathtt{cl}} = \frac{1}{2} \left(\frac{M_1^2}{A} + \frac{M_2^2}{A} + \frac{M_3^2}{C} \right). \tag{2.93}$$

We note, the components of the applied torque $M_i = M \boldsymbol{e}_x \cdot \boldsymbol{e}_i$ depend on the local material frame $\{\boldsymbol{e}_1, \boldsymbol{e}_2, \boldsymbol{e}_3\}$ of the slightly deformed helical filament. We calculate the components M_i in leading order in M. Therefore we use the Frenet frame of the undeformed helix (2.82) as lowest order approximation of the material frame of the disturbed filament. Then we integrate equation (2.93) along the filament and obtain

$$\mathcal{F} = \frac{M^2 L}{4} \left[\frac{1}{A} + \frac{\sin^2 \alpha}{A} + \frac{\cos^2 \alpha}{C} + O\left(\frac{\sin 2kL}{2kL} \right) \right], \tag{2.94}$$

We compare this result with Eq. (2.92) and introduce the helix height $L_0 = L \sin \alpha$ in order to identify the effective bending rigidity

$$A_{\mathtt{eff}} = A \frac{2 \sin \alpha}{\left(1 + \sin^2 \alpha + \frac{A}{C} \cos^2 \alpha\right)}. \tag{2.95}$$

In engineering science the effective bending rigidity of helical springs with a small pitch compared to the radius is used. To compare this with our result we derive a first order expansion of $A_{\mathtt{eff}}$ in α. We introduce the number of coils $n = Lk/(2\pi)$ with the length of one coil $2\pi/k$. Furthermore we use the helical radius $R \approx 1/k + O(\alpha^2)$ and the height of the helix $L_0 \approx L\alpha$. Finally we conclude the result $\frac{1}{A_{\mathtt{spring}}} \approx \frac{n}{L_0} \frac{\pi R}{A} (1 + \frac{A}{C})$, which is given in [15].

2.5.4 Propagation of a disturbance

An instantaneously applied force at one end of the helical filament induces a localized deformation, which spreads along the helix. To treat this situation approximately we assume the helical filament to be an extensible rod, that locally obeys the linearized force-extension relation (2.88a) with $(z - z_0)/L$ replaced by $\mathrm{d}z/\mathrm{d}s$. In addition the rod possesses the local friction coefficient per unit length $a_{\parallel} = A_{\parallel}/L$ (see Eq. (2.19)) for

moving a helix parallel to its axis. Balancing elastic and viscous forces locally, results in the diffusion equation

$$\partial_t z = \frac{k}{a_\parallel} \partial_s^2 z, \tag{2.96}$$

where k is the spring constant of the helix given in Eq. (2.88b). A localized deformation at one end of the helical filament spreads diffusively over the whole filament on a time scale $\tau_C = a_\parallel L^2/k$. For a normal flagellum with length $L = 10\mu\text{m}$ and a helical radius of $R = 0.2\mu\text{m}$ we obtain a typical time of a millisecond.

Analogically we also obtain a diffusion equation for the twist by balancing the elastic torque with the effective rotational friction of the helix

$$\partial_t \Delta\varphi = \frac{c}{b_\parallel} \partial_s^2 \Delta\varphi, \tag{2.97}$$

with the rotational friction coefficient per arc length $b_\parallel = B_\parallel/L$ (see Eq. (2.19)) and the torsional spring constant (2.88d). This equation also occurs in the twist dynamics of a rotating straight rod [132]. The corresponding time scale $\tau_C = b_\parallel L^2/c$ is similar to the one discussed before.

Kapitel 3

Motor-driven bacterial flagella and buckling instabilities

3.1 Introduction

In this chapter we concentrate on the normal form of a single bacterial flagellum of *E.coli*. We neglect the different polymorphic states and only investigate the complex interplay of elasticity and frictional forces. Most results of this chapter are published in [B].

In section 3.2 we model the motor driven flagellum using the free elastic energy of Kirchhoff's rod theory as introduced in section 2.3.2. The coupling of the motor torque to the helical filament by the hook is described by our coarse-grained approach of section 2.1.2. We perform the simulations with the numerical scheme described in section 2.4. The motor torque enters the simulation as an external torque in equation (2.79) and we assume in this chapter that its orientation is fixed, i. e. $\boldsymbol{M} = M\boldsymbol{e}_z$.

A rotating helical flagellum produces a thrust force that adds up along the filament and then pushes the cell body forward. We report two buckling instabilities of a fixed helical filament for increasing motor torque. The first instability occurs in the biologically relevant regime. The straight helical filament starts to bend under the influence of the acting thrust force similar to a rod that buckles under its own load. The buckling instability is visible as a supercritical Hopf bifurcation in the thrust force. It also occurs when the filament is allowed to move by attaching it to a load particle. In this section we mostly perform deterministic simulations, only in a few cases of the fixed filament we have added thermal fluctuations to study their influence. Most of the time we use $\Gamma = 1$ for the twist-to-bend ratio, but also show that our results are comparable to other values if they are rescaled by the effective bending rigidity of the helical filament.

In section 3.3 we will develop an analytical model, which explains the buckling transition and reproduces quantitatively the critical force-torque relation from our simulations. To derive this model we replace the helical filament by a rod with its effective bending rigidity and a rotation-translation coupling in the resistance that catches the helicity of the flagellum. We note that the problem is more complex than the buckling instabilities reported in section 2.3.3 due to the characteristic rotation-translation coupling and the fact that we do not fix the orientation of the helical filament. Nevertheless we are able to obtain a quantitative agreement with the simulations in the biologically relevant regime.

3.2 The motor-driven helical filament

In this section we study in detail the thrust force that the motor-driven helical filament generates both when the actuated end of the filament is fixed in space or attached to a larger load particle, which mimics the cell body. In particular, we describe the buckling transitions by illustrating the observed filament configurations.

It is instructive to shortly remind to pure rotational motion of a rigid helix. In section 2.2.3 we described the formal analogy between the torque-driven rotation of a rigid helix at low Reynolds number and the motion of the force and torque less spinning top with axial symmetry in classical mechanics [7, 73]. According to this analogy, the rigid helix in a viscous fluids precesses about the constant applied torque while also rotating about its helical axis.

However, in our simulations we observe after introducing a finite elasticity of the helical filament, the precession is no longer stable and the helical filament aligns parallel or perpendicular to the torque that is coiling or uncoiling the helix, respectively. In general, the deformation of the filament driving its reorientation depends on the angle between the torque and the first tangent vector of the helical filament and oscillates due to the rotation. At least there is one configuration where the rotation does not change the deformation. This is the case where the helical axis is parallel to the torque. We will discuss this aligned state now in more detail.

3.2.1 Force-torque relation and buckling

Discussion of the basic features

In this section we investigate the motor-driven helical filament and its created thrust force if we fix its first position $\boldsymbol{r}(0) = \boldsymbol{r}^{(0)}$ where the torque is applied. The rotating filament creates a thrust force that is given by the force component on the first bead parallel to the applied torque $\boldsymbol{M} = M\boldsymbol{e}_z$: $F = -\partial\mathcal{F}/\partial\boldsymbol{r}^{(0)} \cdot \boldsymbol{e}_z$ in the discretized model. Figure 3.1(a) plots the resulting thrust force F versus the applied torque determined in simulations without thermal noise. We discuss the graph in detail.

A positive torque M produces a thrust force that pushes against the anchoring point of the filament. The thrust force is constant in time as indicated by the straight line (ii) in figure 3.1(b). The illustration (ii) of figure 3.1(c) shows the stable orientation of the helical filament along the torque $\boldsymbol{M}$. It rotates about the helical axis with angular frequency ω. The local thrust force acting along the helix axis is indicated by F^l. The tangent of the filament at the anchoring point is tilted against $\boldsymbol{M}$ and the tip moves on a circle, as indicated by the schematic.

A negative torque M generates a negative force that pulls at the anchoring point. However, we realized that the orientation of the filament along the torque is not stable. For long times the filament turns away from the torque axis [green arrow in illustration (i) of figure 3.1(c)] until it reaches a configuration perpendicular to $\boldsymbol{M}$, where it slowly

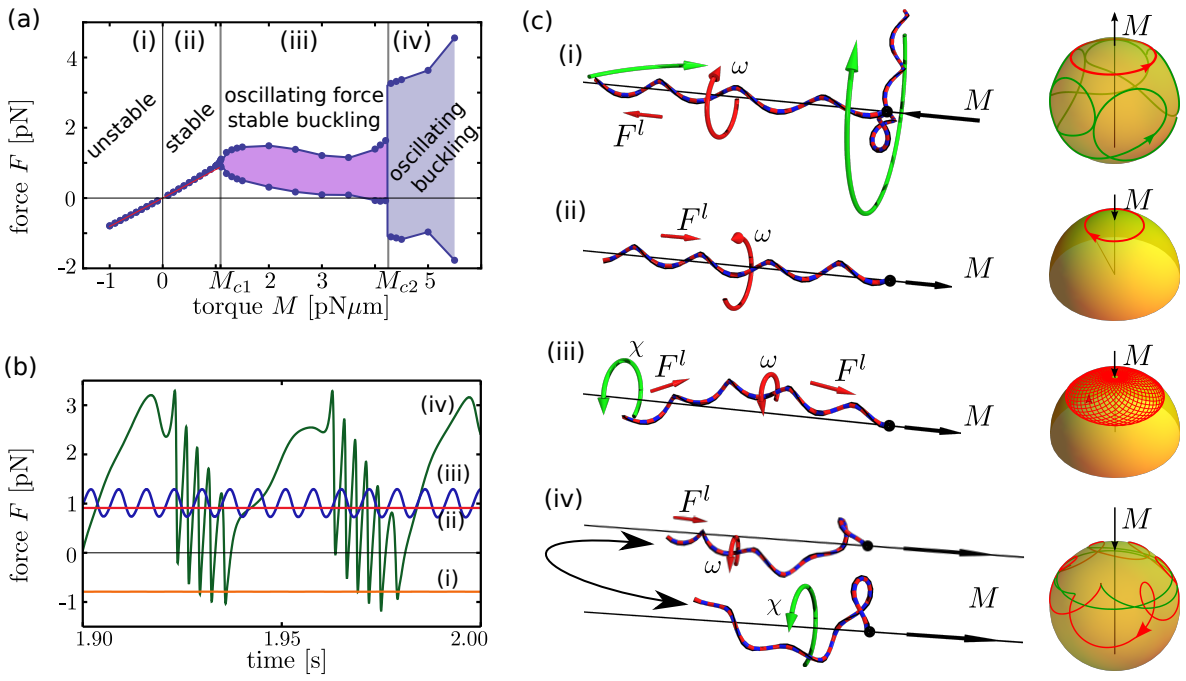

Abbildung 3.1: **(a)** Thrust force F versus motor torque M. Four different regimes associated with different configurations of the rotating filament exist. In regime (iii) and (iv) the minimum and maximum value of the oscillating thrust force are shown. A supercritical bifurcation occurs at the critical torque $M_{c1} \approx 1.1\text{pN}\mu\text{m}$ indicating a buckling transition. A second bifurcation is visible at $M_{c2} \approx 4.2\text{pN}\mu\text{m}$. The red line in regimes (i) and (ii) follows from resistive force theory. **(b)** Thrust force versus time for specific torque values in the four different regimes: (i) $M = -1.0\text{pN}\mu\text{m}$, (ii) $M = 1.0\text{pN}\mu\text{m}$, (iii) $M = 1.2\text{pN}\mu\text{m}$, and (iv) $M = 4.5\text{pN}\mu\text{m}$. **(c)** Characteristic snapshots of the helical filament in the four regimes. The red circular arrow and ω indicate a rotation about the local helix axis and F^l the local thrust force. The green circular arrow and χ show the precession about the external torque axis. In addition, the trajectory of the tip of the first tangent vector is indicated: (i) The green line belongs to the perpendicular orientation of the filament, (iv) red line: fast rotation about helical axis, green line: slow precession about motor torque during relaxation of the filament.

rotates about the local helical axis and slowly precesses about $\boldsymbol{M}$. This motion is also visible for the tip of the first tangent vector. The reorientation of the helix occurs due to elastic deformations when the negative torque slightly unwinds the helical filament. The linear increase of F with M in the regimes (i) and (ii) in figure 3.1(a) fits well with the result from resistive force theory for a perfect helical filament, as indicated by the line. Small deviations are visible at higher torques due to elastic deformations of the helix which enhance the thrust force.

At a critical torque $M_{c1} \approx 1.1\text{pN}\mu\text{m}$ the thrust force starts to oscillate as curve (iii) in figure 3.1(b) indicates. Minimum and maximum values of the force are plotted in figure 3.1(a). They develop continuously from the constant force at M_{c1} indicating a supercritical Hopf bifurcation. Illustration (iii) of figure 3.1(c) shows a buckled configuration that rotates about the local helix axis with frequency ω and precesses with frequency χ about the motor torque $\boldsymbol{M}$ keeping its shape fixed. The trajectory of the tip of the first tangent vector reflects this motion. A straightforward explanation is that the helical filament buckles under the thrust force generated by the rotating filament. The force adds up from the free to the fixed end of the filament and puts the filament under compressional tension. This is similar to a rod that buckles under its own gravitational load [74, 84] . In section 3.3 we will develop a theory for this buckling transition which is quite involved. Finally, at a critical torque value of $M_{c2} \approx 4.2\text{pN}\mu\text{m}$ a second bifurcation occurs in the force-torque relation of figure 3.1(a). The buckled state itself becomes unstable, visible by the fast oscillations of the thrust force in figure 3.1(b). The buckled configuration is compressed until the fixed end becomes perpendicular to the motor torque. At this point the fast rotation about the local helical axis stops and the thrust force averaged over one fast period is approximately zero. Now the strongly bent configuration of the filament relaxes slowly and precesses about the applied torque $\boldsymbol{M}$ as shown in the second configuration in figure 3.1(c)(iv). The thrust force on the anchoring point slowly increases. When the filament is sufficiently relaxed, it starts again its fast rotations about the local helix axis and the whole cycle repeats. The trajectory of the tip of the first tangent for a full cycle is also shown in figure 3.1(c)(iv). The red curve corresponds to the fast rotation and the green one to the relaxation. We note, in the torque-force diagram this second bifurcation leads to a jump of the maximal and minimal force. But we do not observe a hysteresis if we change the torque from values larger than the critical torque to smaller ones.

Movies for all four types of configurations are available in the supplemental material of [B].

Discussion of additional features

The reported supercritical Hopf bifurcation is also visible in other quantities besides the thrust force. We discuss here additional properties of the motor-driven helical filament.

To quantify the stability of the filament aligned parallel to the motor torque axis, we recorded the temporal evolution of the elastic free energy starting from a small

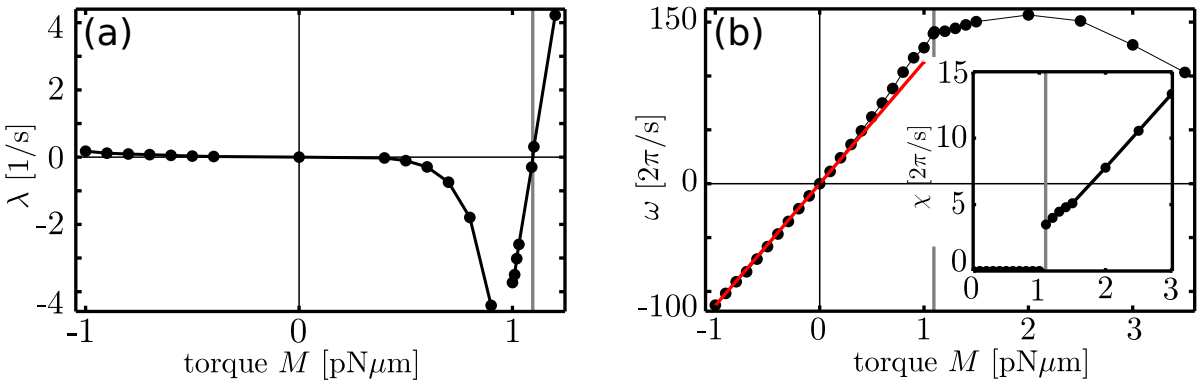

Abbildung 3.2: **(a)** Relaxation rate λ of the elastic free energy versus applied torque M for a small disturbance of the aligned state where the filament is parallel to the torque direction. **(b)** Angular velocity ω and precession frequency χ versus torque M. The supercritical bifurcation at M_{c1} is clearly visible. The red line is calculated with resistive force theory.

disturbance of the aligned state and fit it to the form

$$|\mathcal{F} - \mathcal{F}^0| \approx \delta\mathcal{F}^0 \exp(\lambda t) \sin(\omega t). \tag{3.1}$$

Here ω is the angular velocity of the rotating helix leading to oscillations in $\mathcal{F}$ and λ is the reorientation rate. The result for λ is plotted in figure 3.2(a). For positive M below the critical torque, the negative λ indicates the stable aligned state. For small M a reorientation of the filament could not be detected within the simulation time. Since frictional forces are small and hardly deform the helix, it just precesses about the applied torque. Nevertheless, to record the force-torque relation, we always started from an aligned state at $M = 1\text{pN}\mu\text{m}$ and then changed the driving torque to the desired value and let the elastic free energy relax to its stationary value, where we finally recorded the thrust force. The small positive λ for $M < 0$ indicates the slow reorientation of the filament towards the perpendicular configuration. The supercritical Hopf bifurcation is located where λ changes its sign from negative to positive.

Figure 3.2(b) shows the angular frequency ω for rotations about the local helix axis as a function of M. The linear regime belongs to the aligned state, deviations from it occur in the buckled state. The precession frequency χ for rotations of the whole filament about the torque axis is plotted in the inset. A non-zero χ corresponds to the buckled state.

Finally, we investigate the mean end-to-end distance $\langle r \rangle$ of the helix and its standard

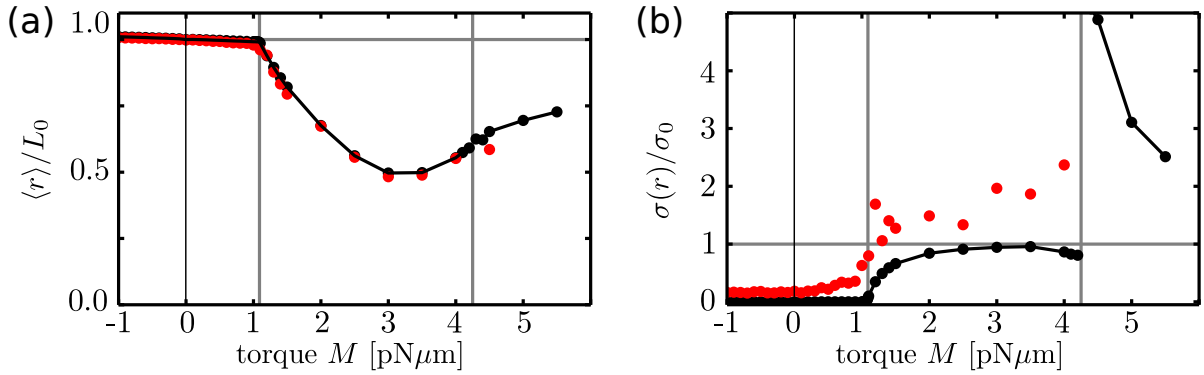

Abbildung 3.3: **(a)** Mean end-to-end distance $\langle r \rangle$ in units of the helix length L_0 versus M. The red dots are results from Brownian dynamics simulations with thermal noise included. **(b)** Standard deviation $\sigma(r)$ of the end-to-end distance in units of $\sigma_0 = R/\sqrt{2}$ versus M. Thermal noise (red dots) leads to fluctuations about the mean value.

deviation σ as a function of M, respectively. They are defined as

$$\langle r \rangle = \lim_{T\to\infty} \frac{1}{T} \int_0^T |\boldsymbol{r}(s = L) - \boldsymbol{r}(s = 0)| \mathrm{d}t, \tag{3.2}$$

$$\sigma^2 = \left\langle (r - \langle r \rangle)^2 \right\rangle . \tag{3.3}$$

In the aligned state the end-to-end distance is constant and given by the height L_0 of the helix. We observe for a torque of $M = \pm 1\mathrm{pN\mu m}$ a small stretching or compression, respectively, of less than 1% due to the rotational induced force. This is consistent with the spring constant $A/(R^2 L)$ we derived in section 2.5.2. After the first bifurcation $\langle r \rangle$ shrinks rapidly due to the bending of the filament. We show the results in figure 3.3(a) in black.

Whereas $\langle r \rangle$ is continuous at both bifurcations, the standard deviation displays a pronounced discontinuity at the second bifurcation in agreement with the behavior of the thrust force as shown in figure 3.3(b). We write σ in units of $\sigma_0 = R/\sqrt{2}$, where R is the helix radius. σ_0 is the maximum value of σ in regime (iii) where the buckled helix has a constant shape but the free end of the filament rotates on a circle with radius R. This maximum is reached in our simulations if the filament is bent to half of its equilibrium length. We note, that the variance σ_0 is small compared to the height L_0 of the helix: $\sigma_0/L_0 \approx 1.7\%$. The strong increase of σ in regime (iv) is due to the oscillating buckled state.

The rotating filament also experiences thermal forces due to the viscous environment. However, since the persistence length $A/k_B T \approx 1\mathrm{mm}$ calculated from the bending rigidity A is much larger than the filament length of $10\mu\mathrm{m}$, we do expect that our results are

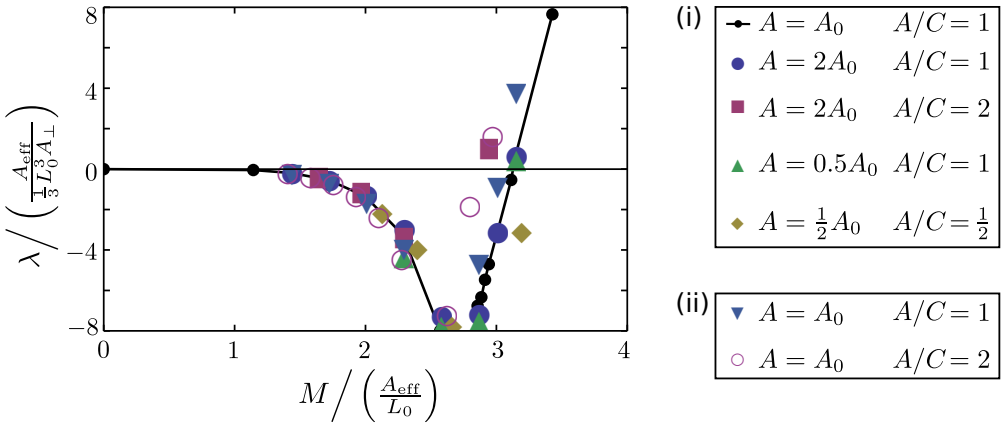

Abbildung 3.4: Reorientation rate λ as a function of motor torque M for different elastic constants, where $A_0 = 3.5\text{pN}\mu\text{m}^2$ is the bending rigidity usually used in this work. Two helical geometries of the flagellum are considered: (i) for peritrichous bacteria (e. g. *E.coli*) and (ii) for monotrichous bacteria.

robust against thermal fluctuations. This is confirmed by the end-to-end distance $\langle r \rangle$ in figure 3.3(a) (red dots) which agrees with the deterministic simulations. The standard deviation in figure 3.3(b) indicates some fluctuations. Below the buckling transition we can directly connect them to compressional fluctuations using the spring constant of the helical filament, that we calculated in Eq. (2.88b) of chapter 2. For a twist-to-bend ratio of $\Gamma = 1$ it is given by $K = A/(R^2 L)$. The equipartition theorem states that the mean energy due to the compression of the helical spring is equal to the thermal energy

$$\left\langle \frac{1}{2} K (r - L_0)^2 \right\rangle = \frac{1}{2} k_B T. \tag{3.4}$$

Dividing this equation by σ_0^2 we obtain $\sigma/\sigma_0 \approx 0.15$ which is in good agreement with the simulated value of 0.18. In the buckled state, the helical filament has more opportunities to fluctuate around which explains the further increase of σ.

Furthermore, we observe strong fluctuations of the thrust force in our Brownian simulations. An average over these fluctuations agrees with the deterministic case (data not shown). The fluctuations would also be smoothed out in an experiment which performs some temporal average during measurement.

Alignment and buckling depend on the effective bending rigidity

We claim that the reorientation rate depends on the bending of the helical filament as a whole and thus the effective bending rigidity A_{eff} should be the relevant parameter. We therefore study in detail the reorientation rate λ of the fixed flagellum which was introduced in equation (3.1).

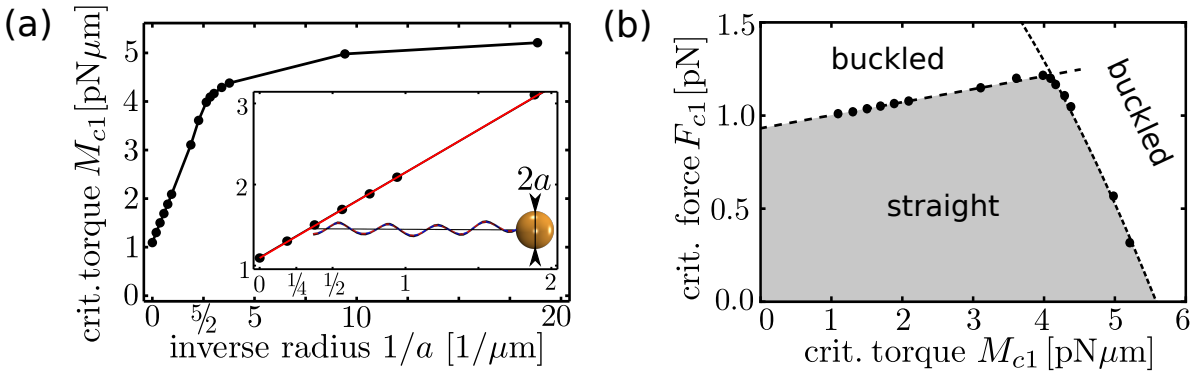

Abbildung 3.5: Buckling transition for a helical filament attached to a bead of radius a that can move along the z direction. **(a)** Critical torque M_{c1} as a function of inverse bead radius $1/a$. Inset: Blow-up for the biologically relevant regime. **(b)** Critical force F_{c1} versus critical torque M_{c1}.

We determined λ as a function of the motor torque M for different values of the bending rigidity A and the torsional rigidity C. In addition to the helical geometry of peritrichous bacteria, like *E.coli*, used in this work, we also consider the flagellum of monotrichous bacteria, which has different helical parameters: $\kappa_0 = 2.2/\mu\text{m}$ and $\tau_0 = 2.5/\mu\text{m}$ [38].

In analogy to the theory of buckling of rods in section 2.3.3 we rescale the torque M by the characteristic bending moment A_{eff}/L_0. Dimensional analysis suggests to rescale the reorientation rate λ by $A_{\text{eff}}/(\frac{1}{3}L_0^3 A_\perp)$, where $A_\perp$ is the friction coefficient of the helix perpendicular to the helical axis as introduced in Eq. (2.19a). The factor $\frac{1}{3}L_0^2 A_\perp$ corresponds to the rotational friction of a helix about an axis perpendicular to the helical one. Using this rescaling all different curves for the reorientation rate fall onto a common master curve as shown in figure 3.4. The effective bending rigidity A_{eff} is therefore the right parameter in an effective description of the helical filament.

3.2.2 Buckling instability during locomotion

So far we have studied the situation where one end of the filament is fixed in space so that it cannot translate. However, rotating flagella push the cell body of a bacterium forward so that it moves. We mimic this scenario by attaching the filament to a bead of radius a which, for simplicity, can only move along the z direction. The thrust force F generated at the attached end of the filament is then used to push the sphere forward acting against the Stokes friction force. We observe similar thrust force-torque relations as for the case of a fixed filament. The aligned state is again unstable for negative torque and possesses a larger reorientation rate which might have biological relevance as we discuss in section 3.4. For positive torque, the aligned state is stable and the thrust force

grows linearly in the driving torque M until the Hopf bifurcation occurs at a critical value M_{c1} indicating the buckling instability.

Figure 3.5(a) shows the critical torque M_{c1} as a function of the inverse bead radius $1/a$. From $1/a = 0$, which corresponds to the fixed filament, the critical torque increases linearly in $1/a$ and then at $a^{-1} \approx 5/2$ turns into a slow growth towards the value for the freely swimming helix, i. e., $1/a \to \infty$. In the biological relevant case with the cell body size $a \approx 0.5 \cdots 2\mu\text{m}$, the linear dependence of the critical torque on $1/a$ can be derived based on the fact that the critical thrust force F_{c1} is nearly constant, as we show in figure 3.5(b). Hence the velocity $v = F_{c1}/(6\pi\eta a)$ is so slow that the buckling transition is hardly influenced by the motion of the helical filament with the attached bead. Now, force and torque on the helix depend linearly on velocity v and angular velocity ω as described by Eq. (2.20). Eliminating ω and setting $v = F_{c1}/(6\pi\eta a)$ at the buckling transition, one arrives at

$$M_{c1} = -\frac{B_\parallel}{C_\parallel} F_{c1} + \left(C_\parallel - \frac{A_\parallel B_\parallel}{C_\parallel} \right) \frac{F_{c1}}{6\pi\eta} \frac{1}{a}. \tag{3.5}$$

Here $A_\parallel$, $B_\parallel$, and $C_\parallel$ are the translational, the rotational, and coupling friction coefficients parallel to the helical axis, respectively, as given in the Eqs. (2.19). This formula with the coefficients calculated by resistive force theory reproduces the linear increase for small $1/a$, as demonstrated by the red line in the inset of figure 3.5(a).

In figure 3.5(b) we plot the critical thrust force versus the critical torque. For biologically relevant values M_{c1} between 1 and 2pNμm the critical force is indeed nearly constant. It only shows a very slow linear increase since frictional forces due to the motion of the helix stabilize it against buckling. At $M_{c1} \approx 4\text{pN}\mu\text{m}$ the behavior changes dramatically. The critical thrust force goes to zero proportional to M_{c1}^2 (see dotted line) following the behavior of a rod that buckles under an applied force and torque as described in section 2.3.3. In this regime the supercritical Hopf bifurcation becomes subcritical and hysteresis occurs. Hence, whereas for small torques a buckling is hindered by locomotion, we observe for large torque the typical quadratic dependence $F_{c1} \propto M_{c1}^2$, which we described for the buckling of a rod subjected twist and thrust on its ends in section 2.3.3. In the following section, we develop a theory to describe the observed buckling transition.

3.2.3 Twist dependent friction

In section 3.2.1 we described the force torque dependence by a linear relation due to resistive force theory for a perfect helical filament apart small deviations at torques of 1pNμm. For the moving filament attached to a bead the deviations become more pronounced. In this section we discuss in more detail the responsible elastic deformations of the helical filament below the critical torque of the first bifurcation.

We have seen that the relative compression due to the force is small. Using the effective spring constant $A/(R^2 L)$ (2.88b) for the helical filament with the maximal obtained

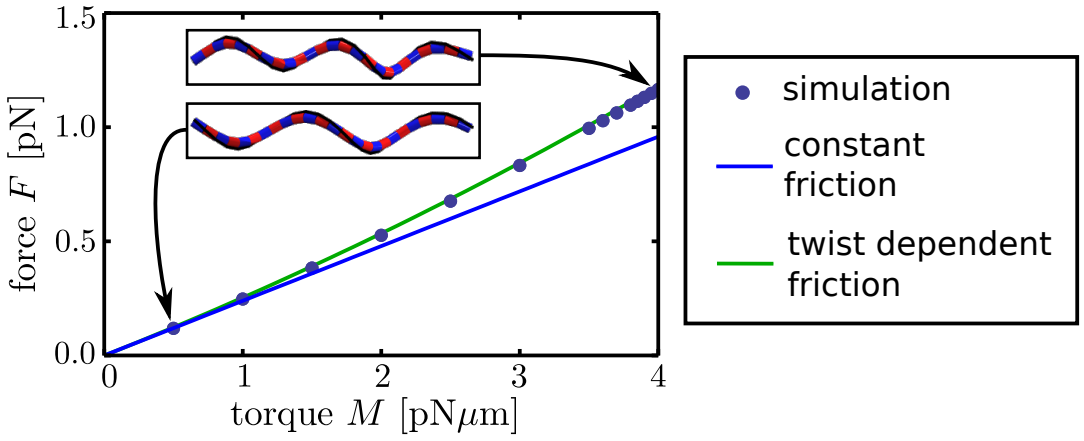

Abbildung 3.6: Thrust force F versus motor torque M below the bifurcation point for a helical filament attached to a bead of radius $a = 0.35\mu$m. The inlets show the first part of the helical filament. For large torque the number of helical turns is increased.

critical force at the buckling transition, we see that the compression remains below 2%, which is negligible. Therefore the pitch angle α_0 remains constant.

On the other hand, we apply a torque along the helical axis. As a result, one end of the helix twists against the other end by an angle $\Delta\phi/L = \Delta k$, where k is the increase of the angle φ per unit length introduced in section 2.5.1. The change Δk is directly related to a different helical pitch and radius, where the latter enters in the friction coefficients (2.19).

Using Eq. (2.88d) with $\Gamma = 1$ we relate the twist to the applied motor torque. One end of the helical filament is free. Hence, the twist increases linearly from the free end to the end, where the torque is applied, and the average value is $\Delta\phi/L = \Delta k = M/(2A)$.

We use the identity $R = \cos\alpha/k$ given in table 2.2 to derive the inverse radius of the twisted filament as function of the applied torque

$$R^{-1} = R_0^{-1} + (\cos\alpha_0)^{-1} M/(2A). \tag{3.6}$$

Using this relation for the friction coefficients (2.19) we obtain a torque or twist dependent friction.

In figure 3.6 we compare the linear theory with constant friction coefficients and the theory with twist dependent friction with our simulations of a filament attached to a small bead of radius $a = 0.35\mu$m. For small torque the twist dependent theory agrees with the linear one and for large torque the new theory explains the deviations from the linear theory, which we observed in the simulations.

3.3 Buckling theory for a helical rod

The goal in this section is to formulate a theory that reproduces the force-torque relation in figure 3.5(b) for the first buckling transition of the helical filament as obtained by our simulations. Clearly, this relation cannot directly be explained by the theory of a thin elastic rod that buckles under the influence of an external force and torque which we described in section 2.3.3. There are several reasons for this. First, the helical filament is not just a simple elastic rod. Second, the external force that puts the helix under tension is generated locally by the rotation-translation coupling of the helix and accumulated along the filament similar to a rod that buckles under its own gravitational weight but in contrast to that, acts only parallel to the helical axis. Third, the whole filament moves with a constant velocity which leads to additional frictional forces and it also precesses about the external torque in the buckled state. In the following we formulate a model based on the theory of a thin elastic rod, derive from it a force torque relation for the buckling transition, and compare it to figure 3.5(b).

3.3.1 Model equations

To set up our model equations, we approximate the helical filament by a thin helical rod, where the helicity comes in through the rotation-translation coupling in the friction matrix. The length of the rod, $L_0 = \sin\alpha L$, agrees with the height of the helix, where α is the pitch angle. In engineering science the buckling of helical springs is a well known problem. If the height of the spring is larger than its radius, one approximates the spring by a soft rod with effective bending, shear, and compressional rigidity [15, 46, 47, 62]. In our case, in contrast to classical helical spring theory, the pitch of the helix is much larger than its radius. We therefore generalized the theory of helical springs and derived the effective bending rigidity $A_{\mathtt{eff}}$ of the helical rod in terms of the bending and torsional rigidity of the filament in section 2.5.3. In section 3.2.1 we demonstrated by rescaling simulation results for different helical geometries, bending, and torsional rigidities, that $A_{\mathtt{eff}}$ is the right parameter in an effective description of the helical filament.

To address buckling of the helical rod, we start with the balance equations for internal elastic force $\boldsymbol{F}$ and torque $\boldsymbol{M}$ acting on a elastic rod (see Eqs. (2.43))

$$\boldsymbol{F}' + \boldsymbol{f} = 0 \tag{3.7a}$$

$$\boldsymbol{M}' + \boldsymbol{e}_3 \times \boldsymbol{F} + \boldsymbol{m} = 0 \tag{3.7b}$$

Here $\boldsymbol{f}$ and $\boldsymbol{m}$ denote, respectively, external force and torque densities due to the applied motor torque and friction with the surrounding fluid.

In addition, boundary conditions are necessary. At the free end of the rod ($s = L_0$) no external force and torque act, so elastic force and torque have to vanish. The hinged end attached to the sphere can only move in z direction with velocity v. The external torque $M\boldsymbol{e}_z$ is balanced by the elastic torque $\boldsymbol{M}(0)$ and the thrust force on the sphere

$F = 6\pi\eta a v$ equals the elastic force at the leading end of the rod, $F_z(0)$:

$$F_z(0) = F = 6\pi\eta a v, \qquad \boldsymbol{M}(0) = M\boldsymbol{e}_z, \tag{3.8a}$$
$$\boldsymbol{F}(L_0) = \boldsymbol{0}, \qquad \boldsymbol{M}(L_0) = \boldsymbol{0}. \tag{3.8b}$$

After setting up the problem, we have to explain how the different forces and torques entering Eqs. (3.7) look like for the helical rod close to the buckling transition. The elastic torque $\boldsymbol{M}$ is given by the constitutive relation (2.44). Only the spontaneous curvature and torsion are zero for the rod which serves as an effective representation of the helical filament:

$$\boldsymbol{M} = A_{\mathtt{eff}}\Omega_1\boldsymbol{e}_1 + A_{\mathtt{eff}}\Omega_2\boldsymbol{e}_2 + C_{\mathtt{eff}}\Omega_3\boldsymbol{e}_3, \tag{3.9}$$

where $A_{\mathtt{eff}}$ is the effective bending rigidity of Eq. (2.95). Since buckling theory considers local displacements of the rod only, the torsional term and the actual value of the effective torsional rigidity C_{eff} are not important. In setting up linearized equations in the vicinity of the buckling transition, the elastic force $\boldsymbol{F}$ is only needed for the unbuckled straight rod oriented along $\boldsymbol{e}_z$. Since the external force density $\boldsymbol{f}$ is constant for the straight rod, as we argue in the next paragraph, Eq. (3.7a) and boundary conditions (3.8) give the linear force profile

$$\boldsymbol{F}(z) = f_\parallel(L_0 - z)\boldsymbol{e}_z \qquad \text{with } f_\parallel = F/L_0, \tag{3.10}$$

where we introduce $f_\parallel$ as thrust force F divided by the rod length L_0. In the following we will use this as a parameter.

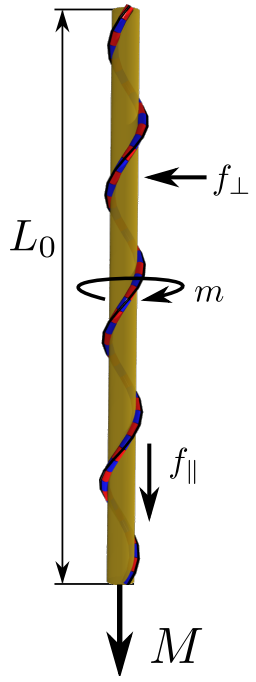

Abbildung 3.7: Effective description of the helical filament.

The straight filament moves with a constant velocity $v\boldsymbol{e}_z$ and rotates with a constant angular velocity $\omega\boldsymbol{e}_z$. They result, respectively, in a constant frictional force density $f_\parallel\boldsymbol{e}_z$ and a torque density $m\boldsymbol{e}_z$ with

$$f_\parallel = a_\parallel v + c_\parallel\omega, \tag{3.11a}$$
$$m = c_\parallel v + b_\parallel\omega, \tag{3.11b}$$

where the frictional coefficient $c_\parallel$ couples translation to rotation. For the local friction we assume the friction coefficients of a helix with full helical turn (2.19) divided by its height, i. e.

$$a_\parallel = A_\parallel/L_0, \qquad a_\perp = A_\perp/L_0, \qquad b_\parallel = B_\parallel/L_0, \quad \text{and} \qquad c_\parallel = C_\parallel/L_0. \tag{3.12}$$

Here we have also introduced the local friction coefficient $a_\perp$ perpendicular to the helical axis, which we will need below. In Eq. (3.10) we have already linked $f_\parallel$ to the thrust

force F. From the torque balance equation (3.7b) and the boundary conditions (3.8), we also deduce a linear torque profile

$$\boldsymbol{M}(z) = m(L_0 - z)\boldsymbol{e}_z \qquad \text{with } m = M/L_0, \tag{3.13}$$

where we relate m to the applied motor torque M divided by the rod length L_0. Hence, m is the second parameter in our problem.

The buckled rod after the first buckling transition in our simulations has a constant shape. It rotates about the local tangent vector with angular velocity $\omega\boldsymbol{e}_3$ and precesses with angular velocity χ about the axis of the applied torque leading to a local velocity $\chi\boldsymbol{e}_z \times \boldsymbol{r}$. Furthermore, the filament translates with velocity v along the z-direction and the total local velocity amounts to $\boldsymbol{v} = v\boldsymbol{e}_z + \chi\boldsymbol{e}_z \times \boldsymbol{r}$. In the vicinity of the buckling transition, deformations are small and in leading order we can identify v and ω with the values of the straight rod. Then, the frictional torque along the local tangent vector is

$$\boldsymbol{m} = m\boldsymbol{e}_3, \tag{3.14}$$

where m is already given in Eq. (3.11b). Thus, close to the buckling instability we can identify m with the applied motor torque as in Eq. (3.13). The frictional force density becomes

$$\boldsymbol{f} = f_\parallel \mathbf{P}_\parallel \cdot \boldsymbol{e}_z + f_\perp \mathbf{P}_\perp \cdot \boldsymbol{e}_z + a_\perp \chi \mathbf{P}_\perp \cdot (\boldsymbol{e}_z \times \boldsymbol{r}), \tag{3.15}$$

where we introduce the projectors

$$\mathbf{P}_\parallel = \boldsymbol{e}_3 \otimes \boldsymbol{e}_3 \qquad \text{and} \qquad \mathbf{P}_\perp = \mathbf{1} - \boldsymbol{e}_3 \otimes \boldsymbol{e}_3, \tag{3.16}$$

on the directions parallel and perpendicular to the tangent vector $\boldsymbol{e}_3$. The force density $f_\parallel$ has already been given in Eq. (3.11a) and

$$f_\perp = a_\perp v \tag{3.17}$$

characterizes the frictional force density generated perpendicular to the local rod axis when the rod moves with velocity v. Finally, $a_\perp\chi$ is the friction due to the precession of the rod. The friction coefficient $a_\perp = A_\perp/L_0$ is derived from the coefficient for a full helix (2.19a) as introduced before in Eq. (3.12). We note that a term $\mathbf{P}_\parallel \cdot (\boldsymbol{e}_z \times \boldsymbol{r})$ does not appear since it does not contribute in leading order to $f_\parallel$. We also did not include the rotation-translation coupling perpendicular to $\boldsymbol{e}_3$ since the two terms cancel each other in the equations, we formulate in the following.

We will analyze the buckling transition by first considering the four parameters m, $f_\parallel$, $f_\perp$, and χ as independent and then apply our results to reproduce the force-torque relation of the helical rod. Buckling occurs when the straight solution $\boldsymbol{r}(z) = (0, 0, z)$ of Eqs. (3.7a) becomes unstable and a new non-trivial solution occurs at a certain parameter set. We, therefore, use the ansatz $\boldsymbol{r}(z) = (X(z), Y(z), z)$ and seek two equations linear in X,

Y, and its derivatives. We start by taking the derivative of the torque balance equation (3.7b) and use $\boldsymbol{F}' = -\boldsymbol{f}$ to arrive at

$$\boldsymbol{M}'' + \boldsymbol{e}_3' \times \boldsymbol{F} - \boldsymbol{e}_3 \times \boldsymbol{f} + \boldsymbol{m} = \boldsymbol{0}, \tag{3.18}$$

where we insert the concrete formulas for $\boldsymbol{M}$, $\boldsymbol{F}$, $\boldsymbol{f}$, $\boldsymbol{m}$. We linearize these resulting equations as in section 2.3.3 using the identities

$$\Omega_1 \approx -Y'', \qquad \Omega_2 \approx X'', \tag{3.19a}$$

$$\mathbf{P}_\parallel \cdot \boldsymbol{e}_z = \boldsymbol{e}_3 \approx (X', Y', 1), \qquad \mathbf{P}_\perp \cdot \boldsymbol{e}_z \approx -(X', Y', 0), \tag{3.19b}$$

$$\text{and} \qquad \mathbf{P}_\perp \cdot (\boldsymbol{e}_z \times \boldsymbol{r}) \approx (-Y, X, 0), \tag{3.19c}$$

and ultimately arrive at

$$0 = -Y'''' + \partial_z(\hat{m}(1-\hat{z})X'') - \hat{f}_\parallel(1-\hat{z})Y'' - \hat{f}_\perp Y' + \hat{\chi}X, \tag{3.20a}$$

$$0 = \quad X'''' + \partial_z(\hat{m}(1-\hat{z})Y'') + \hat{f}_\parallel(1-\hat{z})X'' + \hat{f}_\perp X' + \hat{\chi}Y. \tag{3.20b}$$

Here we introduce the rescaled coordinate $\hat{z} = z/L_0$ and the dimensionless parameters $\hat{m} = mL_0^2/A_{\text{eff}}$, $\hat{f}_\parallel = f_\parallel L_0^3/A_{\text{eff}}$, $\hat{f}_\perp = f_\perp L_0^3/A_{\text{eff}}$, and $\hat{\chi} = \chi a_\perp L_0^4/A_{\text{eff}}$.

Equations (3.20) are quite general and several related problems follow from them. When forces $\hat{f}_\parallel$ and $\hat{f}_\perp$ vanish, they describe the writhing instability of rotating rods [123, 132]. For zero torque and precession frequency, and $\hat{f}_\parallel = -\hat{f}_\perp = \hat{f}_z$, one arrives at the classical example of a column that buckles under its own weight [74, 84]. A similar problem occurs for microtubuli that buckle under the action of molecular motors [60]. In our case, the force density $f_\parallel$ that causes buckling points along the rod axis and $f_\perp$ stabilizes the straight rod for non-zero v. In comparison, the column under gravity always experiences a force density along the vertical which gives a force component perpendicular to the rod as soon as it buckles and thereby supports buckling.

We complete the linearized dynamic equations (3.20) by writing the boundary conditions (3.8) in linearized and reduced form:

$$X(0) = 0 \qquad Y(0) = 0, \tag{3.21a}$$

$$X''(0) = -\hat{m}Y'(0) \qquad Y''(0) = \hat{m}X'(0), \tag{3.21b}$$

$$X''(1) = 0 \qquad Y''(1) = 0, \tag{3.21c}$$

$$X'''(1) = 0 \qquad Y'''(1) = 0. \tag{3.21d}$$

The first line means that the attached end of the rod can only move in z direction and not along the x and y axis. The second line means that a torque does not act perpendicular to the z-axis. So if the rod starts to buckle, the local torque $m\boldsymbol{e}_3$ has to be equilibrated by a bending moment. The free end of the rod is torque less and, therefore, the rod does not bend, as expressed by the third line. Finally, the free end is also force free and the fourth line follows from Eq. (3.7b) by setting $\boldsymbol{F} = \boldsymbol{0}$.

To search for nontrivial solutions of Eqs. (3.20) in our parameter space and thereby identify the buckling transition, we proceeded as follows. In addition, to the boundary conditions for (3.21a) and (3.21b), nontrivial solutions of the buckling equations (3.20) can be characterized by $X'(0)$, $Y'(0)$, $X'''(0)$ and $Y'''(0)$. The principal idea is to use them to generate solutions of Eqs. (3.20) and to fulfill the boundary conditions (3.21c) and (3.21d) at the free end by varying them. However, since $X'(0)$ and $Y'(0)$ just determine the amplitude of a bent configuration and merely fix the rotational degree of freedom about the z axis, they can be chosen arbitrary. Instead, we vary two of our four parameters, $\hat{f}_\perp$ and $\hat{\chi}$, to fulfill the four boundary conditions at $\hat{z} = 1$. As a result, for given $\hat{m}$ and $\hat{f}_\parallel$, we determine parameters $\hat{f}_\perp$ and $\hat{\chi}$ for which nontrivial solutions of the buckling equations exist and thereby identify the manifold of bifurcation points in our four-parameter space. We will discuss this in the following section.

3.3.2 Discussion

Figure 3.8(a) plots the manifold of bifurcation points. To each parameter triple $(\hat{m}, \hat{f}_\parallel, \hat{f}_\perp)$ belongs a specific value of the precession frequency $\hat{\chi}$ which we do not further discuss. At positive $\hat{f}_\perp$ and for small $\hat{m}$ and $\hat{f}_\parallel$, the straight configuration of the helical rod is stable. If we change the sign of $\hat{f}_\perp$, a bifurcation occurs which we interpret as an instability of the straight rod when it reorients towards the perpendicular configuration. We observe this instability in our simulations when we reverse the driving torque as discussed in sections 3.2.1 and 3.2.2. Here we keep the direction of the torque but reverse the sign of the velocity v and thereby the sign of $\hat{f}_\perp$ in Eq. (3.17) by reversing the chirality of the rod. The main result is the surface in dark yellow that belongs to the first buckling transition observed in our simulations. Therefore at large torque $\hat{m}$ the rod is buckled. Finally, at $\hat{f}_\perp \approx 0$ and large $\hat{m}$, a transition between two different configurations of the buckled rod occurs. An interesting feature is the ridge in the bifurcation surface. However, we could not determine any dramatic changes in the buckling of the rod close to this ridge.

Figure 3.8(b) shows buckling curves $\hat{f}_\parallel(\hat{m})$ for different values of the perpendicular force ranging from $\hat{f}_\perp = 0$ in steps of 25 to 300. At $\hat{f}_\perp = 0$ the typical parabolic curve occurs (see sec. 2.3.3). At constant but small value of m, the critical force $f_\parallel$ increases strongly with increasing $\hat{f}_\perp$. Likewise, one needs large forces $\hat{f}_\perp$ to stabilize the straight helical rod at high torques. The red dots are the critical forces and torques from figure 3.5(b) determined in our simulations plotted in reduced units. Note that the buckling curves develop a shoulder at $\hat{m}$ around 15 for increasing $\hat{f}_\perp$ due to the ridge in the manifold of bifurcation points in figure 3.8(a). The two simulation points at large m are close to this ridge. We speculate that the transition from a supercritical bifurcation observed in our simulations at low m to a subcritical bifurcation at large m is connected to the existence of this ridge.

In the rotating helical filament or helical rod, the forces $f_\parallel$ and $f_\perp$ and the torque m

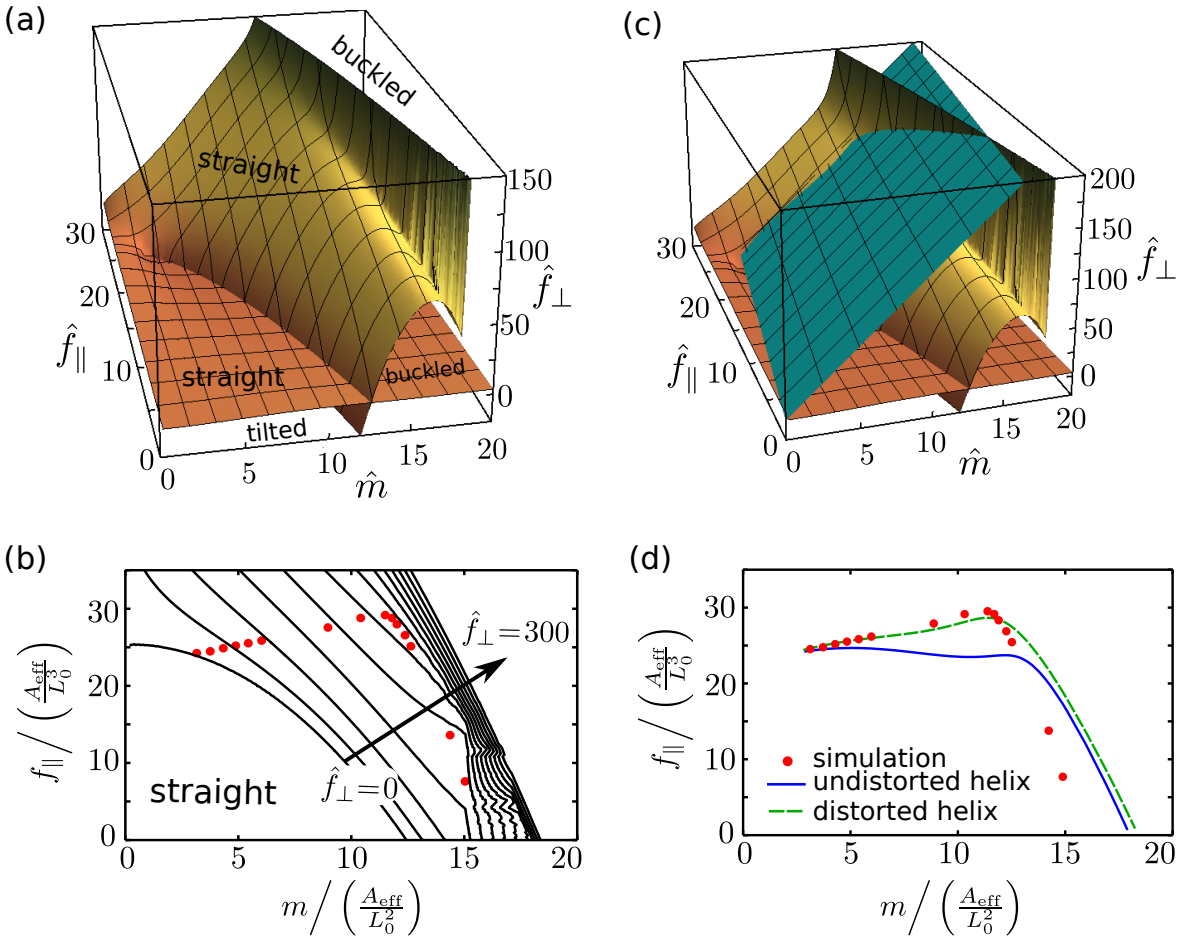

Abbildung 3.8: **(a)** Manifold of bifurcation points in the parameter space $(\hat{m}, \hat{f}_\parallel, \hat{f}_\perp)$. To each parameter triple belongs a specific value of the precession frequency $\hat{\chi}$. **(b)** Buckling curves $f_\parallel(m)$ for different values of the perpendicular force ranging from $\hat{f}_\perp = 0$ in steps of 25 to 300. The red dots are the critical forces and torques from figure 3.5(b). **(c)** The plane pictures relation (3.22) between $f_\parallel$, $f_\perp$, and m for the helical rod with constant friction coefficients. Intersecting it with the manifold of bifurcation points gives the buckling curves in **(d)**. Full blue line: for constant friction coefficients of the undistorted helix, dashed green line: torque-dependent friction coefficients.

are related to each other by the equations (3.11) and (3.17). Eliminating velocity v and angular frequency ω, one arrives at

$$f_\perp = \frac{a_\perp}{a_\parallel b_\parallel - c_\parallel^2} \left(b_\parallel f_\parallel - c_\parallel m \right), \tag{3.22}$$

with the friction coefficients (3.12). Relation (3.22) defines a plane in the parameter space $(\hat{m}, \hat{f}_\parallel, \hat{f}_\perp)$ which we intersect in figure 3.8(c) with the manifold of bifurcation points. The resulting bifurcation curve is then plotted in figure 3.8(d) as full blue line. At low m we have a remarkable quantitative agreement with our simulations (red dots) but we miss the slight increase of the critical force $f_\parallel$.

We already discussed that the location of the buckling transition is sensitive to small variations in the parameters. These variations come in by the elastic deformation of the helical filament that we discussed in section 3.2.3. We derived the change of the helical radius due the twisting by the applied torque, given in Eq. (3.6). When we regard the twist dependence of the friction coefficients $b_\parallel$ and $c_\parallel$ Eq. (3.22) becomes a nonlinear function in $m = M/L_0$. Intersecting it with the bifurcation manifold gives the green curve in figure 3.8(d) which nicely reproduces the critical force-torque relation for $\hat{m} < 10$. Our theory also gives the strong decrease of the critical force $f_\parallel$ at large m. However, in the effective model the bifurcation is shifted to larger torque values. This might be related to the ridge in the manifold of bifurcation points. Nevertheless, considering the fact that we approximate the helical filament by a rigid rod whose helicity comes in through the friction coefficients, we obtain a very good agreement with our simulations.

3.4 Summary and conclusions

Bacteria like *E.coli* move forward by rotating a bundle of helical flagella which creates a thrust force that pushes against the cell body. In this chapter we have modeled a single flagellum based on the discretized version of Kirchhoff's elastic rod theory and our coarse-grained approach for driving the helical filament by a motor torque. When increasing the motor torque, the thrust force reveals a supercritical Hopf bifurcation due to buckling of the helical filament. For further increased torque, a second buckling instability occurs. The Hopf bifurcation is also visible when we attach the flagellum to a spherical particle, which mimics the cell body, so that the whole model bacterium moves forward. We tune the thrust force pushing against the cell body via the size of the load particle. Therefore the critical torque for buckling changes, which results in a characteristic curve, critical force versus torque, for the buckling transition, which we have shown in figure 3.5(b).

We have developed a theory for the observed buckling transition by approximating the helical filament by a rod with an effective bending rigidity and the characteristic rotation translation coupling. The basic picture is that the filament buckles under the frictional forces and torques that act along the filament when it rotates. For large friction of the load particle, when its size is comparable to a bacterial cell body, buckling is mostly due to the thrust force created along the filament and similar to a rod that buckles under its own weight. In the limit of small friction of the load particle, the critical thrust force tends to zero and buckling is mostly driven by the frictional torque acting along the filament. However, our modeling reveals that subtle details of the specific problem are important. One has to take into account the precession of the buckled filament about the applied torque and, in particular, a perpendicular frictional force due to the motion of the model bacterium that stabilizes the filament against buckling. Finally, taking into account the small deformation of the rotating helical filament, we are able to obtain a quantitative agreement with the simulated graph, critical force versus torque, in the biologically relevant regime.

To further illustrate the biological relevance of the observed buckling transition, we first summarize a few experimental values. Hotani gives the torque for observing a polymorphic transition of the flagellum at around 1.1pNμm [54], whereas Darnton *et al.* mention a mean torque acting on a flagellum of about 1.4pNμm [30]. These values agree with the torques where we observe buckling for realistic cell body sizes (see figure 3.5). Reference [30] also mentions the relative stiffness of the helical filament so that it hardly deforms under rotation, which agrees with our simulations. Finally, thrust forces created by the bundle are given as 0.41 ± 0.23pN [30] or 0.5pN [22]. This agrees with an estimate $F = 6\pi\eta a v \approx 0.6$pN where we take the radius of the load particle as $a = 1\mu$m and use the swimming velocity $v = 30\mu$m/s. All these values are close but below the simulated values $F_{c1} \approx 1$pN for real cell sizes. However, we note that F_{c1} scales as A_{eff}/L_0^2, as our analytic model shows, and thereby depends on the explicit choice of the bending (A) and torsional (C) rigidities. We have chosen particular values for them and also set $A = C$

in our simulations. So F_{c1} will vary with the actual parameters.

It is clear that swimming bacteria should avoid buckling for efficient locomotion. However, they cannot simply increase the bending rigidity, since a certain flexibility is necessary during polymorphic transformations or when a bundle forms. Reference [121] shows pictures where single flagella are in a bent conformation similar to the buckled state in our simulations. This might be a hint that flagella naturally buckle under their own thrust. In peritrichous bacteria such as *E.coli* and *Salmonella*, several flagella form a bundle which then has larger bending stiffness and therefore buckling is not observed.

Monotrichous bacteria only use a single flagellum. Their conformation differs in pitch and radius from the flagella of peritrichous bacteria [38]. A detailed analysis shows that their swimming efficiency is reduced due to a smaller pitch angle with $\sin\alpha \approx 0.75$ [111]. This increases the critical force $F_{cr} \propto 1/\sin\alpha$ by about 10% compared to peritrichous bacteria and might be an adaption of the monotrichous bacteria to enhance the stability of their single flagellum.

We also showed that a pulling flagellum is not stably aligned along the applied torque. So most bacteria use their flagella to push themselves through the fluid. Nevertheless, there are some marine bacteria that use a back-and-forth rather than a run-and-tumble strategy for chemotaxis. They live in a turbulent aqueous environment in the ocean where they experience large shear gradients on the micron scale [85]. Simulations in reference [85] show that in addition to the shear-driven reorientation of the bacterium there must be further contributions to the reorientation. Besides rotational diffusion this could also be the unstable orientation of the rotating filament when it pulls the cell body. Recent experiments on the back-and-forth motion of marine bacteria *Vibrio alginolyticus* directly show this reorientation of the flagellum [133].

Kapitel 4

Force-extension curves of bacterial flagella – Stretching-induced polymorphic transformations

4.1 Introduction

In this chapter we present Brownian-dynamics simulations of the force-extension curves of bacterial flagella. These simulations are mainly motivated by recent experiments of Darnton and Berg [28]. With the help of an optical tweezer set up they pulled the two ends of the flagellar filament apart with a constant velocity and induced a transition between two polymorphic configurations. They then reversed the velocity to compress the flagellum in order to return it to the initial configuration. Darnton and Berg recorded force-extension curves mainly for the transformation from the coiled to the normal configuration. The transformation starts locally at one end of the flagellum and then proceeds in discrete steps along the flagellum. Signatures of the steps are clearly visible in the force-extension curves.

In literature there exist several approaches to describe force driven polymorphic transformations in bacterial flagella. We note that calculating the force-extension curves on the basis of coarse-grained molecular dynamics simulations is not possible since simulation times of a few microseconds are far below the experimentally relevant time scale in the order of seconds [2]. There also exist generalizations of Calladine model to an elastic theory of the flagella [37,112–114]. Nevertheless, modeling the polymorphism of a bacterial flagellum on a mesoscopic level is more appropriate. Goldstein *et al.* extended Kirchhoff's classic theory of an elastic rod by introducing a double-well potential for the spontaneous torsion to describe the transition between two helical states with opposed helicity [27, 40]. Wada and Netz also described the helical filament by Kirchhoff's rod theory but attached a spin variable along the filament in order to distinguish locally between the two helical states [126]. They then performed hybrid Brownian-dynamics Monte-Carlo simulations to numerically calculate force-extension curves of bacterial flagella.

In section 4.2 we introduce our extension of Kirchhoff's elastic rod theory to include

the polymorphism of the bacterial flagellum. We model the elastic free energy of the bacterial flagellum in the spirit of references [27, 40]. However, we show in section 4.2.2 that a conventional double-well potential cannot reproduce the experimentally observed force extension curves. We therefore develop an alternative model in section 4.2.3, where we just "glue" the harmonic elastic energies of the two helical states together. This approach is less time-consuming than the one of reference [126] but it is in the biologically relevant limit completely equivalent as we will demonstrate in section 4.2.4.

In section 4.3 we discuss the results for the simulated force-extension curves. We furthermore concentrate on different aspects, namely how they depend on the ratio of torsional and bending rigidities $\Gamma = C/A$ and on the velocity or extensional rate with which the flagellum is pulled apart. We also give an upper bound for Γ which is partially in contrast to experimental results.

The mean extension, at which a coiled-to-normal transition first occurs locally, is a function of the extension rate. We demonstrate in section 4.4 how this extension can be inferred from equilibrium properties of a clamped helical filament. We perform our simulations with realistic parameter values and can directly compare our results to experiments.

This chapter is based on publication [A].

4.2 Continuum model for the bacterial flagellum

4.2.1 Principles for extending Kirchhoff's rod theory

Geometric conditions

We start this section by discussing briefly the phenomenology that the elastic energy in our extended model should describe. Darnton and Berg showed in their experiments [28], that the force-extension curve before a transition corresponds to the force-extension relation of a helical spring (see Eq. (2.90)) deduced from Kirchhoff's rod theory. In order to describe the transition of the bacterial flagellum between two polymorphic configurations, i.e. from coiled to normal, the Kirchhoff rod theory has to be extended to include two local ground states characterized by the rotational strain vector $\boldsymbol{\Omega}_i$ $(i = 1, 2)$. To choose proper values for the intrinsic strain, we have to recall the molecular structure of the filament at which we attach the material frame $\{\boldsymbol{e}_1, \boldsymbol{e}_2, \boldsymbol{e}_3\}$.

In section 2.1.1 we described that the flagellar filament consists of eleven protofilaments that assume two configurations (L and R) that mainly differ in length and so cause the bending of the flagellum. For the coiled filament with three protofilaments in the R-state we choose the Frenet frame as material frame. Consequently we have $\boldsymbol{\Omega}_1 = (0, \kappa_1, \tau_1)$ where κ_1 and τ_1 are the curvature and torsion of the coiled state, respectively (see section 2.1.1). The normal vector corresponds to the material vector $\boldsymbol{e}_1$ and for symmetry reasons points to the central one of the three R-state protofilaments. During a transition from coiled to normal, one of the two marginal R-state protofilaments has to switch into the L-state. As a consequence the new normal vector is slightly rotated to the material vector $\boldsymbol{e}_1$ by an angle of $|\delta\varphi| = \frac{2\pi}{22}$. For simplicity we neglect the small rotation in this work and approximate the intrinsic rotational-strain vector by $\boldsymbol{\Omega}_2 = (0, \kappa_2, \tau_2)$, with the curvature κ_2 and torsion τ_2 of the normal state. Nevertheless we point out, that for transitions between several polymorphic forms as observed in the tumbling of *E.coli*, this phase-shift in the spontaneous curvature is important.

To summarize, the Kirchhoff rod theory has to be extended by including two local ground states characterized by $\boldsymbol{\Omega}_i = (0, \kappa_i, \tau_i)$ $(i = 1, 2)$. Because only one state occurs at mechanical and thermal equilibrium we also will need a tuneable energy difference δ between the two ground states. In the next subsections we will introduce two energies according to these conditions.

Energy for connecting two helical states

The elastic free energy densities that we will introduce below in accordance to our previous geometrical conditions, admit that two domains of different polymorphic states are separated from each other by a sharp domain wall of zero width. To realize a more realistic, smoother transition between two domains, we introduce an additional strain-

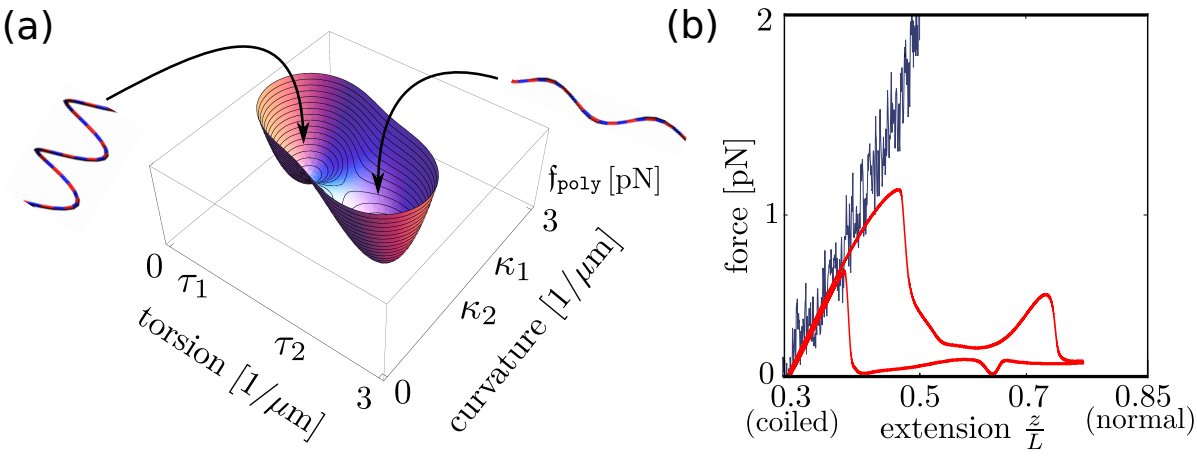

Abbildung 4.1: **(a)** Double-well potential of Eq. (4.3a) plotted as a function of $\Omega_2 = \kappa$ and $\Omega_3 = \tau$ for the parameters of the coiled and normal helical state. **(b)** Red line: Force-extension curve simulated with this potential at $T = 0$ and $v_p = 2\mu\text{m/s}$. Blue line: Force-extension curve comparable to the experimental curves of reference [28] simulated with the Kirchhoff potential at $T > 0$.

gradient energy density of the form [40]

$$f_{bi}(\mathbf{\Omega}') = \frac{\gamma}{2}(\mathbf{\Omega}')^2 , \tag{4.1}$$

with the derivative of the rotational strain rate $\mathbf{\Omega}'$ and the strain-gradient coefficient $\gamma^{1/2}$, which determines the width of the domain wall. For the energy (4.4), which we use in our simulations below, this domain wall width is given by $2\sqrt{\gamma/A}$ with the bending rigidity A.

Goldstein *et al.* [40] related the domain wall size to experimentally observed kink angles between two domains of different polymorphic states [54] and found an upper bound in the order of 0.1μm. On the other side we have to ensure in simulations that the width is large enough to be resolved by our discretization. Otherwise the helical filament contains several domains instead of just two. So we have chosen mostly $\gamma = 0.1\text{pN}\mu\text{m}^4$ corresponding to a domain wall of $\sim 0.3\mu\text{m}$ which is 50% larger than our discretization length.

4.2.2 The double-well potential does not reproduce the experiments

We first tried to generalize the approach of Goldstein *et al.*, who used a typical double well potential for the twist density Ω_3 realized by a polynomial of degree four, to describe two polymorphic states of a flagellum [27, 40]. Whereas the Kirchhoff elastic free energy

can be interpreted as a second order expansion in the rotational strain vector, Goldstein's ansatz includes corrections up to fourth order.

In order to develop a strategy to generalize the double well potential to all three coordinates Ω_i $(i = 1, 2, 3)$ of the angular strain vector $\boldsymbol{\Omega}$, we first write down a general one-dimensional polynomial of degree four:

$$f(x, x_1, x_2) = \frac{A}{2}\frac{(x - x_1)^2}{(x_1 - x_2)^2}[(x - x_2)^2 - \frac{d}{6}(x - x_1)(3x + x_1 - 4x_2)], \tag{4.2a}$$

$$\text{with } \delta = \frac{1}{12}A(x_1 - x_2)^2 d. \tag{4.2b}$$

For $d < 1$ it has two local minima at x_1 and x_2 with $f(x_1) = 0$ and $f(x_2) = \delta$, respectively. Whereas $f''(x_1) = A$, the second derivative of f at x_2 depends on the parameters x_1, x_2, d, and A.

We generalize the polynomial of Eq. (4.2a) to three dimensions by replacing terms of the form Axy by $\boldsymbol{x} \cdot \mathbf{A} \cdot \boldsymbol{y}$, where $\boldsymbol{x}$, $\boldsymbol{y}$ are three-dimensional vectors and $\mathbf{A}$ is a diagonal matrix with $A_{11} = A_{22} = A$ and $A_{33} = C$. The constants A, C are the bending and torsional rigidities, respectively. Using the shorthand notation $|\boldsymbol{x}|^2_{\mathbf{A}} = \boldsymbol{x} \cdot \mathbf{A} \cdot \boldsymbol{x}$ with $\boldsymbol{x} = \boldsymbol{\Omega} - \boldsymbol{\Omega}_i$, we now write

$$\mathfrak{f}(\boldsymbol{\Omega}, \boldsymbol{\Omega}_1, \boldsymbol{\Omega}_2) = \frac{1}{2}\frac{|\boldsymbol{\Omega} - \boldsymbol{\Omega}_1|^2_{\mathbf{A}}}{|\boldsymbol{\Omega}_1 - \boldsymbol{\Omega}_2|^2_{\mathbf{A}}}[|\boldsymbol{\Omega} - \boldsymbol{\Omega}_2|^2_{\mathbf{A}} - \frac{d}{6}(\boldsymbol{\Omega} - \boldsymbol{\Omega}_1) \cdot \mathbf{A} \cdot (3\boldsymbol{\Omega} + \boldsymbol{\Omega}_1 - 4\boldsymbol{\Omega}_2)] \tag{4.3a}$$

$$\text{with } \delta = \frac{1}{12}|\boldsymbol{\Omega}_1 - \boldsymbol{\Omega}_2|^2_{\mathbf{A}} d. \tag{4.3b}$$

The polynomial is illustrated in figure 4.1(a) with $\boldsymbol{\Omega} = (0, \kappa, \tau)$. It has two minima at $\boldsymbol{\Omega}_1$, $\boldsymbol{\Omega}_2$ with $\mathfrak{f}(\boldsymbol{\Omega}_1) = 0$, $\mathfrak{f}(\boldsymbol{\Omega}_2) = \delta$, respectively, and one saddle point at $\boldsymbol{\Omega}_3 = \boldsymbol{\Omega}_1 + \frac{1}{2-d}(\boldsymbol{\Omega}_2 - \boldsymbol{\Omega}_1)$ for $d < 1$. Close to the first minimum at $\boldsymbol{\Omega}_1$, the polynomial agrees with Kirchhoff's elastic free energy (2.46), whereas the bending and torsional rigidities at $\boldsymbol{\Omega}_2$ and also the energy barrier depend on δ. So this ansatz fulfills the conditions for the extended elastic energy formulated before.

Figure 4.1(b) shows a force-extension curve (red line) simulated with Eq. (4.3a) at $T = 0$ with $\Gamma = 1$. For comparison we included a force-extension curve that is comparable to the initial part of the experimental ones described in reference [28]. For that we simulated a helical filament with pure Kirchhoff energy and the same parameters as before at finite temperature. The helical filament with the double well potential is much softer and the initial part of the force-extension relation has a negative curvature in contrast to experiments. We, therefore, decided to introduce an alternative model that we will describe in the following section.

4.2.3 Extended Kirchhoff rod theory

In this section we explain our extended Kirchhoff model that we will use for the simulations of the force-extension curves in the next section. To each of the two relevant

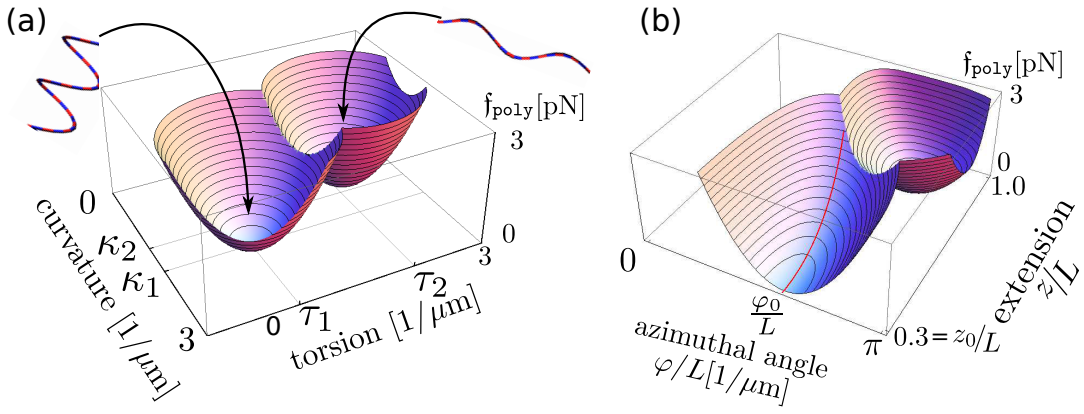

Abbildung 4.2: **(a)** Free energy density $\mathfrak{f}_{\mathtt{poly}}$ from Eq. (4.4) as a function of curvature κ and torsion τ using $\boldsymbol{\Omega} = (0, \kappa, \tau)$. **(b)** Free energy density $\mathfrak{f}_{\mathtt{poly}}$ as a function of height z and azimuthal angle per unit length φ/L of a uniformly stretched helical filament (see section 2.5.2). The red lines indicate the path of the helical filament in the energy landscape during stretching.

polymorphic forms of the flagellum we assign the elastic free energy of Kirchhoff's rod theory. Furthermore we introduce a difference δ of the two energy densities in the ground states. Since the free energy of a system always assumes a minimum, we locally assign to a bacterial flagellum with angular strain $\boldsymbol{\Omega}$ the minimum $\mathfrak{f}_{\mathtt{poly}}(\boldsymbol{\Omega}, \boldsymbol{\Omega}_1, \boldsymbol{\Omega}_2)$ of the free energy densities of the two polymorphic configurations:

$$\mathfrak{f}_{\mathtt{poly}}(\boldsymbol{\Omega}, \boldsymbol{\Omega}_1, \boldsymbol{\Omega}_2) = \min\left(\mathfrak{f}_{\mathtt{cl}}(\boldsymbol{\Omega}, \boldsymbol{\Omega}_1), \mathfrak{f}_{\mathtt{cl}}(\boldsymbol{\Omega}, \boldsymbol{\Omega}_2) + \delta\right), \tag{4.4}$$

where $\mathfrak{f}_{\mathtt{cl}}$ is the elastic free energy density of Eq. (2.46). We show the resulting energy density $\mathfrak{f}_{\mathtt{poly}}(\boldsymbol{\Omega}, \boldsymbol{\Omega}_1, \boldsymbol{\Omega}_2)$ in figure 4.2(a) for $\Omega_1 = 0$ and $\Gamma = 1$ as a function of curvature $\Omega_2 = \kappa$ and torsion $\Omega_3 = \tau$. figure 4.2(b) shows the energy in the variables of a uniformly deformed helical spring, i.e. the azimuthal angle per unit length φ/L and the relative extension z/L (see section 2.5.2).

Note that our ansatz can easily be extended to describe more than two of the polymorphic states of bacterial flagella. In particular, this will be necessary for understanding the sequence of polymorphic transitions during the tumbling phase of *E.coli*.

Collecting all the contributions, the total elastic free energy

$$\mathcal{F} = \int_0^L \mathfrak{f}(\boldsymbol{\Omega}, \boldsymbol{\Omega}', \boldsymbol{\Omega}_1, \boldsymbol{\Omega}_2) + \mathfrak{f}_{\mathtt{st}}(\boldsymbol{r}')\mathrm{d}s, \tag{4.5a}$$

which we will use in the following for modeling the bacterial flagellum, is based on the stretching energy $\mathfrak{f}_{\mathtt{st}}(\boldsymbol{r}')$ that ensures the inextensibility of the filament in the numerical variation as described in section 2.4 and the density

$$\mathfrak{f} = \mathfrak{f}_{\mathtt{poly}}(\boldsymbol{\Omega}, \boldsymbol{\Omega}_1, \boldsymbol{\Omega}_2) + \mathfrak{f}_{\mathtt{bi}}(\boldsymbol{\Omega}') \tag{4.5b}$$

with the strain-gradient energy $\mathfrak{f}_{\mathtt{bi}}(\boldsymbol{\Omega}')$ that gives the domain wall between the two polymorphic states an energy as given in Eq. (4.1).

4.2.4 Relation to the free energy of Wada and Netz

Wada and Netz formulated an alternative, statistical model to access the polymorphism of the bacterial flagellum [126] which they described as a bead-spring chain. To each bead they assigned the Kirchhoff free energy and an Ising spin to distinguish locally between the two polymorphic forms of the flagellum. The Ising spin Hamiltonian then favored the same polymorphic state for adjacent beads. By integrating out the spin degree of freedom, they derived an effective elastic free energy density:

$$\mathfrak{f}(\boldsymbol{\Omega}, \boldsymbol{\Omega}_1, \boldsymbol{\Omega}_2) = \mathfrak{f}_1 - \mathfrak{f}_2, \tag{4.6a}$$

with

$$\mathfrak{f}_1 = \frac{A}{2}\Omega_1^2 + \frac{A}{2}\left(\Omega_2 - \frac{\kappa_1+\kappa_2}{2}\right)^2 + \frac{C}{2}\left(\Omega_3 - \frac{\tau_1+\tau_2}{2}\right)^2, \tag{4.6b}$$

$$\mathfrak{f}_2 = \frac{k_B T}{a}\ln\left[\cosh(\Lambda) + \sqrt{\sinh^2(\Lambda) + \mathrm{e}^{-4J/k_BT}}\right] + \frac{J}{a}, \tag{4.6c}$$

and

$$\frac{k_BT}{a}\Lambda = \delta + \frac{A}{2}(\kappa_1-\kappa_2)\left(\Omega_2 - \frac{\kappa_1+\kappa_2}{2}\right) + \frac{C}{2}(\tau_1-\tau_2)\left(\Omega_3 - \frac{\tau_1+\tau_2}{2}\right). \tag{4.6d}$$

Here A, C are the bending and torsional rigidities, respectively, δ is the difference of the ground-state energies of the helical conformations (κ_1, τ_1) and (κ_2, τ_2), and a is the length of discretization. The quantity J is the interaction strength in the Ising spin Hamiltonian.

In experiments, where a thermally induced transition from the *normal* to the *semicoiled* configuration was studied, most flagella assumed a pure polymorphic form of either the normal or semicoiled state [48] suggesting that the energy cost for forming a domain wall between the two helical states is much larger than thermal energy. Using this observation, we demonstrate that the free energy density of Wada and Netz simplifies to our elastic free energy (4.4).

We interpret the energy cost $2J$ for two anti-parallel spins as the energy of a domain wall connecting two helical states. We simplify $\mathfrak{f}_2$ using $k_BT \ll J$ to obtain

$$\mathfrak{f}_2 \approx \frac{k_BT}{a}|\Lambda| + \frac{J}{a}, \tag{4.7}$$

where we used $\cosh x + |\sinh x| = \exp|x|$. Now, we introduce the elastic free energy densities of the two helical states,

$$\alpha = \frac{A}{2}\Omega_1^2 + \frac{A}{2}(\Omega_2-\kappa_2)^2 + \frac{C}{2}(\Omega_3-\tau_2)^2 + \delta/2, \tag{4.8}$$

$$\beta = \frac{A}{2}\Omega_1^2 + \frac{A}{2}(\Omega_2-\kappa_1)^2 + \frac{C}{2}(\Omega_3-\tau_1)^2 - \delta/2, \tag{4.9}$$

and write the two contributions to the energy density (4.6) up to a constant as

$$\mathfrak{f}_1 = \frac{1}{2}(\alpha + \beta) + const, \qquad \mathfrak{f}_2 \approx \frac{1}{2}|\alpha - \beta| + \frac{J}{a}. \tag{4.10}$$

This finally gives our ansatz for the free energy density (4.4):

$$\mathfrak{f} \approx \frac{1}{2}(\alpha + \beta - |\alpha - \beta|) + const = \min(\alpha, \beta) + const. \tag{4.11}$$

Therefore our ansatz is equivalent to the elastic free energy of Wada and Netz in the biologically relevant limit. Hence we do not take into account the spin dynamics our model is simpler and less time consuming.

4.3 Force-extension curves

4.3.1 Pulling on and compressing the helical filament

We performed both Stokesian (temperature $T = 0$) and Brownian dynamics ($T = 300K$) simulations of the force-extension measurements in reference [28]. Similar to the experimental setup, we fix one end of the filament whereas the other end is allowed to move in a harmonic potential with trap stiffness $100\,\mathrm{pN}/\mu\mathrm{m}$ (as in reference [28]) mimicking the experimental situation where a bead attached to the bacterial flagellum was trapped by an optical tweezer. The axis of the helical filament is oriented parallel to the z axis. In the beginning, the minimum of the harmonic potential coincides with one end of the filament in the initial coiled state. We then move the potential with a constant velocity v_p along the z axis and the filament stretches. After reaching a maximum extension $\zeta_M = z_M/L$, the potential is moved with the opposite velocity $-v_p$ back into the initial position. Note that in experiments the extension rates were $v_p = 0.4\mu\mathrm{m/s}$ and less [28]. Such small velocities are very time consuming in our simulations so that we typically chose values from the range $v_p = 2, \ldots, 20\mu\mathrm{m/s}$ for recording the complete force-extension curve. When we were just monitoring the initial part of the curve, we used velocities as small as $v_p = 0.2\mu\mathrm{m/s}$ (see section 4.4). We note that the used extension rates are much smaller than the characteristic velocity $v_c = 10^3\mu\mathrm{m/s}$ with which a disturbance relaxes through the filament, as derived in section 2.5.4. So the extending filament passes through a sequence of equilibrium configurations. This also means that the applied and elastic forces nearly balance each other since they are much larger than the frictional forces.

We first simulated the extension of a filament with only one helical state. Similar to the snapshots 1 and 2 in figure 4.3(a), the deformation of the filament is uniform except for small regions at both ends. This leads to a small deviation of the simulated force-extension curve from the theoretical prediction of Eq. (2.90) for a uniformly stretched filament. The situation is similar to the results in figure 4.3(b), where the initial part 1-2 of the simulated blue curve is compared to the analytic prediction (thin black line). If we even shift the thin black line to the right, the dashed black line agrees very well with the blue curve besides the initial part close to position 1. We checked that even this difference gradually vanishes with increasing the height of the helix as expected. Furthermore, we do not observe any pronounced difference between deterministic Stokesian and Brownian dynamics simulations. For $T \neq 0$, the forces fluctuate around a value which agrees with the deterministic force at $T = 0$.

We then determined the force-extension curve at $T = 0$ when the helical filament can switch from the coiled to the normal state using the elastic free energy (4.5). The results are illustrated in figure 4.3, where the blue curve in (b) corresponds to $T = 0$. At a certain extension (position 2) the measured force drops sharply since a small segment of the filament close to the fixed end switches into the normal state as snapshots 2 and 3 in figure 4.3(a) reveal. Then the filament is stretched again. Further adjacent

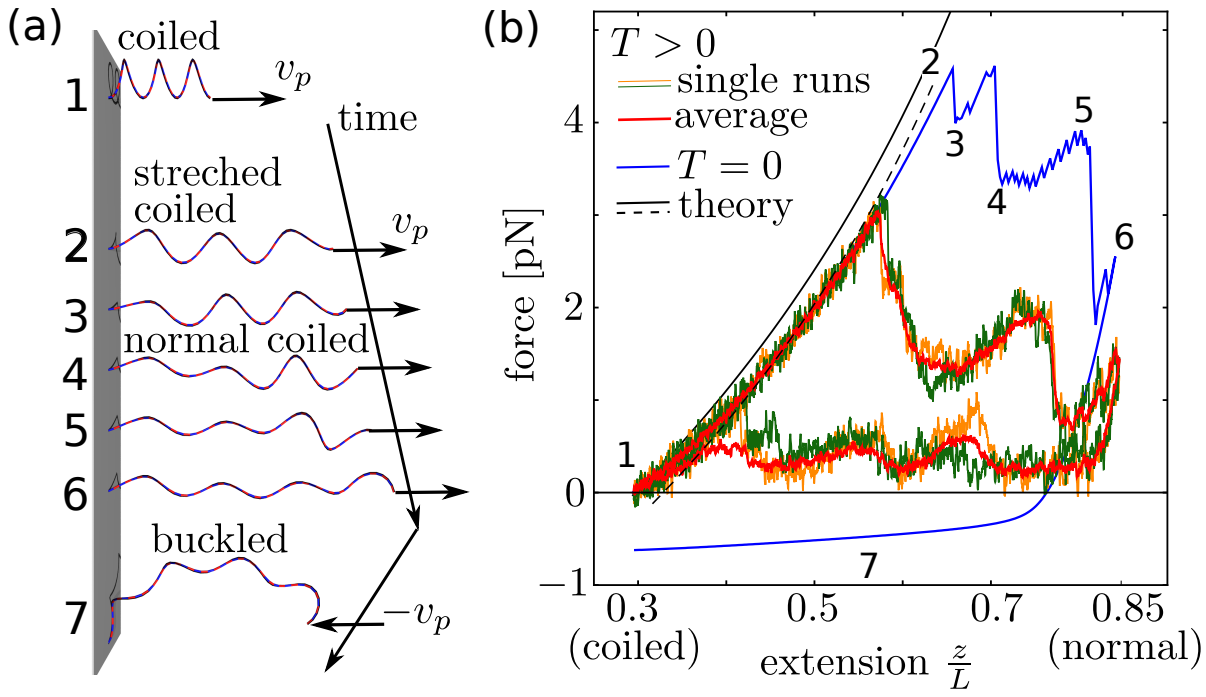

Abbildung 4.3: **(a)** Snapshots of a helical filament stretched at $T = 0$ with velocity $v_p = 2\mu$m/s. The coiled-to-normal transition ($v_p > 0$) and buckling ($v_p < 0$) are visible. **(b)** Force-extension curves simulated without thermal noise ($T = 0$) (blue curve) and with thermal noise: two realizations (thin orange and green lines) and an average over 10 runs (thick red line) are shown. The parameters are $v_p = 2\mu$m/s and $\Gamma = 0.7$. The analytic prediction for a uniformly stretched helix (thin black line) and its shifted curve (dashed black line) are shown. The numbers indicate the extension of the snapshots in (a).

segments transform suddenly until at position 6 the filament is nearly completely in the normal state. From here we invert the velocity v_p and move both ends together. However, the filament does not transform back into the coiled state but remains in the normal state. This ultimately leads to a negative force under which the filament buckles [see snapshot 7 in figure 4.3(a)]. We estimate the buckling force using the critical force $F_c = \pi^2 A_{\mathtt{eff}}/L_0^2 \approx 0.4\text{pN}$ of a rod with length $L_0 = L\sin\alpha$ and hinged ends (see Eq. (2.60) with $M_c = 0$) and the effective bending rigidity $A_{\mathtt{eff}}$ (see Eq. (2.95)) of the normal form of the bacterial flagella which is in good agreement with the simulation. In the supplementary material of publication [A], movie 1 shows the full cycle.

Brownian dynamics simulations reveal the influence of thermal fluctuations on the force-extension curve. Two realizations are included in figure 4.3(b) as thin lines and the thick red line shows an ensemble average over 10 runs. In the supplementary material of publication [A], movie 2 shows the full cycle. Clearly, the first transition into the normal state occurs at a smaller extension compared to the deterministic case since thermal fluctuations help to overcome the energy barrier in the elastic free energy density (see figure 4.2). Whereas the force in each realization fluctuates visibly, the sharp decrease of the force when a local transition into the normal state occurs is as pronounced as in the deterministic case. Finally, when both ends of the filament are moved together, it completely transforms back to the coiled state and buckling is not observed. The single realizations of the complete cycle of the force-extension curve closely resemble the experimental curves in figures 5 and 6 of reference [28]. In particular, the force and extension where the first coiled-to-normal transition occurs fall into the experimental ranges of 3 to 5pN and $z/L = 0.55$ to 0.6, respectively.

We now discuss in more detail how the difference δ in the ground-state energies of the two helical states, the twist-to-bend ratio Γ, and the extension rate v_p influence the force-extension curves.

4.3.2 Ground-state energy difference of the coiled and normal state

Increasing the ground-state energy $\delta > 0$ of the normal relative to the coiled state also increases the energy barrier, which the flagellum in the coiled configuration has to overcome to transform locally into the normal state. Therefore, the transition is delayed to a larger extension z/L or does not occur at all. On the other hand, the barrier which the normal configuration has to overcome to relax back into the coiled state decreases and buckling of the filament becomes less probable. Observations also show that a filament prepared in the normal state very slowly relaxes back into the coiled state, so δ should not be too large compared to thermal energy k_BT. By also using the following quantitative considerations, we adjusted δ to 0.1pN which resulted in good agreement with experimental observations, as already demonstrated.

We now derive an upper bound for δ to ensure that a transformation from the coiled to the normal state is, in principal, observable. The locus of the energy barrier in the

κ-τ-plane of figure 4.2 is given by

$$\mathfrak{f}_{\mathtt{c1}}(\mathbf{\Omega}, \mathbf{\Omega}_1) = \mathfrak{f}_{\mathtt{c1}}(\mathbf{\Omega}, \mathbf{\Omega}_2) + \delta, \tag{4.12}$$

where $\mathbf{\Omega} = (0, \kappa, \tau)$ and $\mathbf{\Omega}_i = (0, \kappa_i, \tau_i)$ contains the values for spontaneous bend κ_i and torsion τ_i of the coiled ($i = 1$) and normal state ($i = 2$), respectively. Assuming both states have the same elastic constants A, C, we arrive at a straight line

$$\kappa(\kappa_1 - \kappa_2) + \tau\Gamma(\tau_1 - \tau_2) + \delta/A = \frac{1}{2}\left[(\kappa_1^2 - \kappa_2^2) + \Gamma(\tau_1^2 - \tau_2^2)\right]. \tag{4.13}$$

We will use this formula later. The ground-state energy density of the normal state at $\mathbf{\Omega}_2 = (0, \kappa_2, \tau_2)$ is δ. Only if δ lies below the energy density of the coiled state at $\mathbf{\Omega} = \mathbf{\Omega}_2$, a clear transition between both states is possible. The explicit form of this upper bound, $\delta < f_{cl}(\mathbf{\Omega}_2, \mathbf{\Omega}_1)$, combines with $\delta > 0$ to the inequality

$$0 < \frac{\delta}{A(\kappa_1 - \kappa_2)^2} < \frac{1}{2}(1 + \Gamma\Delta^2), \qquad \text{where} \quad \Delta = \frac{\tau_1 - \tau_2}{\kappa_1 - \kappa_2}, \tag{4.14}$$

is the ratio of the differences in spontaneous torsion and curvature.

In experiments the value of δ changes with the conditions of the solvent. In particular, different polymorphic forms of the bacterial flagellum become stable when one alters the pH value, ionic strength, or temperature of the aqueous environment [48]. It would be interesting to perform the force-extension experiments under different conditions to investigate how a changing δ but also variations in bending (A) and torsional (C) rigidity influence the force-extension curve of a bacterial flagellum.

4.3.3 Twist-to-bend ratio

Increasing the twist-to-bend ratio Γ also increases the energy barrier $\Delta\mathfrak{f}_b$ as the following formula for the minimum value of the barrier demonstrates,

$$\frac{\Delta\mathfrak{f}_b}{A(\kappa_1 - \kappa_2)^2} = \frac{1}{8}\frac{\left(1 + \Gamma\Delta^2 + 2\delta/[A(\kappa_1 - \kappa_2)^2]\right)^2}{1 + \Gamma\Delta^2}. \tag{4.15}$$

However, in contrast to δ an increasing Γ increases both barriers for the coiled-to-normal and the normal-to-coiled transition.

We now discuss in figure 4.4(a) how the twist-to-bend ratio Γ influences the force-extension curve of the helical filament. The filament is stretched to an extension $z/L = 0.95$, well above the equilibrium height $z/L = 0.85$ of the normal state. Figure 4.4(b) shows contour plots of the elastic free energy density as a function of curvature and torsion for the same Γ as in (a). The red line indicates the sequence of κ, τ values, as the filament in the coiled state is uniformly stretched. Note that for $\Gamma \neq 1$, the anisotropy of the elastic free energy density is clearly visible.

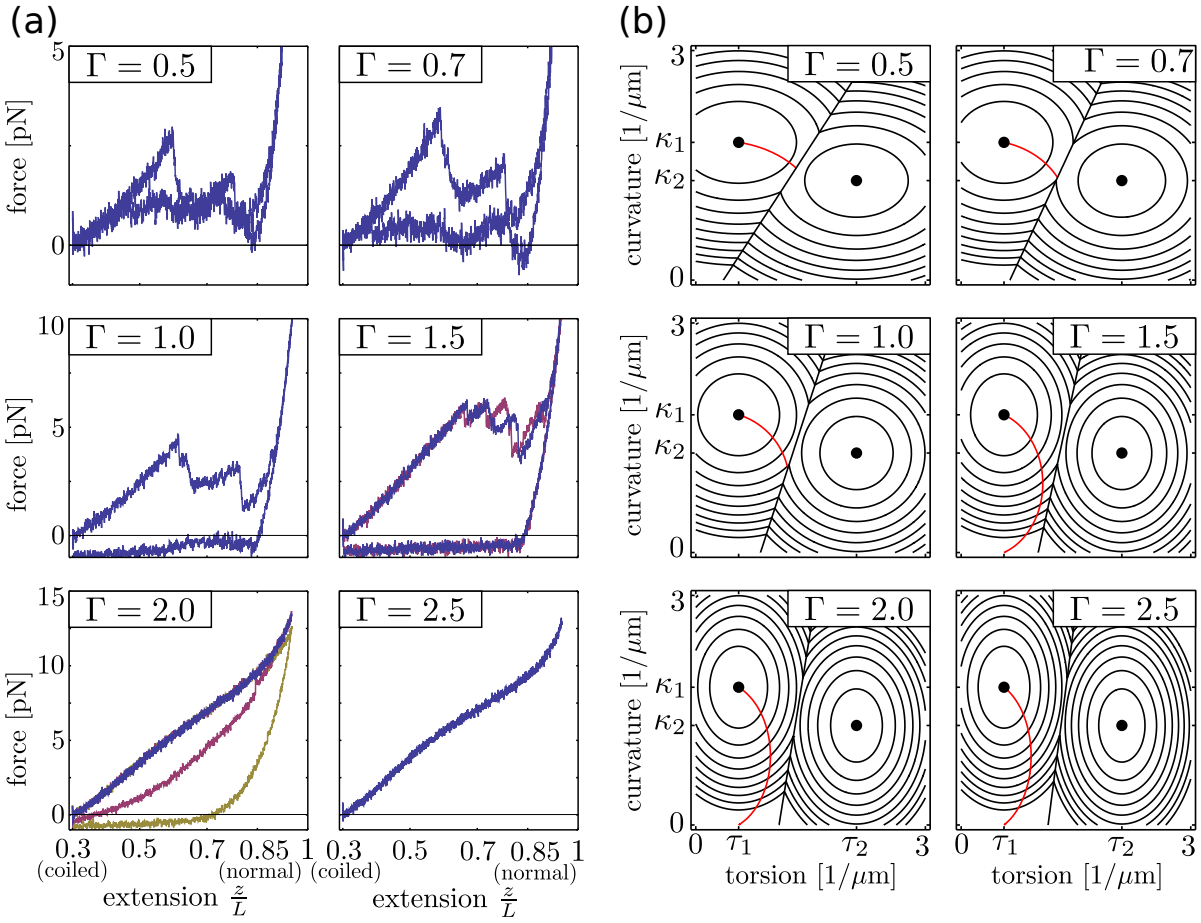

Abbildung 4.4: **(a)** One or several realizations of force-extension curves for increasing twist-to-bend ratios Γ. The extensional rate is $v_p = 2\mu$m/s. **(b)** Contour plots of the elastic free energy density as a function of curvature and torsion for the same Γ as in (a). The red line indicates the sequence of κ, τ values, as the filament in the coiled state is uniformly stretched.

For $\Gamma = 0.5$ and 0.7, one observes the typical force-extension curves as already discussed in figure 4.3, also for $\Gamma = 0.7$. Since now the maximal extension $z/L = 0.95$ is larger, the curve for $\Gamma = 0.7$ during compression looks different. While at $z/L = 0.95$ the entire filament is in the normal state, the filament for $\Gamma = 1$ no longer transforms completely into the normal state. Most pronounced at $\Gamma = 1$ is the fact that even with thermal forces the filament does not return into the coiled state during compression. This results in a negative force under which the filament buckles. All the force-extension curves in figure 4.4(a) are determined for an extension rate $v_p = 2\mu\text{m/s}$. A smaller v_p enhances the probability that thermal fluctuations transform the filament back into the coiled state and buckling is not observed. The same is true for a smaller extension where a larger part of the filament stays in the coiled state and makes it easier for the rest of the filament to return to the coiled state. At a ratio $\Gamma = 1.5$ the force-extension curve changes qualitatively. A first transition into the normal state occurs at a larger extension $z/L \approx 0.65$ compared to the previous curves. The transitions are no longer as pronounced and there are larger differences between single realizations of the force-extension curve. In addition, for $\Gamma < 1.5$ only one normal domain occurs whereas for $\Gamma = 1.5$ two normal domains are observed. The reason for all these features becomes clear from figure 4.4(b). At $\Gamma = 1.5$ a uniformly stretched filament does not hit the energy barrier anymore but passes the barrier in a close distance so that thermal fluctuations are needed to induce transformations into the normal state. For further increase of Γ a transition into the normal state does not occur at all realizations, as the three graphs for $\Gamma = 2$ demonstrate. A similar behavior is observed in reference [28] for a transition from the normal into the hyperextended state. The blue curve corresponds to the traditional force-extension relation of the helix in the coiled state. In the yellow curve a complete transition into the normal state was realized. A partial transformation occurred in the magenta curve which then completely returned into the coiled state. Finally, at $\Gamma = 2.5$ the filament always remains in the coiled state. Beyond an extension of $z/L = 0.5$ the slope of the curve becomes smaller. This is the onset of a qualitatively new behavior. At even larger Γ and $\tau_0/\kappa_0 < 1$, one observes a sharp drop in the force due to a discontinuous transformation, where one turn of the helical filament unwinds. This is discussed in references [63, 125].

As discussed, when neglecting thermal fluctuations, a coiled-to-normal transition is no longer observable in the force-extension curve, when in figure 4.4(b) the straight line [Eq. (4.13)] separating the coiled and normal state becomes tangential to the trajectory of the uniformly stretched filament. In section 2.5.2 we have seen that this trajectory is given by an ellipse [Eq. (2.91)]. Combining both equations leads to a second condition for the ground-state energy difference δ/A

$$\frac{\delta}{A(\kappa_1-\kappa_2)^2} < \frac{1}{2(\kappa_1-\kappa_2)}\left(\kappa_2 + \Gamma\tau_2\Delta + \sqrt{(1+\Gamma\Delta^2)(\kappa_1^2+\Gamma\tau_1^2)}\right). \tag{4.16}$$

Together with condition (4.14), we obtain a region in the parameter space $(\Gamma, \delta/A)$ where a transformation from the coiled to the normal state should occur. The region

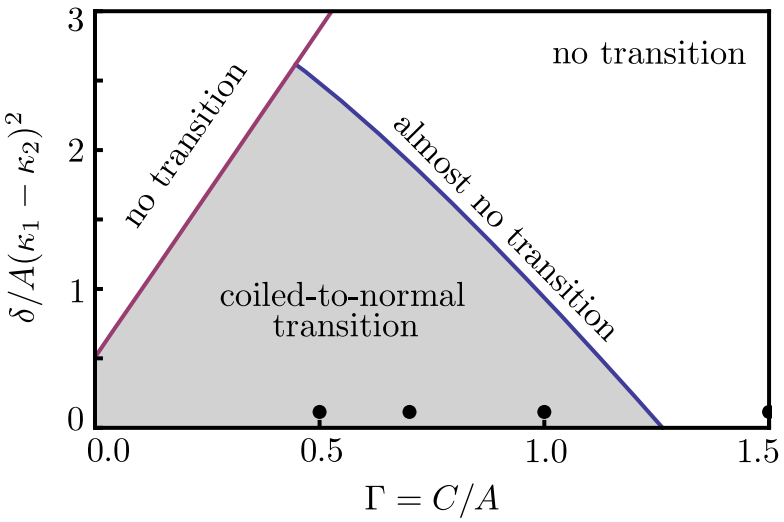

Abbildung 4.5: The shaded area indicates the parameter ranges for the ground-state energy difference δ and the twist-to-bend ratio Γ for which a coiled-to-normal transition should be observed. The dots give parameter values used in simulations. Note that thermal fluctuations shift the upper border for Γ indicated by the blue line to the right.

is indicated as shaded area in figure 4.5. Based on experimental data for the Young's and shear modulus in literature, Flynn and Ma received for the twist-to-bend ratio Γ the range $10^{-1} - 10^{2}$ [36]. With a computational method, called the quantized elastic deformational model, they calculated $\Gamma \approx 23$ [36]. On the other hand, together with our value $\delta/[A(\kappa_1 - \kappa_2)^2] \approx 0.11$, we predict a value of $\Gamma \lesssim 1$, in good agreement with our simulations.

4.3.4 Extensional rate

In section 4.3.1 we reasoned that during the measurements of the force-extension curves the bacterial flagellum goes through a sequence of equilibrium states. This means that frictional forces acting on the filament through the solvent are negligible against elastic forces. Therefore, without thermal noise, the force-extension curve does not depend on the extensional rate v_p. In contrast, our Brownian dynamics simulations demonstrate a clear influence of v_p. In figure 4.6, we show force-extension curves for twist-to-bend ratios $\Gamma = 0.7$ and 1 and different extension rates $v_p = 2\mu\text{m/s}$, $5\mu\text{m/s}$ and $20\mu\text{m/s}$. The first transition from the coiled to normal state occurs at larger extensions when v_p is increased. This is immediately clear since smaller velocities v_p give the filament more time to explore the energy landscape with the help of thermal fluctuations. So the appropriate

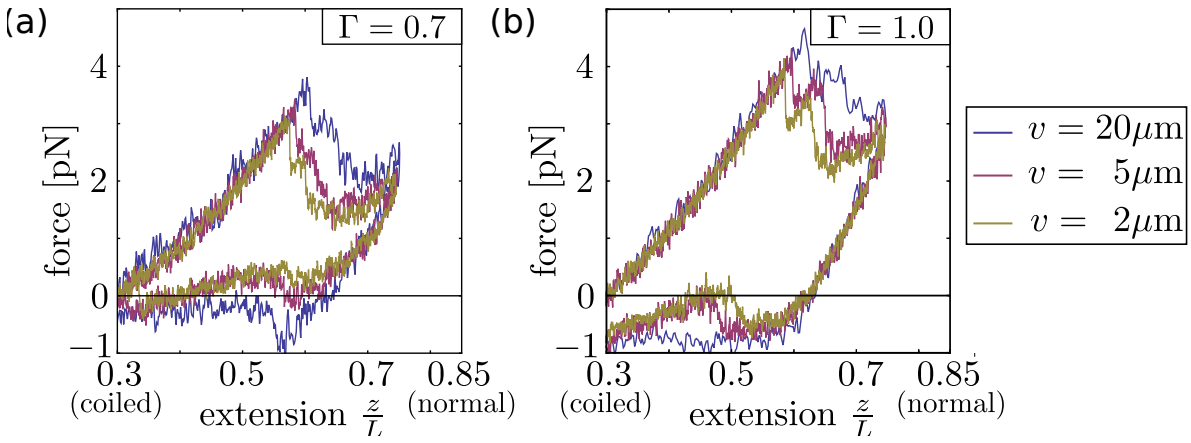

Abbildung 4.6: Force-extension curves for twist-to-bend ratios $\Gamma = 0.7$ **(a)** and $\Gamma = 1$ **(b)** at different extension rates $v_p = 2\mu\text{m/s}$, $5\mu\text{m/s}$ and $20\mu\text{m/s}$.

local curvature and torsion to overcome the potential barrier can be created at smaller extension. The curves in figure 4.6 just give one specific realization for each parameter set. In the following section, we will investigate in detail the probability distribution for the extension where the first coiled-to-normal transition occurs.

If the filament in the normal state is compressed too fast, it will start to buckle since again it has not sufficient time to overcome the energy barrier. This is visible in figure 4.6(a), where the filament with the highest compressing rate $v_p = 20\mu\text{m/s}$ buckles which corresponds to a negative force. On the other hand, for smaller rates v_p, the filament always returns into the coiled state.

4.4 Clamped filament

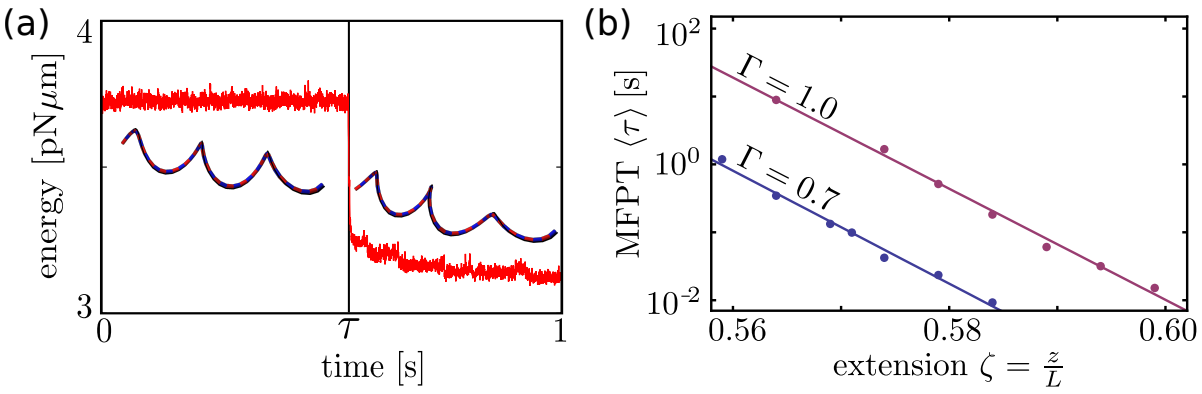

Abbildung 4.7: **(a)** When the local coiled-to-normal transition occurs, the energy decreases instantaneously. **(b)** Mean-first-passage time (MFPT) as a function of extension $\zeta = z/L$ for $\Gamma = 0.7$ and $\Gamma = 1.0$.

Since the bacterial flagellum goes through a sequence of equilibrium states during the measurements of the force-extension curves, it should be possible to derive some characteristics of these curves by investigating a clamped filament which is hold at a fixed extension $\zeta = z/L$ in thermal equilibrium. In particular, we show here how one can infer the mean extension $\langle\zeta\rangle\,(v_p)$, where the filament in a force-extension measurement undergoes the first local transition to the normal state, as a function of the extension rate v_p.

We stretch the filament in the coiled state at zero temperature to an extension $\zeta = z/L$ and keep this extension constant. We then perform a Brownian dynamics simulation and determine for each realization the first passage time τ at which a local transition to the normal state occurs. Figure 4.7(a) shows the filament before and after the transition accompanied by a sharp decrease of the elastic free energy. According to Kramers theory, the mean-first-passage time (MFPT) is proportional to the Arrhenius factor,

$$\langle\tau\rangle \sim \exp\left(\frac{\triangle\mathcal{F}(\zeta)}{k_B T}\right). \tag{4.17}$$

The activation energy $\triangle\mathcal{F}(\zeta)$ depends on the extension ζ and is needed to create the domain wall between the coiled and normal state. We determined the MFPT by averaging over 100 simulated values for τ at each extension ζ. The results are plotted in figure 4.7(b) for two twist-to-bend ratios $\Gamma = 0.7$ and $\Gamma = 1$. We only simulated $\langle\tau\rangle$ for a small variation in the extension for two reasons: at larger extensions where $\triangle\mathcal{F}(\zeta) \approx k_B T$ the Kramers theory is no longer valid and $\langle\tau\rangle$ is too small to be determined accurately;

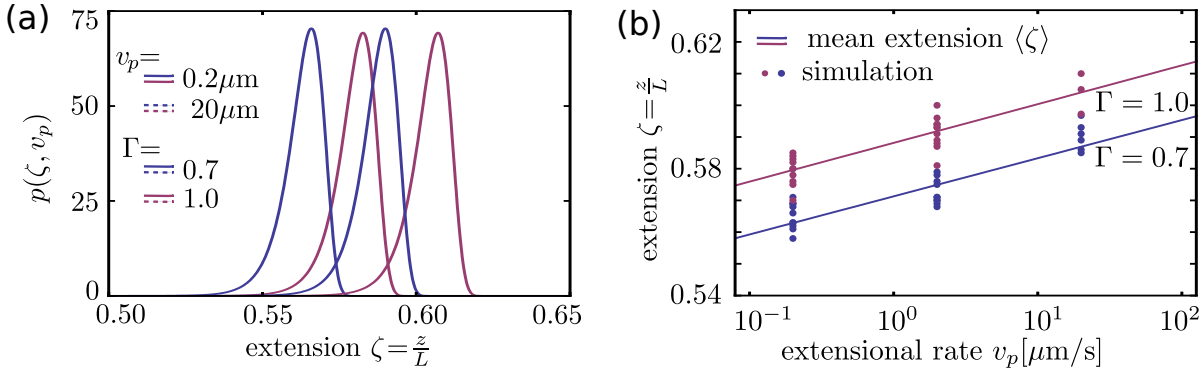

Abbildung 4.8: **(a)** Probability distributions $p(\zeta, v_p)$ as a function of extension ζ for $\Gamma = 0.7$ (blue) and $\Gamma = 1$ (magenta) at extension rates $v_p = 0.2\mu$m/s (full lines) and $v_p = 20\mu$m/s (dashed lines). **(b)** Analytically determined mean extension $\langle\zeta\rangle(v_p)$ for the coiled-to-normal transition as a function of velocity v_p for $\Gamma = 0.7$ (blue) and $\Gamma = 1$ (magenta). The dots indicate numerically determined extensions for each simulation run.

at smaller extensions $\langle\tau\rangle$ is so large that it cannot be calculated in reasonable simulation times. Note that for $\Gamma = 1$ the MFPT spans three decades. Our simulation results demonstrate that $\langle\tau\rangle(\zeta)$ can be fitted by an exponential

$$\log\langle\tau\rangle(\zeta) \approx \alpha - \beta\zeta, \tag{4.18}$$

where $\langle\tau\rangle$ is measured in seconds. Equation (4.18) can just be viewed as a Taylor expansion to linear order in ζ. The parameters α and β follow from a least-square fit. Whereas α changes with Γ, the slope β surprisingly does not seem to depend on Γ within the numerical accuracy. A similar law as Eq. (4.18) is used in situations where bonds rupture under a given load force [10, 35]. Note, however, that here we control the extension.

Within the adiabatic or quasistationary approximation, we now formulate the probability $p(t, v_p)\mathrm{d}t$ that within the time interval $[t, t + \mathrm{d}t]$ the filament transforms locally from the coiled to normal state when stretched with velocity v_p. This is a conditional probability that (I) the transition occurs in the time interval $\mathrm{d}t$ and (II) there was no transition until the time t. The first one is given by the inverse of the MFPT $\langle\tau\rangle(t)^{-1}\mathrm{d}t$ at time t. The second one is the product of the probability that there was no transition $(1 - \langle\tau\rangle(t_1)^{-1}\mathrm{d}t_1)$ at time t_1 for all times $t_1 < t$

$$\prod_{0<t_1<t}\left(1 - \frac{\mathrm{d}t_1}{\langle\tau\rangle(t_1)}\right) = \exp\left(-\int_0^t \frac{1}{\langle\tau\rangle(t_1)}\,\mathrm{d}t_1\right) \tag{4.19}$$

where we used $1 - \mathrm{d}t_1/\langle\tau\rangle \approx \exp(-\mathrm{d}t_1/\langle\tau\rangle)$. If we consider that the time dependence of the MFPT comes in by varying the extension $\zeta = z/L$ by

$$\zeta(t, v_p) = \zeta_0 + tv_p/L \tag{4.20a}$$

we obtain

$$p(t, v_p) = \frac{1}{\langle\tau\rangle\big(\zeta(t, v_p)\big)} \exp\left(-\int_0^t \frac{1}{\langle\tau\rangle\big(\zeta(t_1, v_p)\big)}\,\mathrm{d}t_1\right). \tag{4.20b}$$

Using Eq. (4.20a), we introduce the probability $p(\zeta, v_p)\mathrm{d}\zeta = p(t, v_p)\mathrm{d}t$ that the filament undergoes a local coiled-to-normal transition at extension ζ. To calculate it analytically we rewrite Eq. (4.18) in the form

$$\langle\tau\rangle = \tau_0 \exp[-\beta(\zeta - \zeta_0)]. \tag{4.21}$$

and assume its the validity for the whole ζ range. Now we introduce the rescaled extension variable $x = \beta(\zeta - \zeta_0) = \beta v_p t/L$ and calculate the probability $p(x)\mathrm{d}x = p(t)\mathrm{d}t$ by solving the integral in Eq. (4.20b) with the help of $\langle\tau\rangle = \tau_0 \exp(-x)$ and obtain

$$p(x)\mathrm{d}x = \mathrm{e}^{x-A} \exp\left(-\mathrm{e}^{-A}(\mathrm{e}^x - 1)\right)\mathrm{d}x, \tag{4.22}$$

where $\exp(-A) = L/(\beta v_p \tau_0)$. At $x = 0$ or $\zeta = \zeta_0$, the choice of our parameters shows that the energy barrier between coiled and normal state is much larger than $k_B T$, so $p(x = 0) = e^{-A}$ is almost zero or $A \gg 1$. Even for $x \approx 0$, we can therefore approximate the probability density in Eq. (4.22) as

$$p(x) \approx \mathrm{e}^{x-A} \exp\left(-\mathrm{e}^{x-A}\right) := p_0(x - A), \tag{4.23}$$

and therefore

$$p(\zeta, v_P) = \beta\, p_0\left(\beta(\zeta - \zeta_0) - \log\left(\frac{\beta v_p \tau_0}{L}\right)\right). \tag{4.24}$$

As discussed above the parameter β is constant for different twist-to-bend ratios. So the probability distributions are always the same but shifted due to the parameter A, e.g. different values of the extension rate v_p or Γ (which affects τ_0).

The results are plotted in figure 4.8(a) for $\Gamma = 0.7$ (blue) and $\Gamma = 1$ (magenta) and for extension rates $v_p = 0.2\mu\mathrm{m/s}$ (full lines) and $v_p = 20\mu\mathrm{m/s}$ (dashed lines). The probability distributions are concentrated on a small range about their maximum values and are shifted to larger extensions for increasing velocities v_p, as expected.

Now we calculate the mean extension

$$\langle\zeta\rangle\,(v_p) = \int_{\zeta_0}^{\infty} \zeta p(\zeta, v_p) d\zeta, \tag{4.25}$$

at which the coiled-normal transition occurs first for a given extension rate v_p. Therefore we first write the probability density of Eq. (4.23) as $p(x) = -\partial_x \exp\left(-\mathrm{e}^{x-A}\right)$ to derive the mean of the rescaled extension variable $\langle x\rangle$. After integrating by parts and substituting $y = -\exp(x - A)$ we arrive at the exponential integral function:

$$\langle x\rangle = -\exp(\mathrm{e}^{-A}) \int_{-\infty}^{-\mathrm{e}^{-A}} \frac{\mathrm{e}^y}{y}\mathrm{d}y, \tag{4.26}$$

which for $e^{-A} \ll 1$ is approximated by

$$\langle x \rangle \approx -(C + \log e^{-A}) = -C + A, \tag{4.27}$$

where $C = -\int_0^\infty e^{-x} \log x dx \approx 0.577$ is Euler's constant. Introducing the original extension variable ζ and $A = \log(v_p \tau_0 / L) + \log(\beta)$, we obtain for the mean extension at which the coiled-to-normal transition first takes place

$$\langle \zeta \rangle = \zeta_0 + \frac{1}{\beta}\Big(- C + \log(v_p \tau_0 / L) + \log(\beta)\Big). \tag{4.28}$$

In particular we have shown that the mean extension grows logarithmicly with the extension rate

$$\langle \zeta \rangle (v_p) \sim \log v_p. \tag{4.29}$$

The mean extension $\langle \zeta \rangle (v_p)$ with all prefactors and constant terms is plotted in figure 4.8(b) for $\Gamma = 0.7$ (blue) and $\Gamma = 1$ (magenta) together with numerically determined extensions ζ for several realizations at a specific velocity v_p. The values scatter around the mean value and are, therefore, in good agreement with the analytical treatment. We note that a relation similar to Eq. (4.29) occurs for the velocity dependence of the rupture force of single molecular bonds in dynamic force spectroscopy [35].

4.5 Summary and conclusions

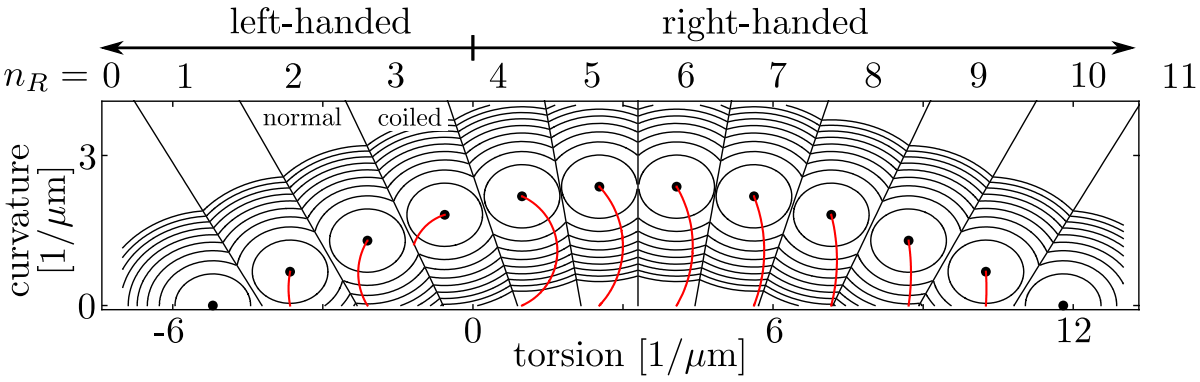

Abbildung 4.9: Contour lines of the free energy density of the extended Kirchhoff rod theory that includes all 12 polymorphic states of the bacterial flagellum. For all helical states the same ground state energy and the same bending and torsional rigidity with $\Gamma = 0.7$ is assumed. The red lines indicate the paths of uniformly stretched flagella.

In this chapter we have developed a sufficiently simple elastic model to describe the polymorphism of a bacterial flagellum based on Kirchhoff's theory of an elastic rod. The friction with the aqueous environment is modeled within resistive force theory. Using geometrical parameters of the coiled and normal states and the bending rigidity as obtained in reference [28], we are able to reproduce the force-extension curves recorded in experiments. Thermal fluctuations realized within Brownian dynamics simulations are crucial. In particular, the force values at which a first coiled-to-normal transition takes place lie between 3 and 5 pN, as in experiments [28]. We have investigated in detail how the force-extension curve depends on the twist-to-bend ratio Γ and, furthermore, by analytic arguments identified a parameter region for ground-state energy difference δ and Γ, where a coiled-to-normal transition should be observable. It clearly demonstrates that for values of Γ well above one, a polymorphic transformation is not possible and therefore contradicts some of the experimental values for Γ recorded in literature. Based on our simulations, we predict Γ to be within 0.7 and 1.0. Further studies demonstrate how the extensional rate v_p influences the force extension curve. We directly observe the influence in the simulations of the full force-extension cycle but also when we concentrate on the extension for the first coiled-to-normal transition. Since the extensional rates v_p are sufficiently small, the flagellum goes through a sequence of quasi-stationary states. We, therefore, used equilibrium properties of clamped flagella to predict a logarithmic velocity dependence for the mean extension of the first coiled-to-normal transition in good agreement with our simulations.

Our approach is easily extended to include more than two polymorphic states. Figure 4.9 shows the contour lines of the resulting free energy landscape when all twelve polymorphic conformations of the Calladine model of the bacterial flagella are taken into account. For each of these conformations we take Kirchhoff's elastic free energy with spontaneous curvature and torsion as given by Calladine [19] and just consider the minimum value from all these free energies. We assume here that the ground-state energies of all helical states are zero and that they all have the same bending and torsional rigidities with $\Gamma = 0.7$. We also included the paths of uniformly stretched helical filaments. The coiled-to-normal transition ($n_R = 3$ to 2) takes place with certainty. However, all the other transitions would need thermal fluctuations to occur. For example, the normal-to-hyperextended transition ($n_R = 2$ to 1) will only occur when it is stretched sufficiently slowly so that thermal fluctuations can induce the transformation.

We can now use our model to study various aspects connected to bacterial locomotion. Hence we will investigate how polymorphic transitions are induced by rotating the flagellum in the next chapter.

Kapitel 5

Rotation-induced polymorphic transformations

5.1 Introduction

In this chapter we apply our model of the polymorphism of bacterial flagella, which we have developed and compared with experiments in the previous chapter, to the rotation-induced transformations, which occur for example during the tumbling of *E. coli*.

As far as we know, there exists only one study, which was carried out by Arkhipov *et al.* [2] that directly addresses the rotation-induced transformation between polymorphic states. It is based on coarse-grained molecular dynamics simulations. Nevertheless these simulations only consider a small segment of the flagellar filament with a length below one micron for a few microseconds. Watari and Larson [129] investigated the swimming of bacteria during the switch from run to tumble. The transformations between the polymorphic states, e. g. from normal to semicoiled and finally to curly I, were mimicked by changing the equilibrium configuration of the helical form, e. g. the intrinsic curvature and torsion, during the simulations. Lobaton and Bayen [82, 83] studied swimming of a single flagellated bacterium called *Rhodobacter sphaeroides*. They described the flagellar filament with an elastic network. They used four different spring constants within the network which were optimized to describe two helical states of the flagellum, that appear in a low- and a high-torque regime, respectively.

Our challenging goal is to model the tumbling of *E.coli* or *Salmonella* which includes a rotation-induced transition between four different helical states, namely the normal, coiled, semicoiled, and curly I form. In particular, this involves a switch from a right-handed to a left-handed helix. We start our study of the rotation-induced polymorphic transformations with a minimal model that involves a spherical cell body and one flagellum with two relevant polymorphic states. We use the bacterium *Rhodobacter sphaeroides* as biological motivation for our minimal model. In contrast to the run-and-tumble strategy of *E. coli* it follows a run-and-stop strategy to perform chemotaxis. During swimming, the flagellum of *Rhodobacter* has a similar form as the normal form of *E. coli*, which is optimized for propelling the bacterium forward. After a while the bacterium stops rotation of the motor and the flagellum relaxes into a coiled state. When the motor is

switched on again, the flagellum returns into the normal state and the bacterium swims to a new, random direction.

In section 5.2 we will first discuss the swimming behavior of *Rhodobacter*. Then we will present our model of this bacterium and discuss the rotation-induced transition between the two polymorphic states in detail. Finally we will show how the coiled-to-normal transition contributes to the random reorientation of the cell during the run-and-stop strategy. Subsequently we will demonstrate in section 5.3 how our model has to be extended to describe the transformation between several polymorphic forms as observed during the tumbling motion of *E. coli*.

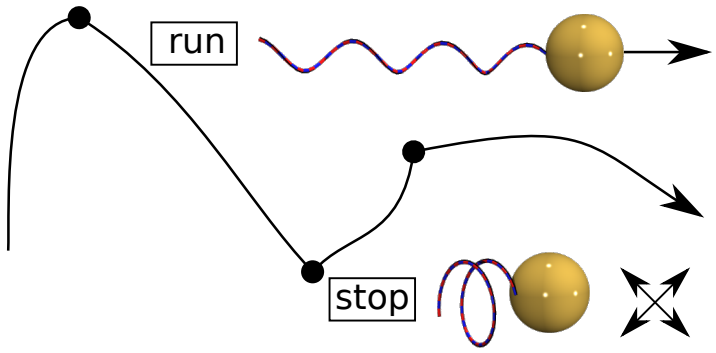

Abbildung 5.1: *Rhodobacter* uses for chemotaxis a run-and-stop strategy which is the analogue of the run-and-tumble strategy of bacteria like *E. coli*. During a run the flagellum is in a normal state optimized for swimming. When flagellar rotation stops the filament relaxes into an open coiled form. After a while the flagellum statrts to rotate again and the normal helix reforms such that the bacterium swims into a new direction.

5.2 Swimming of Rhodobacter sphaeroides

5.2.1 Biology of Rhodobacter sphaeroides

Rhodobacter sphaeroides is a purple bacterium which produces energy through photosynthesis and is living in freshwater. It is in many ways different compared to peritrichous bacteria like *E. coli* or *Salmonella*. It has an oblate but nearly spherical cell body with only one flagellum. Exceptions are dividing bacteria which have two flagella that act independently, e. g. without forming a bundle [3]. The cell swims with an average speed of 35µm/s [5] and reaches a maximal speed of up to 80µm/s [3] which is much faster than the typical speed of *E. coli*. It stops intermittently typically every 10s and restarts after a short interval of typically about 1s, but both times have a wide variation [3]. Due to this run-and-stop strategy they change their swimming direction, which is essential during a chemo- or phototactic response, but it is less pronounced compared to the reorientation during tumbling of peritrichous bacteria [3, 108]. Also accelerating and decelerating motion of *Rhodobacter* and apparent changes in the swimming direction without a pronounced stop or pause is observed [5].

The flagellum is comparable to the normal form of the flagellum of *E. colis* during the swimming but it is right-handed and rotates clockwise. It has a pitch of 2.2µm and a helical diameter of 0.7µm, which corresponds to a curvature of $\kappa_0 = 1.4/\mu m$ and a torsion of $\tau_0 = 1.4/\mu m$ [3].

After the flagellar rotation has stopped, the filament undergoes a polymorphic transition relaxing from the distal end into a coiled form. When rotation starts again, the normal helix reforms starting from the cell body towards the distal end [3]. In contrast

to the coiled form of *E. coli*, which we have studied in chapter 4, the coiled form of *Rhodobacter* resembles a rope lasso like structure. Therefore it is also referred to as "open coil" [108]. It has a diameter of 2.1μm and a small pitch which is not given in literature. Therefore we use as curvature $\kappa_0 = 0.95/\mu\text{m}$ and assume for the torsion $\tau_0 = 0.1/\mu\text{m}$. In figure 5.1 we sketch the swimming trajectory of *Rhodobacter* and the helical forms in the run and stop phase. We note that reference [38] gives other values for the geometrical parameters of the coiled and the normal form which we will discuss later. In addition, there exists also a flagellar form which is straight or a helix with very small radius that appears for very fast rotations [4, 108].

In section 2.1 we discussed in vitro experiments with detached bacterial flagella where different polymorphic states could be induced by changing the solvent conditions. Similar experiments were done with the *Rhodobacter* flagellum, where the coiled form is dominant under physiological conditions. Other forms, e. g. the normal one, are obtained by reducing the pH value. Noteworthy, the range of forms obtained for the *Rhodobacter* filament are different from the forms of *E. coli* or *Salmonella* [108].

5.2.2 Modeling the polymorphic states and swimming of Rhodobacter sphaeroides

To model the bacterium we assume a spherical cell body with radius $a = 1\mu\text{m}$ at the position $\boldsymbol{r}_B$. We attach the flagellum at one point on the surface of the sphere $\boldsymbol{r}_B + a\boldsymbol{e}$ with the normalized orientation vector $\boldsymbol{e}$. For the coupling of the cell body with the flagellum we use again our coarse-grained hook model, i. e. hinged boundary conditions for the attached end of the flagellum. The first point of the filament moves with the point on the sphere where it is attached. We drive the filament with a motor torque $M \geqq 0$ which is parallel to the orientation vector $\boldsymbol{e}$. It acts on the flagellum with $\boldsymbol{M} = -M\boldsymbol{e}$ so that it rotates clockwise (if seen from behind). The opposed torque $-\boldsymbol{M}$ acts on the cell body such that it rotates counterclockwise.

The spherical cell body moves with a velocity $\boldsymbol{v}$ due to the force of the flagellum $\boldsymbol{F}$ and rotates with angular velocity $\boldsymbol{\omega}$ due to the motor torque and the force-induced torque,

$$\gamma_T \boldsymbol{v} = \boldsymbol{F} \qquad \text{and} \qquad \gamma_R \boldsymbol{\omega} = M\boldsymbol{e} + a\boldsymbol{e} \times \boldsymbol{F}, \tag{5.1}$$

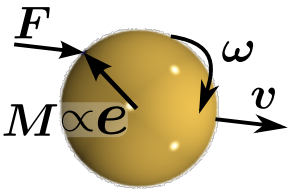

Abbildung 5.2: Motion of the cell body

with the translational and rotational friction coefficients $\gamma_T = 6\pi\eta a$ and $\gamma_R = 8\pi\eta a^3$ as shown in figure 5.2. To avoid an overlap of the filament with the cell body, we use the repulsive part of a Lennard-Jones potential $U = F_0 a \frac{1}{12} \left(\frac{a}{r^{(n)}}\right)^{12}$ with the distance $r^{(n)} = |\boldsymbol{r}^{(n)} - \boldsymbol{r}_B|$ of a point of the filament $\boldsymbol{r}^{(n)}$ to center of the cell body $\boldsymbol{r}_B$. This interaction force also enters Eq. (5.1). We choose at the surface of the cell body the force $F_0 = 1\text{pN}$ comparable to the typical thrust force.

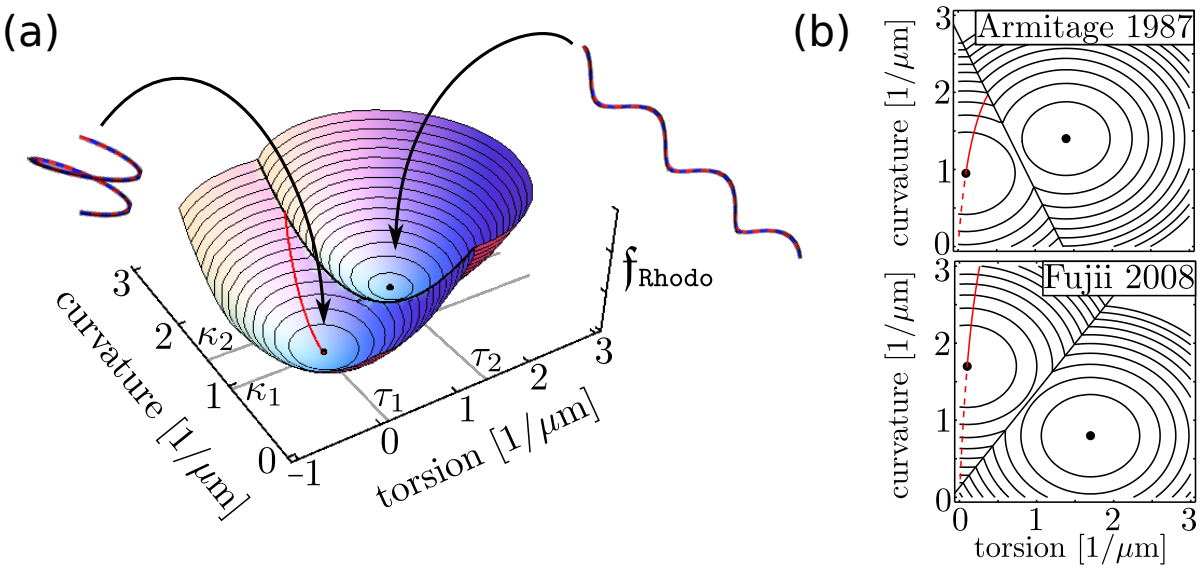

Abbildung 5.3: **(a)** Free elastic energy density of the flagellum of *Rhodobacter* as function of curvature κ and torsion τ using $\mathbf{\Omega} = (0, \kappa, \tau)$. The open coiled (left) and normal (right) form of the flagellum are sketched. The red line indicates the uniform deformation of a helical spring due to a torque applied parallel to the helical axis. **(b)** Comparison of the energy density for the flagellum geometry of references [3] (Armitage 1987) and [38] (Fujii 2008). In the Armitage geometry a deformation of the coiled form due to a torque engenders a transition to the normal form whereas in the Fujii geometry a transition is not possible. Therefore we use the Armitage geometry.

To model the two polymorphic states, i. e. the normal and the (open) coiled filament, we use our extended elastic free energy (4.4) and (4.5) introduced in section 4.2.3 with the intrinsic curvature and torsion derived from reference [3]. We show the resulting energy density $\mathfrak{f}_{\mathtt{poly}}(\mathbf{\Omega}, \mathbf{\Omega}_1, \mathbf{\Omega}_2)$ in figure 5.3(a) for $\Omega_1 = 0$ as a function of curvature $\Omega_2 = \kappa$ and torsion $\Omega_3 = \tau$. The red line indicates the uniform deformation of a helical spring due to an applied torque along the helical axis as described in section 2.5.2. We use it as a rough approximation for the deformation of the filament due to the applied motor torque. Figure 5.3(b) shows equipotential lines of the energy for the used flagellum geometry published by Armitage and Macnab 1987 [3] and for the flagellum geometry published by Fujii *et al.* [38] mentioned above. In the Armitage geometry a deformation of the coiled form due to a torque engenders a transition to the normal form, which can be seen from the red curve indicating the path of uniform deformation. In the Fujii geometry a transition due to uniform deformation is not possible, which we also verified by simulations. Therefore we use always the geometry given by Armitage [3] in our simulations.

For the elastic properties of the *Rhodobacter* flagellum we did not find details in

literature. It is only stated that the open coils and the normal forms are faint and highly susceptible to Brownian motion [108]. This could be a hint that its bending rigidity is smaller than the one of a *E. coli* flagellum. Nevertheless we assume for comparability within this work the same bending rigidity $A = 3.5\text{pN}\mu\text{m}^2$ as before.

5.2.3 Dynamics of the coiled-to-normal and normal-to-coiled transition

In chapter 4 we learned that thermal noise is important for the flagellum to cross the energy barrier between two polymorphic forms and so to undergo a polymorphic transformation. So we performed Brownian dynamics simulations of our motor driven model bacterium. We start with a relaxed flagellum in the coiled state and immediately turn on the motor torque to a maximal value of $M_{\mathtt{max}} = 4.5\text{pN}\mu\text{m}$. Straightaway we observe a transition into the normal state like in the experiments and our model bacterium starts to swim. When we reduce the torque to zero the bacterium stops and the filament relaxes slowly into the coiled state. We describe the details of the dynamics of the two transitions in more detail below.

In figure 5.4(a) we show some snap shots of the angular strain vector $\mathbf{\Omega}$ along the filament in the free energy landscape projected to the Ω_2-Ω_3-plane corresponding to curvature and torsion, respectively, for $\Omega_1 = 0$. Each point corresponds to a discretized segment of the filament with the length $h = 0.2\mu\text{m}$. In section 4.3.2 we derived the form of the energy barrier in this plane (see Eq. (4.13)). We use it as boundary between the two polymorphic states to determine the actual configuration of the filament from the rotational strain for every point along the filament (given in arc length) and time. We plot this configuration color coded in white and gray for the open coiled and normal state, respectively, in figure 5.4(b). In the same graph we plot the applied motor torque as a function of time in blue.

After we turn on the motor torque at time $t = 0\text{ms}$ the filament switches from the open coiled into the normal state. This transition starts at the end which is attached to the cell body and it takes around 25ms to transform 90% of the filament into the normal form. This time is consistent with the characteristic time scale τ_c for the diffusion of the twist given in section 2.5.4. We obtain $\tau_c \sim 40\text{ms}$ for the open coiled and $\tau_c \sim 8\text{ms}$ for the normal form. The large difference appears due to the radial dependence of $\tau_c \propto R^2$ and the small radius of the normal form.

We show in figure 5.4(c) snapshots of our model bacterium with the filament configuration during the coiled-to-normal transition. At 5ms a small part of around 10% of the filament at the end attached to the cell body is in the normal state. Most parts of the filament remain in the coiled form which is deformed spiral-like. This is confirmed by the snapshot of the rotational strain along the filament shown in figure 5.4(a)(i), where most of the points group around the red line indicating the deformation due to the torque parallel to the helical axis. During the transition from coiled to normal, the

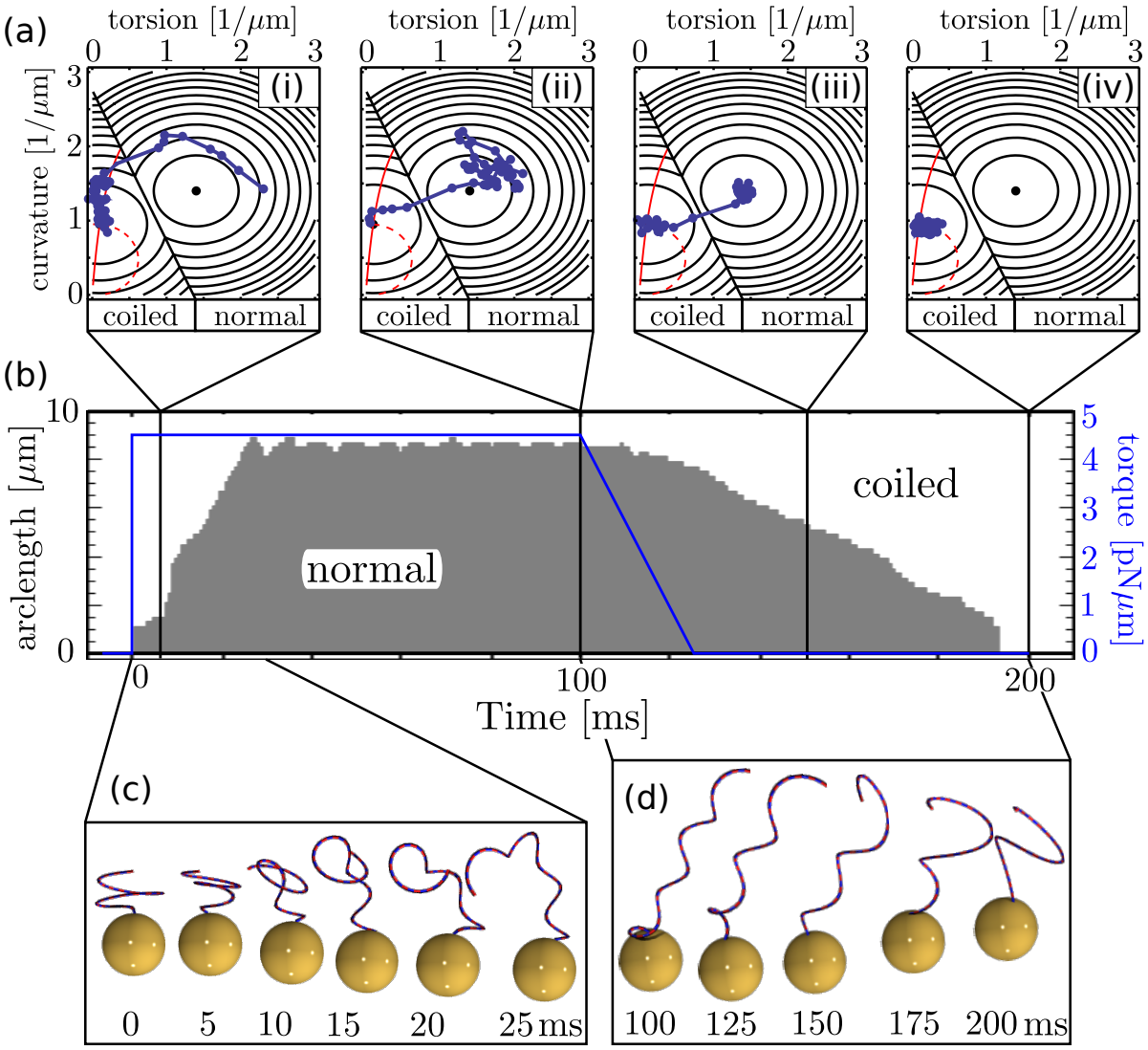

Abbildung 5.4: **(a)** Snapshots of the Ω_2 and Ω_3 components of the rotational strain vector along the filament in the energy landscape after times (i) 5ms, (ii) 100ms, (iii) 150ms, and (iv) 200ms. The continuous and the dotted red lines indicate the path of a uniformly deformed helix due to a torque or a force, respectively. **(b)** Time evolution of the applied motor torque (blue line) and the actual polymorphic state at a certain arc length (white: coiled state, gray: normal state). **(c)** Snapshots of the filament during the coiled-to-normal transition. **(d)** Snapshots of the filament during the normal-to-coiled transition.

height of the corresponding undeformed helix $L_0 = \sin\alpha L$ changes from 1μm to 7μm. As a consequence there is a large stress during the coiled-to-normal transition between the parts of the filament that are in different states. Comparing the spring constants (see Eq. (2.88b)) of the two polymorphic forms, we recognize that the normal filament is much stiffer than the open coiled state, again because of the smaller helical radius. As a consequence the part in the normal state assumes its equilibrium length and therefore compresses the coiled part, as can be seen in the snap shots of the filament in figure 5.4(c) at times $t = 10$ms and $t = 15$ms. The final transition to the normal state of the deformed end leads to an overall bent filament as shown for times $t = 20$ms and $t = 25$ms. In the next section we point out, that the bent configuration plays an important role in the reorientation of the cell during the run-and-stop strategy.

In figure 5.4(d) we show snapshots of our model bacterium with the filament configuration during the normal-to-coiled transition. In figure 5.4(a)(ii) the rotational strain along the filament before reducing the motor torque is illustrated. 90% of the filament are in the normal state. However, because there is no torque at the free end, which leads to a deformation, it remains in the coiled state. Nevertheless, it is difficult to detect the coiled vestige in the helix as shown in 5.4(d) for $t = 100$ms.

We reduce the motor torque within 25ms to zero and therefore the rotational strain relaxes into the two local minima of the coiled and the normal form [see figure 5.4(a)(iii)]. Due to the energy difference δ between both states, it relaxes slowly into the coiled state with lower energy as can be seen for times $t = 150$ms and $t = 175$ms. Finally, the whole filament switches into the coiled state. We note that during the normal-to-coiled transition the cell body is pulled backwards due to the change of the height of the helical state.

Torque and length dependence of the coiled-to-normal transition

Until now we assumed a torque which is large enough to induce a coiled-to-normal transition. Now we investigate the necessary torque for such a transition and compare the results for two different filament lengths.

In chapter 4 we have derived the position of the energy barrier between two polymorphic states (see Eq. (4.13)). We use this result to estimate the torque required to deform the coiled filament such that it crosses the barrier and a transition to the normal form is induced. Therefore we use the absolute value $M(\mathbf{\Omega})$ of the constitutive equation (2.44) assuming zero twist angle and identify $\Omega_2 = \kappa$ with the curvature and $\Omega_3 = \tau$ with the torsion

$$M = A\sqrt{(\kappa - \kappa_1)^2 + \Gamma^2(\tau - \tau_1)^2}. \tag{5.2}$$

Here we used the intrinsic curvature κ_1 and torsion τ_1 of the coiled form, the bending rigidity A and the twist-to-bend ratio Γ.

Along the energy barrier we detect two characteristic points: first, the minimum of the energy barrier, where we obtain $M_{\mathtt{min}} \approx 1.5$pNμm for the chosen geometry and elastic parameters, second, the intersection of the energy barrier with the approximate solution

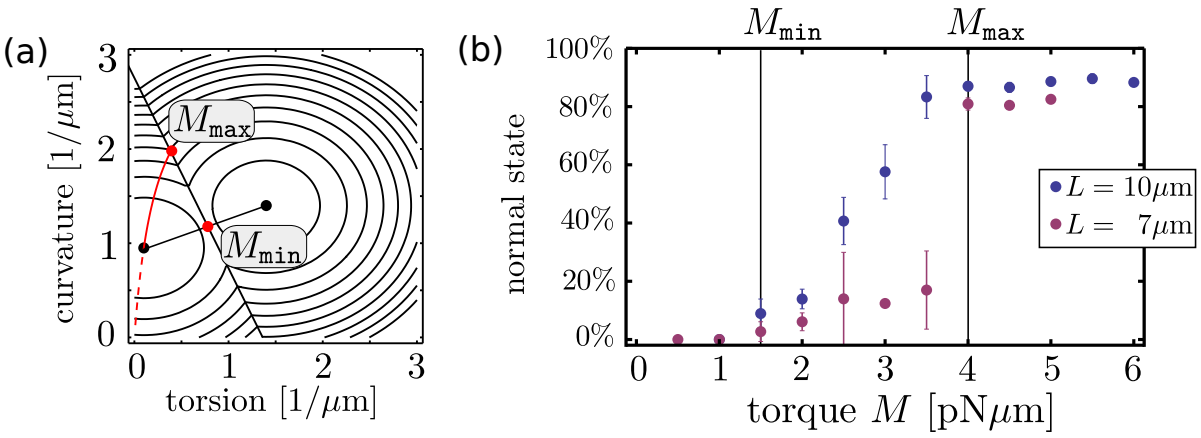

Abbildung 5.5: **(a)** The positions in the energy landscape, where we derived the characteristic torques $M_{\mathtt{min}}$ and $M_{\mathtt{max}}$, is indicated by the red dots. **(b)** The fraction of the filament that switches into the normal state as a function of the applied motor torque for a filament length of $L = 7\mu$m and $L = 10\mu$m. The dots correspond to the mean value of twenty realizations 50ms after the motor torque reached its maximum. The error bars indicate the standard deviation.

of a uniformly deformed helix for which we obtain $M_{\mathtt{max}} \approx 4$pNμm. The positions in the energy landscape of the points where we determined $M_{\mathtt{min}}$ and $M_{\mathtt{max}}$, are indicated in figure 5.5(a). We do not expect a transition for torques M smaller than $M_{\mathtt{min}}$, because the energy barrier is too large. For an intermediate torque $M_{\mathtt{min}} < M < M_{\mathtt{max}}$, we deform the filament such that small thermal fluctuations may help to cross the energy barrier. When we choose a torque larger than $M_{\mathtt{max}}$, the approximate uniformly deformed helix crosses the energy barrier and therefore we expect a fast transition.

To test our prediction, we perform the same simulations as before and determine the fraction of the filament which has switched into the normal state 50ms after the motor torque has reached its maximum. We note, this is twice the time we have obtained before for a coiled-to-normal transition to take place. We present the data in figure 5.5(b) for a short filament of $L = 7\mu$m and a long filament of $L = 10\mu$m. The dots correspond to an average over twenty different realizations, whereas the error bars indicate the standard deviation. When the deviation between the different realizations is smaller than the point size, no error bar is shown.

We observe three different regimes. For small torques $M < M_{\mathtt{min}}$ we never find a transition even if we wait for a very long time, i. e. up to 500ms. For the intermediate regime, $M_{\mathtt{min}} < M < M_{\mathtt{max}}$, we observe a partial transition of the filament into the normal state which always starts from the tip. We observe a remarkable difference between the short and the long filament. In the short filament only the tip switches into the normal

state also if we wait for very long times. In contrast, for the long filament a larger fraction of the filament switches within the first 50ms into the normal state as could be seen in figure 5.5. If we wait longer than 50ms we observe for a torque larger than $M \approx 2.5\text{pN}\mu\text{m}$ a complete transition of the filament (which means that only the last 10% remains in the coiled state, data not shown). For large torques $M > M_{\mathtt{max}}$ we observe a third regime where the coiled-to-normal transition occurs immediately as described before.

5.2.4 Changing the swimming direction with the run-and-stop strategy

Dynamics of the reorientation

Rhodobacter and *E. coli* perform a random walk which is important for a chemotactic response. *E. coli* randomly changes the direction by switching the rotational direction of one of its motors. Therefore the filament, which is attached to this motor, leaves the bundle of rotating flagella and the cell is reoriented to a new random direction. For *Rhodobacter* with only one flagellum and motor this strategy is not possible. Switching the rotational direction of the motor will only rotate the cell body and the flagellum in the opposite direction as before so that the bacterium would swim backward. Therefore *Rhodobacter* uses a different strategy to obtain a reorienting torque by rotating the flagellum in a way such that it creates a force parallel to the surface of the cell. As discussed before, after the coiled-to-normal transition the flagellum is bent. The relaxation to a straight helix and the rotation-induced thrust force of the bent filament produces such a force that reorients the cell. We discuss now that this is the main contribution for the reorientation of the bacterium during the run-and-stop strategy.

During the normal-to-coiled transition we do not observe a pronounced change of the orientation of the cell. This transition needs a relative long time such that the motor torque is most of the time zero. Hence during the relaxation to the coiled state only elastic forces act. These forces appear due to the change of height of the helix from the normal to the coiled form and act more or less perpendicular to the surface of the cell. Hence they do not contribute to a reorientation.

To analyze the reorientation during the coiled-to-normal transition, we perform a simulation, starting in the coiled state with zero torque and let the cell diffuse. We start the motor torque by increasing it linearly from zero to $M = 4.5\text{pN}\mu\text{m}$ within 10ms, in agreement with the observed switching times in other bacteria [12, 122]. In figure 5.6 we show in (a) the time behavior of the coiled-to-normal transition and the applied motor torque, in (b) the trajectory of the cell body, and in (c) the trajectory of the tip of the orientation vector $\boldsymbol{e}$, which is parallel to the applied torque, projected on the unit sphere. We distinguish five different phases in the dynamics which we color coded in the trajectories. In the beginning (i) we observe only diffusion, shown in red, which does not contribute significantly to the reorientation due to the small rotational diffusion constant $D_R \sim 0.16/\text{s}$ of the cell body. Then the motor torque is increased linearly in phase (ii),

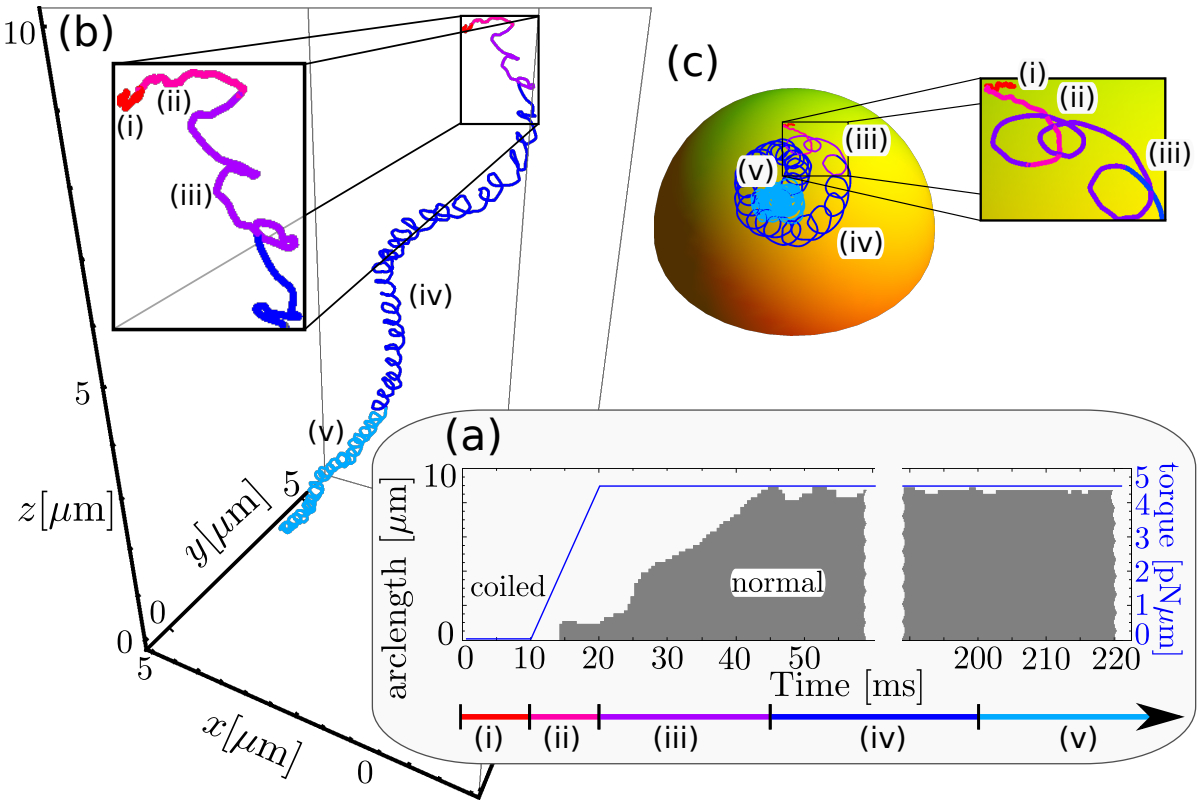

Abbildung 5.6: **(a)** Time evolution of the applied motor torque (blue line) and the actual polymorphic state (white: coiled state, gray: normal state), **(b)** Trajectory of the swimming model bacterium, **(c)** Trajectory of the orientation of the model bacterium. The five different phases of locomotion are indicated by colors: (i) translational and rotational diffusion, (ii) increasing the motor torque, (iii) coiled-to-normal transition of the flagellum, (iv) reorientation, and (v) straight swimming.

shown in magenta. When the coiled flagellum with its large radius starts to rotate the cell is slightly reoriented. In this phase only a small fraction of the filament switches into the normal state. After reaching the maximum torque the full transition occurs corresponding to phase (iii), shown in purple. Here the cell starts to translate, driven by the expanding normal filament. As mentioned before, at the end of this phase, when the filament is almost in the normal state, the helix is bent (see figure 5.4(c) at 25ms). During phase (iv), shown in deep blue, this bent configuration relaxes to a straight normal form which lasts around 150ms. In this phase the bacterium swims on a bent trajectory. Also the main part of the reorientation occurs in this time. Subsequently in the last phase (v), shown in light blue, the bacterium swims straight and no significant change of the mean orientation is observed.

We note that the trajectory in phase (v) is a helix with a radius of $\sim 0.1\mu$m and also the orientation vector rotates on a small circle. This is due to the relative large helical radius (0.35μm) of the normal filament. In our simulations the filament is attached at its end such that it does not rotate directly about the helical axis. This leads to a force perpendicular to the helical axis rotating with the filament. Helical trajectories are also known for magnetotactic bacteria [93]. For *Rhodobacter* helical trajectories have not reported yet, maybe due to low resolution or because the helical radius is smoothed out by the finite size of the hook.

The mean reorientation

Now we analyze the strength of the reorientation of the cell during the coiled-to-normal transition. Therefore we repeat the simulation described before and determine the swimming direction of the cell in phase (v). The cell starts with the initial orientation $\boldsymbol{e}_0$ at the beginning of the simulation, i. e. before the motor torque is switched on. As discussed before, phase (v) of swimming straight is reached about 150ms after the motor torque reached its maximum. Therefore we determine at this time the swimming direction. Since the bacterium swims on a helical trajectory we use the time average over one helical turn of the orientation vector $\boldsymbol{e}$ to obtain the actual normalized swimming direction $\boldsymbol{e}_s$. We introduce the reorientation angle $\cos\varphi = \boldsymbol{e}_s \cdot \boldsymbol{e}_0$ as the angle between the actual swimming direction and the initial orientation $\boldsymbol{e}_0$.

First we calculate the mean swimming orientation $\langle \boldsymbol{e}_s \rangle$ as the ensemble average of different realizations of our simulation starting with the same initial condition. This vector contains the information of the reorientation angle

$$\cos\overline{\varphi} := \langle \cos\varphi \rangle = \langle \boldsymbol{e}_s \rangle \cdot \boldsymbol{e}_0. \tag{5.3}$$

We note, in our simulations we always choose the same initial condition, e. g. the flagellum always has the same relative position to the cell body. Therefore the mean swimming orientation is in general not parallel to the initial orientation. In contrast in experiments the initial condition is randomly distributed. Therefore $\langle \boldsymbol{e}_s \rangle$ would be parallel to the initial orientation due to symmetry reasons. Nevertheless the reorientation angle φ and

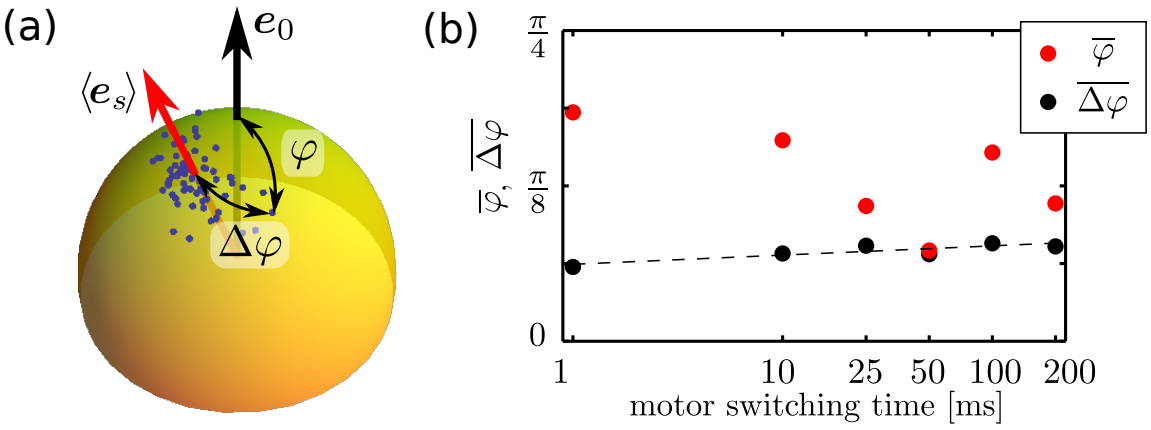

Abbildung 5.7: **(a)** The reorientation distribution for a motor switching time of 10ms. The initial orientation is given by the black arrow. The red one gives the average orientation of 100 different realizations (blue dots). **(b)** The average reorientation angle and the deviation from the mean orientation as function of the motor switching time.

its mean $\overline{\varphi}$ are the same and hence could be used for comparison between experiments and simulations.

We use the direction of the mean orientation $\langle \boldsymbol{e}_s \rangle$ to measure the strength of the stochastic effects, induced by fluctuations of the filament due to Brownian motion during the coiled-to-normal transition. Therefore we introduce the angle between the actual swimming direction and the mean orientation $\cos \Delta\varphi = \boldsymbol{e}_s \cdot \langle \boldsymbol{e}_s \rangle / |\langle \boldsymbol{e}_s \rangle|$. Again we calculate the mean of this quantity by an ensemble average

$$\cos \overline{\Delta\varphi} := \langle \cos \Delta\varphi \rangle = |\langle \boldsymbol{e}_s \rangle|. \tag{5.4}$$

In figure 5.7(a) we show the tip of the swimming orientation $\boldsymbol{e}_s$ on the unit sphere for 100 realizations (blue dots). The black arrow points in the direction of the initial orientation $\boldsymbol{e}_0$ and the red one in the direction of the mean swimming orientation $\langle \boldsymbol{e}_s \rangle$. In figure 5.7(b) we study the influence of the switching time of the motor torque, which is the time where the torque is linearly increased from zero to its maximum value, on the mean orientation angle $\overline{\varphi}$ and the mean deviation from the new swimming direction $\overline{\Delta\varphi}$.

For the mean orientation angle $\overline{\varphi}$ we find a maximum of around $\overline{\varphi} \sim 33°$ at small motor switching times of one microsecond. We observe reorientations up to an angle of $\varphi \sim 45°$. In this case the change of the motor torque is faster than the coiled-to-normal transition. Therefore we obtain a pronounced bending of the normal filament directly after the transition which leads to the strong reorientation discussed before (see figure 5.6). When we increase the motor switching time, the mean orientation angle

decreases to a minimum when the switching time is comparable with the coiled-to-normal transition time or the relaxation time of the coiled filament. As a consequence the bending of the normal state is less pronounced at the end of the transition. Especially for a motor switching time of 50ms the mean orientation $\langle \boldsymbol{e}_s \rangle$ is nearly parallel to the initial orientation $\boldsymbol{e}_0$ and so the mean orientation angle $\overline{\varphi}$ and the mean deviation from the new swimming direction $\overline{\Delta\varphi}$ are equal. For large motor switching times, the mean orientation angle $\overline{\varphi}$ increases again because of three contributions to the reorientation. First, the coiled state rotates slowly, which leads to a small reorientation, similar to observations in experiments [4]. Second, a partial transition into the normal state occurs, which is typical for slow motor torques. Third we find a full transition which results in a slightly bent normal state.

We find a deviation from the new swimming direction of $\overline{\Delta\varphi} \sim 10^\circ \ldots 15^\circ$. The growth of $\overline{\Delta\varphi}$ fits well to a logarithmic increase of the motor switching time. In chapter 4 we described how a force or, in our case, the torque drives the filament near the boundary between coiled and normal state where thermal fluctuations help to cross the energy barrier. As a consequence the time when a transition occurs fluctuates. We conclude that the main part of $\overline{\Delta\varphi}$ is determined by the fluctuations within the coiled-to-normal transition.

5.2.5 Summary and conclusion

In this section we modeled the bacterium *Rhodobacter sphaeroides* which serves as a minimal model to study the rotation-induced transition between two polymorphic states of a bacterial flagellum during swimming. Without an applied torque the filament is always in an open coiled state with small pitch and large radius. When we apply a sufficiently large torque, the filament undergoes a coiled-to-normal transition starting from the end attached to the motor. After decreasing the torque to zero, the filament relaxes slowly back into the coiled state starting from its free end, which is comparable to observations in experiments.

We identified two critical values of the applied torque: $M_{\mathtt{min}}$ is the minimal torque, which is necessary to cross the energy barrier and $M_{\mathtt{max}}$ is the torque, which leads for a uniform deformation to a coiled-to-normal transition. Below $M_{\mathtt{min}}$ no transition occurs at all. For torques between $M_{\mathtt{min}}$ and $M_{\mathtt{max}}$ we observe a partial coiled-to-normal transition strongly influenced by thermal fluctuations. If the applied torque is larger than $M_{\mathtt{max}}$, we find a fast coiled-to-normal transition comparable to the one observed in experiments.

During the transition from the coiled to the normal form of the flagellum, the helical height changes by a factor of seven. At the end of the coiled-to-normal transition the filament is strongly bent, since the transition is faster than the relaxation time of the filament. Due to the relaxation to a straight helix, the cell changes its swimming direction significantly. This reorientation is important for chemotaxis of *Rhodobacter sphaeroides*. Hence the run-and-stop strategy replaces the run-and-tumble strategy of bacteria like *E. coli* and *Salmonella*.

5.3 Rotation-induced polymorphic transformations in Escherichia coli

Peritrichous bacteria, such as *Escherichia coli* and *Salmonella typhimurium* propel themselves by rotating a bundle of flagella. When the sense of rotation of a flagellum is reversed, it leaves the bundle and undergoes a sequence of different polymorphic forms. During the flagellar polymorphism, the bacterium tumbles and then continues swimming in a different direction, which is a crucial point for chemotaxis. In this section we demonstrate that our elastic model of the polymorphic forms of the bacterial flagellum describes the transformations observed during the tumbling of *E. coli*.

In experiments the transition from normal to semicoiled and finally to curly I flagellar states are observed during a tumbling event. We know from Calladine's model [19], that also the coiled form is situated between the normal and the semicoiled state. Based on this model Speier *et al.* analyzed the internal strain energy. When the normal form is the state with lowest energy, the coiled form has a smaller energy than the semicoiled and curly I form. Therefore we also take the coiled state into account and hence describe a transition between four different helical states.

In accordance with our model in chapter 4, we assign the elastic free energy of Kirchhoff's rod theory and use additional energy densities δ_i for the ground states to each of the four relevant polymorphic forms. Since the free energy of a system always assumes a minimum, we locally assign the minimum of the free energy densities of the four polymorphic configurations to the bacterial flagellum with angular strain $\boldsymbol{\Omega}$

$$\mathfrak{f}_{\mathtt{poly}}(\boldsymbol{\Omega}, \boldsymbol{\Omega}_1, \boldsymbol{\Omega}_2, \boldsymbol{\Omega}_3, \boldsymbol{\Omega}_4) = \min_{n_R=2,3,4,5} \left(\mathfrak{f}_{\mathtt{cl}}(\boldsymbol{\Omega}, \boldsymbol{\Omega}_i) + \delta_{n_R}\right), \tag{5.5}$$

where we use the elastic free energy density $\mathfrak{f}_{\mathtt{cl}}$ of Eq. (2.46). The number of protofilaments in the R state $n_R = 2, 3, 4, 5$ refers to normal, coiled, semicoiled and curly I forms, respectively. The total elastic energy is given by the integral (4.5) but with the new four-state instead of the two-state energy density. For simplicity we assume a linear increase of the energy of the ground states, i. e. $\delta_2 = 0, \delta_3 = 0.1\text{pN}, \delta_4 = 0.2\text{pN}, \delta_5 = 0.3\text{pN}$. To derive the intrinsic curvature and torsion of the states we use Eq. (2.1).

In section 4.2 we shortly described how a polymorphic transition leads to a small phase shift in the spontaneous curvature. As discussed in section 2.1.1, the flagellar filament consists of eleven protofilaments. They assume two states (L and R) that mainly differ in length and therefore cause the bending of the flagellum. For the normal filament with two protofilaments in the R-state, we choose the Frenet frame as material frame. Consequently, we have $\boldsymbol{\Omega}_2 = (0, \kappa_2, \tau_2)$ with curvature κ_2 and torsion τ_2 for the normal form. Hence, the normal vector $\boldsymbol{n}$ corresponds to the material vector $\boldsymbol{e}_1$ and points for symmetry reasons between the two R-state protofilaments. During a transition from the normal to the other polymorphic forms, protofilaments in the L state switch into the R state. The normal vector always points into the direction of bending and therefore to the center of all R state protofilaments. Hence, for every protofilament, which switches

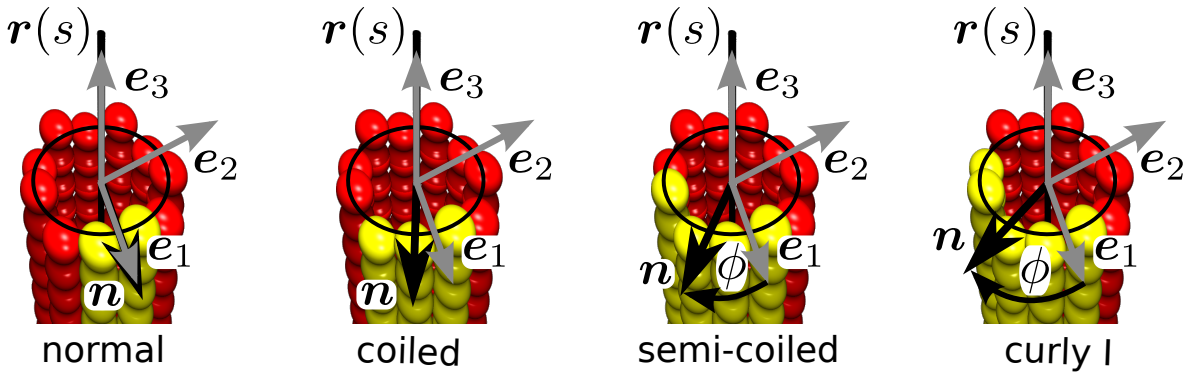

Abbildung 5.8: The molecular structure of the filament is changed during a polymorphic transition. We show in yellow the protofilament in the R state and in red the protofilament in the L state. The material frame is defined by the normal state, but the normal vector $\boldsymbol{n}$ which describes the direction of bending changes. Therefore the intrinsic angular strain includes a phase shift ϕ in the spontaneous curvature.

into the R state, the normal vector rotates with respect to the material frame by an angle of $\delta\phi = 2\pi/22$, as sketched in figure 5.8. We argued in chapter 4 that $\delta\phi$ is small and therefore neglected for a transition between two polymorphic forms. This is not true anymore for the transition between four states, as discussed below. In the following we use $\Omega_{n_R} = (\kappa_{n_R} \sin((2-n_R)\frac{\pi}{11}), \kappa_{n_R} \cos((2-n_R)\frac{\pi}{11}), \tau_{n_R})$ as the intrinsic rotational strain rate. The sign of the twist angle is chosen such that it supports a transition driven by a torque, which unwinds the normal state.

For the simulations we attach the filament to a sphere of radius 1µm as described in section 5.2. To ensure the numerical stability of the filament during the transition from a left- to a right-handed helix, we reduce the discretization length to $h = 0.1\mu\text{m}$.

In preliminary simulations we observe that a short segment of the filament at the end, which is attached to the sphere, sometimes points into the sphere. This is in contrast to the simulations of *Rhodobacter*, where the hinged boundary condition together with a soft repulsive potential of the cell body, was sufficient to describe the cell body-filament interaction. To avoid this unphysical behavior, we introduce an additional bending torque for the hook depending on $\cos\alpha = \boldsymbol{e}_3^{(0)} \cdot \boldsymbol{e}$, where $\boldsymbol{e}_3^{(0)}$ is the first tangent vector of the filament and $\boldsymbol{e}$ is the direction of the motor torque. For small angles the filament rotates freely as described in section 2.1.2. To ensure $\alpha < \pi/2$ we use a torque of the form

$$M_{\text{hook}}(\alpha) = M_H \begin{cases} 0 & \alpha < \alpha_0 \\ \frac{1}{\cos(\alpha)} - \frac{1}{\cos(\alpha_0)} & \alpha_0 < \alpha. \end{cases} \tag{5.6}$$

In the simulations we choose $\alpha_0 = \pi/4$ and $M_H = 3.5\text{pN}\mu\text{m}$.

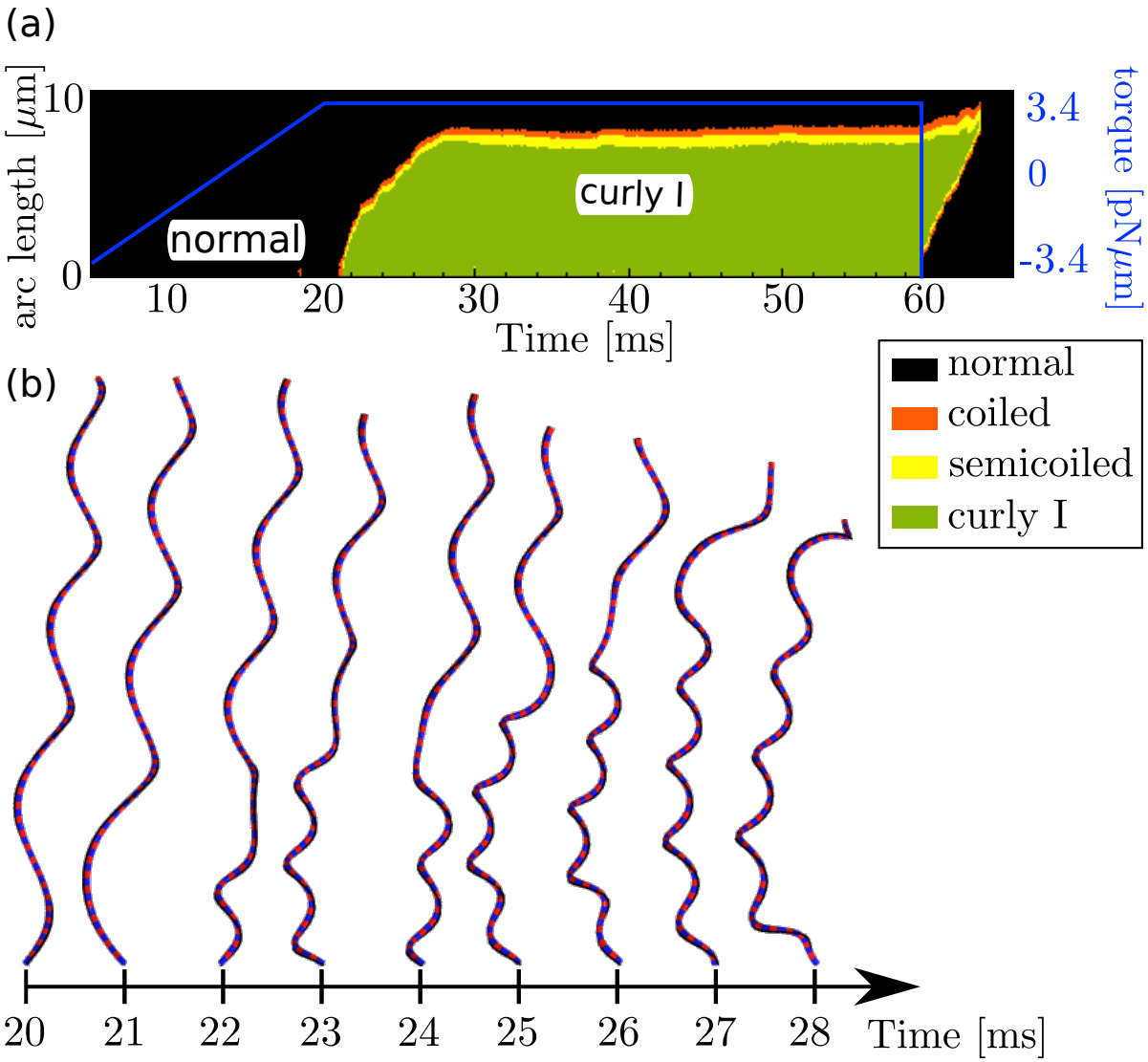

Abbildung 5.9: **(a)** Time evolution of the applied motor torque (blue line) and the actual polymorphic state at locations along the filament given in arc length. **(b)** Snapshots of the flagellar configuration during the normal-to-curly I transition which occurs during the tumbling of *E. coli*

We start our simulation with a filament that rotates in the normal state driven by a torque of -3.4pNμm. After some time, we linearly increase the motor torque within 15ms up to a value of $+3.4$pNμm. When the torque reaches its maximum, we observe a fast transition of 75% of the filament into the curly I form of the bacterial flagellum. The transition occurs within about 8ms which is much faster than the coiled-to-normal transition in *Rhodobacter sphaeroides*. The reason is the shorter relaxation time of a helix with small helical radius. After 40ms we reverse the sense of rotation of the motor again. We note that the abrupt change of the torque is artificial and a linear change as in the beginning is biologically more relevant. Nevertheless, a transition back into the normal state is observed. The two intermediate states, e. g. coiled and semicoiled, are only visible at the boundary between normal and curly I state. Figure 5.9 shows the time behavior of the applied motor torque (blue line) and the polymorphic state along the filament. We also show snapshots of the normal-to-curly I transition which are comparable to experimental snapshots shown in reference [121]. We note that the motor torque of 3.4pNμm, where the transition occurs, is in good agreement to the motor torque of 3.6pNμm reported for *E. coli* [13].

We repeat the simulations with polymorphic states where the phase shift in the spontaneous curvature is neglected. We observe a normal-to-curly I transition, too, but only 50% of the filament undergoes the transition. This confirms the importance of the phase shift in the spontaneous curvature for the transition between more than two polymorphic forms of the bacterial flagellum.

In summary, we have developed a model of the bacterial flagellum, which describes the transformations between different polymorphic states. In particular, we have demonstrated that the model also describes the normal-to-curly I transition observed during the tumbling of *Escherichia coli*. Hence, the model can be used to study the full tumbling event of this bacterium in future.

Kapitel 6

Conclusions

Flagella of bacteria such as *Escherichia coli* and *Salmonella typhimurium* assume different helical shapes during the tumbling phase. The aim of this work was to provide a model of the bacterial flagellum that will be used to study the tumbling event of bacteria in more detail. Therefore we demonstrated how to model the motor-driven rotating flagellum. We have developed a sufficiently simple elastic model to describe the polymorphism of the bacterial flagellum based on Kirchhoff's theory of an elastic rod. The model reproduces experimental force-extension curves including force-induced polymorphic transitions, and also enables to study the biological relevant rotation-induced polymorphic transformations.

We started by investigating the motor-driven rotating bacterial flagellum in chapter 3. We have used a discretized version of Kirchhoff's elastic-rod theory and a coarse-grained approach for driving the helical filament by a motor torque. The friction with the aqueous environment has been modeled within resistive force theory. Due to its helical geometry the rotating flagellum generates a thrust force, which pushes the bacterium forward. When increasing the motor torque, the thrust force reveals a supercritical Hopf bifurcation due to buckling of the helical filament. Increasing the torque further leads to a second buckling instability. The Hopf bifurcation is also visible, when the flagellum is attached to a load particle, which mimics the bacterial cell body. We have tuned the thrust force pushing against the cell body by the size of the load particle and therefore the critical torque for the buckling instability changes, too. Hence we have obtained a characteristic diagram showing the critical force versus torque for the buckling transition.

Furthermore we have developed a theory for the observed buckling transition by approximating the helical filament by a rod with an effective bending rigidity and the characteristic rotation-translation coupling. In general the filament buckles under the frictional forces and torques, which act along the filament. But for the biologically relevant regime, where the size of the load particle is comparable to a bacterial cell body, buckling is mostly due to the thrust force created along the filament and is comparable to a vertical column that buckles under its own weight [84]. In the limit of a small load particle the critical thrust force goes to zero and the buckling is mostly driven by the frictional torque acting along the filament, similar to a rod rotating around its axis at low Reynolds number [123, 132]. By taking the deformation of the rotating helical fila-

ment into account, we have obtained quantitative agreement with the simulation results in the biologically relevant regime.

We have discussed the biological relevance of the observed buckling transition. It is clear that swimming bacteria should avoid buckling for efficient locomotion. Nevertheless they are not able to simply increase bending rigidity since a certain flexibility is necessary during polymorphic transformations or to form a bundle. Our discussion in chapter 3 and the necessary torque, which we have obtained in simulations of chapter 5 for the polymorphic transformations, indicate that a single flagellum buckles under its own thrust force. Nevertheless, in peritrichous bacteria such as *E.coli* and *Salmonella* several flagella form a bundle which increases the bending stiffness and therefore buckling is not observed. Monotrichous bacteria have only a single flagellum but with a helical geometry that leads to a larger effective bending rigidity.

We found that a rotating flexible helix aligns parallel to the applied motor torque. This helps single-flagellated bacteria like *Rhodobacter sphaeroides* to swim straightforward. We have also shown that a pulling flagellum is not stably aligned along the applied torque, which is important for the chemotaxis of marine bacteria that use a back-and-forth rather than a run-and-tumble strategy.

In chapter 4 we have extended Kirchhoff's theory of elastic rods to describe the polymorphism of a bacterial flagellum. Using our model we have reproduced the force-extension curves recorded in experiments [28]. We have shown that thermal fluctuations implemented with Brownian dynamics simulations are crucial for polymorphic transformations to occur. Furthermore, we identified by analytic arguments a parameter region for the ground-state energy difference and the twist-to-bend ratio, where a coiled-to-normal transition is observable. We have also predicted a logarithmic dependence of the mean extension of the first coiled-to-normal transition on the extensional rate, which agrees with our simulations.

In chapter 5 we have shown that a rotating bacterial flagellum exhibits polymorphic transformations. Therefore we have applied our model to the single-flagellated bacterium *Rhodobacter sphaeroides* and have been able to reproduce its run-and-stop swimming path. Without an applied torque the filament is always in an open coiled state with small pitch and large radius. When we apply a sufficiently large torque, the filament undergoes a coiled-to-normal transition where the normal state is optimized to push the bacterium forward. The transition starts from the end of the filament that is attached to the cell body towards the distal end. Due to the large change of the helical height the normal filament is bent at the end of the coiled-to-normal transition. During the subsequent relaxation to a straight helix, the swimming direction of *Rhodobacter* changes, which is a crucial point for chemotaxis. When the motor torque is switched off again, the bacterium stops and the filament relaxes back into the coiled state starting from its free end towards the cell body. We have also analyzed the mean reorientation during a coiled-to-normal transition as a function of time needed to switch on the motor. The reorientation is largest when the motor is switched on fast.

Finally we have presented simulations of the polymorphic transformations observed

during the tumbling of *E.coli*. This involves four helical states with different handedness. The motor torque where the transition occurs is comparable to values measured for *E.coli*.

To summarize, we implemented a method to drive the bacterial flagellum by a motor torque. We extended Kirchhoff's theory of elastic rods to include the polymorphic forms of the bacterial flagellum. Our model reproduces force-extension curves observed in experiments. Finally we have demonstrated that our model explains the polymorphic transformations observed in rotating bacterial flagella. Therefore we provide a model to study the locomotion of a bacteria such as *Escherichia coli* and *Salmonella typhimurium*. Especially for the first time it is possible to study the tumbling event in full detail, which includes the dynamic interaction of several flagella and rotation-induced transformations between four different polymorphic forms of the bacterial flagellum.

List of Publications

Related to this work:

[A] Reinhard Vogel & Holger Stark, *Force-extension curves of bacterial flagella*, The European Physical Journal E: Soft Matter and Biological Physics **33**, 259–271 (2010)

[B] Reinhard Vogel & Holger Stark, *Motor-driven bacterial flagella and buckling instabilities*, The European Physical Journal E: Soft Matter and Biological Physics **35**, 1–15 (2012)

Other publications:

[C] Reinhard Vogel & Ulrich Behn, *Th1–Th2 Regulation and Allergy: Bifurcation Analysis of the Non-Autonomous System*, Mathematical Modeling of Biological Systems, Volume II, Birkhäuser Boston, 145-155 (2008)

[D] Christoph Speier, Reinhard Vogel & Holger Stark, *Modeling the bacterial flagellum by an elastic network of rigid bodies.*, Physical Biology **8**, 046009 (2011)

Diploma thesis:

[E] Reinhard Vogel *Th1-Th2-Regulation und Allergie: Bifurkationsanalyse des nichtautonomen Systems*, Diplomarbeit, Universität Leipzig (2007)

Literaturverzeichnis

[1] D. Apel and M. G. Surette. Bringing order to a complex molecular machine: the assembly of the bacterial flagella. *Biochim. Biophys. Acta*, 1778(9):1851–1858, 2008.

[2] A. Arkhipov, P. L. Freddolino, K. Imada, K. Namba, and K. Schulten. Coarse-grained molecular dynamics simulations of a rotating bacterial flagellum. *Biophysical Journal*, 91(12):4589 – 4597, 2006.

[3] J. P. Armitage and R. M. Macnab. Unidirectional, intermittent rotation of the flagellum of Rhodobacter sphaeroides. *J. Bacteriol.*, 169(2):514–518, 1987.

[4] J. P. Armitage, T. P. Pitta, M. A. Vigeant, H. L. Packer, and R. M. Ford. Transformations in flagellar structure of rhodobacter sphaeroides and possible relationship to changes in swimming speed. *J. Bacteriol.*, 181(16):4825–4833, 1999.

[5] J. P. Armitage and R. Schmitt. Bacterial chemotaxis: Rhodobacter sphaeroides and sinorhizobium meliloti–variations on a theme? *Microbiology*, 143(12):3671–3682, 1997.

[6] L. Arnold. *Stochastic differential equations: theory and applications*. A Wiley-Interscience publication. Wiley, 1974.

[7] V. I. Arnold. *Mathematical Methods of Classical Mechanics*. Springer-Verlag, 1978.

[8] S. Asakura. Polymerization of flagellin and polymorphism of flagella. *Adv. Biophys.*, 1:99–155, 1970.

[9] B. Behkam and M. Sitti. Bacterial flagella-based propulsion and on/off motion control of microscale objects. *Applied Physics Letters*, 90(2):023902, 2007.

[10] G. I. Bell. Models for the specific adhesion of cells to cells. *Science*, 200(4342):618–627, 1978.

[11] H. C. Berg. Motile behavior of bacteria. *Physics Today*, 53(1):24–29, 2000.

[12] H. C. Berg. The rotary motor of bacterial flagella. *Annual Review of Biochemistry*, 72(1):19–54, 2003.

[13] H. C. Berg. *E. coli in Motion*. Springer, 2004.

[14] H. C. Berg and E. M. Purcell. Physics of chemoreception. *Biophysical Journal*, 20(2):193–219, 1977.

[15] C.B. Biezeno and R. Grammel. *Technische Dynamik*. Technische Dynamik. Springer, 1939.

[16] R. L. Bishop. There is more than one way to frame a curve. *American Mathematical Monthly*, 82:246, 1975.

[17] R. Brown. A brief account of microscopical observations made on the particles contained in the pollen of plants. *Philosophical Magazine*, 4:161–173, 1828.

[18] J. Buder. Zur Kenntnis des Thiospirillum jenense und seiner Reaktionen auf Lichtreize. *Jahrbücher für wissenschaftliche Botanik*, 56:529 – 584, 1915.

[19] C. R. Calladine. Construction of bacterial flagella. *Nature*, 255:121–124, 1975.

[20] C. R. Calladine. Change of waveform in bacterial flagella: The role of mechanics at the molecular level. *Journal of Molecular Biology*, 118(4):457 – 479, 1978.

[21] G. G. Chassie, L. E. Becker, and W. L. Cleghorn. On the buckling of helical springs under combined compression and torsion. *International Journal of Mechanical Sciences*, 39(6):697 – 704, 1997.

[22] S. Chattopadhyay, R. Moldovan, C. Yeung, and X. L. Wu. Swimming efficiency of bacterium escherichia coli. *Proc. Natl. Acad. Sci. U.S.A.*, 103(37):13712–13717, 2006.

[23] S. Chattopadhyay and X. L. Wu. The effect of long-range hydrodynamic interaction on the swimming of a single bacterium. *Biophysical Journal*, 96(5):2023–2028, 2009.

[24] S. Childress. *Mechanics of swimming and flying.* Cambridge University Press, 1981.

[25] G. Chirico and J. Langowski. Kinetics of dna supercoiling studied by brownian dynamics simulation. *Biopolymers*, 34(3):415–433, 1994.

[26] N. Chouaieb, A. Goriely, and J. H. Maddocks. Helices. *Proc. Natl. Acad. Sci. U.S.A.*, 103(25):9398–9403, 2006.

[27] D. Coombs, G. Huber, J. O. Kessler, and R. E. Goldstein. Periodic chirality transformations propagating on bacterial flagella. *Physical Review Letters*, 89(11):118102, 2002.

[28] N. C. Darnton and H. C. Berg. Force-extension measurements on bacterial flagella: triggering polymorphic transformations. *Biophysical Journal*, 92(6):2230–2236, 2007.

[29] N. C. Darnton, L. Turner, K. Breuer, and H. C. Berg. Moving fluid with bacterial carpets. *Biophysical Journal*, 86(3):1863–1870, 2004.

[30] N. C. Darnton, L. Turner, S. Rojevsky, and H. C. Berg. On torque and tumbling in swimming escherichia coli. *J. Bacteriol.*, 189(5):1756–1764, 2007.

[31] J. K. G. Dhont. *An introduction to dynamics of colloids*. Elsevier, 1996.

[32] E. H. Dill. Kirchhoff's theory of rods. *Archive for History of Exact Sciences*, 44:1–23, 1992.

[33] A. Einstein. Über die von der molekularkinetischen Theorie der Wärme geforderte Bewegung von in ruhenden Flüssigkeiten suspendierten Teilchen. *Annalen der Physik*, 322(8):549–560, 1905.

[34] Leonhard Euler. *Methodus Inveniendi Lineas Curvas Maximi Minimive Proprietate Gaudente*. Kessinger Publishing, LLC, 1744.

[35] E. Evans. Probing the relation between force–lifetime–and chemistry in single molecular bonds. *Annu. Rev. Biophys. Biomol. Struct.*, 30:105–128, 2001.

[36] T. C. Flynn and J. Ma. Theoretical analysis of twist/bend ratio and mechanical moduli of bacterial flagellar hook and filament. *Biophysical Journal*, 86(5):3204 – 3210, 2004.

[37] B. Friedrich. A mesoscopic model for helical bacterial flagella. *Journal of Mathematical Biology*, 53(1):162–178, 2006.

[38] M. Fujii, S. Shibata, and S. I. Aizawa. Polar, peritrichous, and lateral flagella belong to three distinguishable flagellar families. *Journal of Molecular Biology*, 379(2):273 – 283, 2008.

[39] T. Furuta, F. A. Samatey, H. Matsunami, K. Imada, K. Namba, and A. Kitao. Gap compression/extension mechanism of bacterial flagellar hook as the molecular universal joint. *Journal of Structural Biology*, 157(3):481 – 490, 2007.

[40] R. E. Goldstein, A. Goriely, G. Huber, and C. W. Wolgemuth. Bistable helices. *Physical Review Letters*, 84(7):1631–1634, 2000.

[41] A. Goriely and M. Tabor. Nonlinear dynamics of filaments I. Dynamical instabilities. *Physica D:*, 105(1-3):20 – 44, 1997.

[42] A. Goriely and M. Tabor. Nonlinear dynamics of filaments II. Nonlinear analysis. *Physica D:*, 105(1-3):45 – 61, 1997.

[43] A. Goriely and M. Tabor. The nonlinear dynamics of filaments. *Nonlinear Dynamics*, 21:101–133, 2000.

[44] K. Guevorkian and J. M. Valles. Swimming paramecium in magnetically simulated enhanced, reduced, and inverted gravity environments. *Proc. Natl. Acad. Sci. U.S.A.*, 103(35):13051–13056, 2006.

[45] John Happel and Howard Brenner. *Low Reynolds Number Hydrodynamics*. Springer, 1983.

[46] J. A. Haringx. On the buckling and the lateral rigidity of helical compression springs. *Proc. Ned. Akad. Wet.*, 45:533–539 & 650–654, 1942.

[47] J. A. Haringx. On highly compressible helical springs and rubber rods, and their application for vibration-free mountings. *Philips Research Reports*, 3(6):401–449, 1948.

[48] E. Hasegawa, R. Kamiya, and S. Asakura. Thermal transition in helical forms of Salmonella flagella. *J. Mol. Biol.*, 160(4):609–621, 1982.

[49] K. Hasegawa, I. Yamashita, and K. Namba. Quasi- and nonequivalence in the structure of bacterial flagellar filament. *Biophysical Journal*, 74(1):569–575, 1998.

[50] W. R. Hesse, K. J. Freedman, D. K. Yi, C. W. Ahn, and M. Kim. Bacterial nanofluidic structures for medicine and engineering. *Small*, 6(8):895–909, 2010.

[51] W. R. Hesse, L. Luo, G. Zhang, R. Mulero, J. Cho, and M. J. Kim. Mineralization of flagella for nanotube formation. *Materials Science and Engineering: C*, 29(7):2282 – 2286, 2009.

[52] H. Hoshikawa and N. Saito. Brownian motion of helical flagella. *Biophysical Chemistry*, 10(1):81–89, 1979.

[53] H. Hotani. Micro-video study of moving bacterial flagellar filaments. ii. polymorphic transition in alcohol. *Biosystems*, 12(3-4):325–330, 1980.

[54] H. Hotani. Micro-video study of moving bacterial flagellar filaments. iii. cyclic transformation induced by mechanical force. *Journal of Molecular Biology*, 156(4):791 – 806, 1982.

[55] P. J. A. Janssen and M. D. Graham. Coexistence of tight and loose bundled states in a model of bacterial flagellar dynamics. *Phys. Rev. E*, 84:011910, 2011.

[56] C. J. Jones, R. M. Macnab, H. Okino, and S. I. Aizawa. Stoichiometric analysis of the flagellar hook-(basal-body) complex of salmonella typhimurium. *Journal of Molecular Biology*, 212(2):377 – 387, 1990.

[57] R. Kamiya and S. Asakura. Flagellar transformations at alkaline ph. *J. Mol. Biol.*, 108(2):513–518, 1976.

[58] R. Kamiya and S. Asakura. Helical transformations of salmonella flagella in vitro. *Journal of Molecular Biology*, 106(1):167 – 186, 1976.

[59] R. Kamiya, S. Asakura, K. Wakabayashi, and K. Namba. Transition of bacterial flagella from helical to straight forms with different subunit arrangements. *J. Mol. Biol.*, 131(4):725–742, 1979.

[60] D. Karpeev, I. S. Aranson, L. S. Tsimring, and H. G. Kaper. Interactions of semiflexible filaments and molecular motors. *Phys. Rev. E*, 76(5):051905, 2007.

[61] U. B. Kaupp, N. D. Kashikar, and I. Weyand. Mechanisms of sperm chemotaxis. *Annu. Rev. Physiol.*, 70:93–117, 2008.

[62] E. Kernchen. Zur Stabilität von Schraubenfedern. *Archive of Applied Mechanics*, 48:383–392, 1979.

[63] D. A. Kessler and Y. Rabin. Stretching instability of helical springs. *Physical Review Letters*, 90(2):024301, Jan 2003.

[64] M. Kim, J. C. Bird, A. J. van Parys, K. S. Breuer, and T. R. Powers. A macroscopic scale model of bacterial flagellar bundling. *Proc. Natl. Acad. Sci. U.S.A.*, 100(26):15481–15485, 2003.

[65] M. Kim and T. R. Powers. Hydrodynamic interactions between rotating helices. *Phys. Rev. E*, 69(6):061910, 2004.

[66] M. Kim and T. R. Powers. Deformation of a helical filament by flow and electric or magnetic fields. *Phys. Rev. E*, 71(2):021914, 2005.

[67] M. J. Kim and K. S. Breuer. Microfluidic pump powered by self-organizing bacteria. *Small*, 4(1):111–118, 2008.

[68] G. Kirchhoff. Über das Gleichgewicht und die Bewegung eines unendlich dünnen elastischen Stabes. *Journal für die reine und angewandte Mathematik*, 56:285 – 313, 1859.

[69] Peter E. Kloeden, Eckhard Platen, and Henri Schurz. *Stochastic Differential Equations*. Universitext. Springer Berlin Heidelberg, 1994.

[70] A. J. Kluyver and C. B. Van Niel. *The Microbe's contribution to biology.* Harvard university press, 1956.

[71] K. Kobayashi, T. Saitoh, D. S. H. Shah, K. Ohnishi, I. G. Goodfellow, R. E. Sockett, and S.-I. Aizawa. Purification and Characterization of the Flagellar Basal Body of Rhodobacter sphaeroides. *J. Bacteriol.*, 185(17):5295–5300, 2003.

[72] S. A. Koehler and T. R. Powers. Twirling elastica: Kinks, viscous drag, and torsional stress. *Physical Review Letters*, 85(22):4827–4830, 2000.

[73] L. D. Landau and E. M. Lifshitz. *Mechanics.* Pergamon Press, 1976.

[74] L. D. Landau and E. M. Lifshitz. *Theory of Elasticity.* Pergamon Press, 1986.

[75] L. D. Landau and E. M. Lifshitz. *Fluid mechanics.* Pergamon Press., 1987.

[76] S. H. Larsen, J. Adler, J. J. Gargus, and R. W. Hogg. Chemomechanical coupling without ATP: the source of energy for motility and chemotaxis in bacteria. *Proc. Natl. Acad. Sci. U.S.A.*, 71(4):1239–1243, 1974.

[77] P. Läuger. Torque and rotation rate of the bacterial flagellar motor. *Biophysical Journal*, 53(1):53–65, 1988.

[78] S. Y. Lee. *Systems Biology and Biotechnology of Escherichia Coli.* Springer, 2009.

[79] J. Lighthill. Flagellar hydrodynamics. *SIAM Review*, 18(2):161–230, 1976.

[80] J. Lighthill. Helical distributions of stokeslets. *Journal of Engineering Mathematics*, 30(1):35– 78, 1996.

[81] R. Liu and H. Ochman. Stepwise formation of the bacterial flagellar system. *Proc. Natl. Acad. Sci. U.S.A.*, 104(17):7116–7121, 2007.

[82] E. Lobaton and A. Bayen. Modeling and optimization analysis of single flagellum bacterial motion. In *American Control Conference, 2007. ACC '07*, pages 455 –461, july 2007.

[83] E. J. Lobaton and A. M. Bayen. Modeling and optimization analysis of a single-flagellum micro-structure through the method of regularized stokeslets. *Control Systems Technology, IEEE Transactions on*, 17(4):907 –916, 2009.

[84] A. E. H. Love. *A Treatise on the Mathematical Theory of Elasticity*, volume 4. Edition. New York Dover Publications, 1944.

[85] R. H. Luchsinger, B. Bergersen, and J. G. Mitchell. Bacterial swimming strategies and turbulence. *Biophysical Journal*, 77(5):2377–2386, 1999.

[86] R. M. Macnab. Bacterial flagella rotating in bundles: a study in helical geometry. *Proc. Natl. Acad. Sci. U.S.A.*, 74(1):221–225, 1977.

[87] R. M. Macnab. The bacterial flagellum: reversible rotary propellor and type iii export apparatus. *J. Bacteriol.*, 181(23):7149–7153, 1999.

[88] M. Manghi, X. Schlagberger, Y. W. Kim, and R. R. Netz. Hydrodynamic effects in driven soft matter. *Soft Matter*, 2:653–668, 2006.

[89] M. Manghi, X. Schlagberger, and R. R. Netz. Propulsion with a rotating elastic nanorod. *Physical Review Letters*, 96(6):068101, 2006.

[90] M. D. Manson, P. Tedesco, H. C. Berg, F. M. Harold, and C. van der Drift. A protonmotive force drives bacterial flagella. *Proc. Natl. Acad. Sci. U.S.A.*, 74(7):3060–3064, 1977.

[91] McMillen and Goriely. Tendril perversion in intrinsically curved rods. *Journal of Nonlinear Science*, 12(3):241–281, 2002.

[92] P.C. Nelson. *Biological physics: energy, information, life.* W.H. Freeman and Co., 2008.

[93] F. S. Nogueiral and H. G. P. L. Barros. Study of the motion of magnetotactic bacteria. *European Biophysics Journal*, 24:13–21, 1995.

[94] A. Okubo. Fantastic voyage into the deep: marine biofluid mechanics. *Lecture notes in biomathematics*, 71:32–47, 1987.

[95] M. Polin, I. Tuval, K. Drescher, J. P. Gollub, and R. E. Goldstein. Chlamydomonas swims with two gears in a eukaryotic version of run-and-tumble locomotion. *Science*, 325(5939):487–490, 2009.

[96] W.H. Press. *Numerical Recipes: The Art of Scientific Computing.* Cambridge University Press, 2007.

[97] E. M. Purcell. Life at low reynolds number. *American Journal of Physics*, 45(1):3–11, 1977.

[98] E. M. Purcell. The efficiency of propulsion by a rotating flagellum. *Proc. Natl. Acad. Sci. U.S.A.*, 94(21):11307–11311, 1997.

[99] M. Reichert and H. Stark. Synchronization of rotating helices by hydrodynamic interactions. *Eur. Phys. J. E*, 17(4):493–500, 2005.

[100] Michael Reichert. *Hydrodynamic Interactions in Colloidal and Biological Systems.* PhD thesis, University Konstanz, 2006.

[101] S. Y. Reigh, R. G. Winkler, and G. Gompper. Synchronization and bundling of anchored bacterial flagella. *Soft Matter*, 8:4363–4372, 2012.

[102] F. A. Samatey, K. Imada, S. Nagashima, F. Vonderviszt, T. Kumasaka, M. Yamamoto, and K. Namba. Structure of the bacterial flagellar protofilament and implications for a switch for supercoiling. *Nature*, 410(6826):331–337, 2001.

[103] F. A. Samatey, H. Matsunami, K. Imada, S. Nagashima, T. R. Shaikh, D. R. Thomas, J. Z. Chen, D. J. DeRosier, A. Kitao, and K. Namba. Structure of the bacterial flagellar hook and implication for the molecular universal joint mechanism. *Nature*, 431:1062–1068, 2004.

[104] B. Scharf. Real-time imaging of fluorescent flagellar filaments of rhizobium lupini h13-3: Flagellar rotation and ph-induced polymorphic transitions. *J. Bacteriol.*, 184(21):5979–5986, 2002.

[105] Michael Schmiedeberg. *Colloidal particles on quasicrystalline substrates*. PhD thesis, TU Berlin, 2008.

[106] C. L. Sears. A dynamic partnership: Celebrating our gut flora. *Anaerobe*, 11(5):247 – 251, 2005.

[107] M. Seville, T. Ikeda, and H. Hotani. The effect of sugars on the morphology of the bacterial flagellum. *FEBS Lett.*, 332(3):260–262, 1993.

[108] D. S. Shah, T. Perehinec, S. M. Stevens, S. I. Aizawa, and R. E. Sockett. The flagellar filament of rhodobacter sphaeroides: ph-induced polymorphic transitions and analysis of the flic gene. *J. Bacteriol.*, 182(18):5218–5224, 2000.

[109] T. R. Shaikh, D. R. Thomas, J. Z. Chen, F. A. Samatey, H. Matsunami, K. Imada, K. Namba, and D. J. Derosier. A partial atomic structure for the flagellar hook of salmonella typhimurium. *Proc. Natl. Acad. Sci. U. S. A.*, 102(4):1023–1028, 2005.

[110] Y. Sowa and R. M. Berry. Bacterial flagellar motor. *Q. Rev. Biophys.*, 41(2):103–132, 2008.

[111] S. E. Spagnolie and E. Lauga. Comparative hydrodynamics of bacterial polymorphism. *Physical Review Letters*, 106(5):058103, 2011.

[112] C. Speier, R. Vogel, and H. Stark. Modeling the bacterial flagellum by an elastic network of rigid bodies. *Phys. Biol.*, 8(4):046009, 2011.

[113] S. V. Srigiriraju and T. R. Powers. Continuum model for polymorphism of bacterial flagella. *Physical Review Letters*, 94(24):248101, 2005.

[114] S. V. Srigiriraju and T. R. Powers. Model for polymorphic transitions in bacterial flagella. *Phys. Rev. E*, 73(1):011902, 2006.

[115] E. L. Starostin and G. H. M. van der Heijden. Force and moment balance equations for geometric variational problems on curves. *Phys. Rev. E*, 79:066602, 2009.

[116] D. J. Struik. *Lectures on classical differential geometry*. Dover books on advanced mathematics. Addison-Wesley Pub. Co., 1988.

[117] N. Thamwattana, J. A. Mccoy, and J. M. Hill. Energy density functions for protein structures. *The Quarterly Journal of Mechanics and Applied Mathematics*, 61(3):431–451, 2008.

[118] S. Trachtenberg, D. J. DeRosier, S. I. Aizawa, and R. M. Macnab. Pairwise perturbation of flagellin subunits : The structural basis for the differences between plain and complex bacterial flagellar filaments. *Journal of Molecular Biology*, 190(4):569 – 576, 1986.

[119] Tropea. *Springer handbook of experimental fluid mechanics*. Springer, 2007.

[120] Z.C. Tu and Z.C. Ou-Yang. Elastic theory of low-dimensional continua and its applications in bio- and nano-structures. *Journal of Computational and Theoretical Nanoscience*, 5:422–448, 2008.

[121] L. Turner, W. S. Ryu, and H. C. Berg. Real-time imaging of fluorescent flagellar filaments. *J. Bacteriol.*, 182(10):2793–2801, 2000.

[122] S. B. van Albada, S. Tănase-Nicola, and P. R. ten Wolde. The switching dynamics of the bacterial flagellar motor. *Mol Syst Biol*, 5:316, 2009.

[123] H. Wada and R. R. Netz. Non-equilibrium hydrodynamics of a rotating filament. *Europhysics Letters*, 75(4):645–651, 2006.

[124] H. Wada and R. R. Netz. Model for self-propulsive helical filaments: Kink-pair propagation. *Physical Review Letters*, 99(10):108102, 2007.

[125] H. Wada and R. R. Netz. Stretching helical nano-springs at finite temperature. *Europhysics Letters*, 77(6):68001, 2007.

[126] H. Wada and R. R. Netz. Discrete elastic model for stretching-induced flagellar polymorphs. *Europhysics Letters*, 82(2):28001, 2008.

[127] H. Wada and R. R. Netz. Hydrodynamics of helical-shaped bacterial motility. *Phys. Rev. E*, 80(2):021921, 2009.

[128] H. Wada and R. R. Netz. Plectoneme creation reduces the rotational friction of a polymer. *Europhysics Letters*, 87(3):38001, 2009.

[129] N. Watari and R. G. Larson. The hydrodynamics of a run-and-tumble bacterium propelled by polymorphic helical flagella. *Biophysical Journal*, 98(1):12–17, 2010.

[130] W. B. Whitman, D. C. Coleman, and W. J. Wiebe. Prokaryotes: the unseen majority. *Proc. N*, 95(12):6578–6583, 1998.

[131] C. H. Wiggins and R. E. Goldstein. Flexive and propulsive dynamics of elastica at low reynolds number. *Physical Review Letters*, 80:3879–3882, 1998.

[132] C. W. Wolgemuth, T. R. Powers, and R. E. Goldstein. Twirling and whirling: Viscous dynamics of rotating elastic filaments. *Physical Review Letters*, 84(7):1623–1626, 2000.

[133] L. Xie, T. Altindal, S. Chattopadhyay, and X. L. Wu. Bacterial flagellum as a propeller and as a rudder for efficient chemotaxis. *Proc. Na*, 108(6):2246–2251, 2011.

[134] I. Yamashita, K. Hasegawa, H. Suzuki, F. Vonderviszt, Y. Mimori-Kiyosue, and K. Namba. Structure and switching of bacterial flagellar filaments studied by x-ray fiber diffraction. *Nature Structural & Molecular Biology*, 5(2):125–132, 1998.

[135] H. Yamazaki and K. D. Squires. Comparison of oceanic turbulence and copepod swimming. *MEPS*, 144:299–301, 1996.

[136] H. Yeh, P. Liu, M. Briggs, and C. Synolakis. Propagation and amplification of tsunamis at coastal boundaries. *Nature*, 372(6504):353–355, 1994.

[137] K. Yonekura, S. Maki-Yonekura, and K. Namba. Complete atomic model of the bacterial flagellar filament by electron cryomicroscopy. *Nature*, 424(6949):643–650, 2003.

[138] L. Zhang, J. J. Abbott, L. Dong, B. E. Kratochvil, D. Bell, and B. J. Nelson. Artificial bacterial flagella: Fabrication and magnetic control. *Applied Physics Letters*, 94(6):064107, 2009.

[139] Z. Zhou, P. Y. Lai, and B. Joós. Elasticity and stability of a helical filament. *Phys. Rev. E*, 71(5):052801, 2005.

[140] Z. Zhou, P. Y. Lai, and B. Joós. Erratum: Elasticity and stability of a helical filament [Phys. Rev. E **71**, 052801 (2005)]. *Phys. Rev. E*, 73(3):039910, 2006.

Zusammenfassung

Bakterien wie *Escherichia coli* oder *Salmonella typhimurium* schwimmen durch die Rotation eines Bündels von Flagellen. Diese sind lange fadenähnliche Biopolymere in der Form einer Helix. Ein einzelnes Flagellum wird durch einen rotierenden Motor angetrieben, der in der Zellwand sitzt. Durch die Rotation erzeugt das Flagellum, ähnlich wie eine Schiffsschraube, eine Vortriebskraft, die das Bakterium durch die umgebende Flüssigkeit schiebt. Während des Schwimmens ändern die Bakterien in regelmäßigen Abständen zufällig ihre Schwimmrichtung. Hierzu drehen sie die Rotationsrichtung eines Flagellums um, wodurch es gezwungen ist, das Bündel mit den anderen Flagellen zu verlassen. Dabei durchläuft es eine Sequenz verschiedener helikaler Formen, beginnend mit einer linkshändigen und endend mit einer rechtshändigen Helix.

Ziel dieser Arbeit ist es, ausgehend von der klassischen Elastizitätstheorie gebogener langer dünner Stäbe von G. Kirchhoff (1858) ein Modell für die beobachteten Übergänge zwischen den verschiedenen Zuständen des Bakterienflagellums zu entwickeln.

Hierzu beginnen wir mit der Simulation eines einzelnen rotierenden elastischen Flagellums. Dabei erzeugt die durch die Rotation entstehende Vortriebskraft eine Biegeinstabilität der elastischen Helix. Ausgehend von der Theorie knickender Stäbe erklären wir quantitativ die beobachtete Instabilität.

Anschließend erweitern wir die klassische Theorie elastischer Stäbe, um zwei oder mehr helikale Gleichgewichtszustände zu beschreiben. Basierend auf experimentellen Beobachtungen nehmen wir an, dass die verschiedenen Zustände sich durch Kirchhoffs Theorie beschreiben lassen, und der Zustand mit der geringste elastische Energie angenommen wird. Um unser Modell zu testen, simulieren wir einen dehnungsinduzierten Übergang zwischen zwei helikalen Formen. Die hierdurch erhaltenen Kraft-Dehnungs-Kurven stimmen gut mit experimentellen Daten überein. Darüber hinaus erhalten wir eine Eingrenzung für die elastischen Parameter des Bakterienflagellums.

Wir wenden unser Modell des Flagellums auf ein Bakterium namens *Rhodobacter sphaeroides* an. Dieses besitzt nur ein Flagellum und nutzt einen Übergang zwischen einer Helix mit kleiner und großer Ganghöhe aus, um seine Richtung zu ändern. Es stellt somit ein einfaches Modellsystem dar, um rotationsgetriebene Übergänge zu studieren. Mit unserem Modell können wir das typische Schwimmverhalten von *R. sphaeroides* reproduzieren und sehen, dass die schnelle Änderung der Ganghöhe während des Übergangs verantwortlich für dessen Richtungsänderung ist.

Am Ende der Arbeit demonstrieren wir, dass unser Modell ebenfalls die Übergänge zwischen mehreren Zuständen mit unterschiedlicher Händigkeit beschreibt, die während des Schwimmens von *E. coli* und *Salmonella* beobachtet werden. Somit ist es in Zukunft möglich, den vollständigen Schwimmzyklus von diesen Bakterien am Computer zu studieren.

Abstract

Bacteria like *Escherichia coli* and *Salmonella typhimurium* swim by rotating flagella. These are long helical filamentlike biopolymers. Each flagellum is driven by a rotary motor situated in the cell wall. Due to the rotation of the flagellum a thrust force is created which pushes the bacterium through the surrounding fluid. From time to time the bacterium changes its swimming direction randomly. For this they switch the rotational direction of the flagellum which leads to the leaving of the bundle and undergoes a sequence of different helical configurations starting from a left-handed and ending with a right-handed helix.

This work aims to develop a model for the transitions between the polymorphic forms of the bacterial flagellum based on the classical elasticity theory of curved rods from Kirchhoff (1858). Therefor we start with simulations of a single rotating helical filament. We observe a buckling instability of the elastic helix which is caused by the thrust force of the flagellum. Starting from the buckling theory of rods we explain quantitative the instability.

After that we extend the classical theory to describe two or more helical equilibrium states. Based on experimental observations we assume that every polymorphic form is described by Kirchhoff's theory. The state which has the lowest elastic energy is observed. To validate our model we simulate stretching induced polymorphic transitions between two polymorphic forms. We measure force-extension curves in agreement with experimental results.

We apply our model of the flagellum to simulate the swimming of the bacterium *Rhodobacter sphaeroides*. It uses a polymorphic transition of its single flagellum from a helical form with small pitch to a form which is optimized for swimming, to change its swimming direction randomly. Therefor it is a minimal model to study rotational-driven polymorphic transformations. Our model reproduces the swimming behavior of *R. sphaeroides* and we show that the fast and large increase of the helical pitch is responsible for the random reorientation of the cell.

Finally we demonstrate that our model also describes the transition between several polymorphic states with different handedness as observed for *E. coli* and *Salmonella*. Therefor it is possible to study the swimming of these bacteria in more detail in future work.

Danksagung

Für meine Doktorarbeit schulde ich sehr vielen Menschen einen herzlichen Dank. Insbesondere danke ich:

- an erster Stelle meinem Doktorvater Prof. Dr. Holger Stark, der mir meine Promotion ermöglicht hat. Besonders hervorheben möchte ich die Freiheiten, die er mir bei meiner Arbeit gewährt hat, und die konstruktiven Gespräche und Kritiken, die einen wertvollen Beitrag für diese Arbeit darstellen.
- Prof. Dr. Roland Netz, der sich als Gutachter meiner Arbeit zur Verfügung stellte, und Prof. Dr. Martin Schoen, der den Vorsitz des Promotionsausschusses übernahm.
- Prof. Dr. Stephan Herminghaus und der gesamten Abteilung komplexe Fluide am Max-Planck-Institut für Dynamik und Selbstorganisation in Göttingen, dafür das ich mich hier für zwei Monate in das Forschungsgebiet meiner Doktorarbeit einarbeiten konnte.
- der VolkswagenStiftung, die das Projekt *Swimming of bacteria at low Reynolds numbers* förderte, in dessen Rahmen meine Doktorarbeit entstand.
- Diana Kaminski, Andreas Zöttle, Johannes Taktikos und Maximilian Schmitt für die Unterstützung beim Korrekturlesen meiner Arbeit.
- allen derzeitigen und ehemaligen Mitgliedern der Arbeitsgruppe für das gute Arbeitsumfeld und die vielen hilfreichen Diskussionen.

Abschliessend bedanke ich mich noch bei meiner Familie, die mir immer motivierend beiseite stand.